DETERMINATION OF CONSTRAINTS ON THE SKYRME ENERGY DENSITY FUNCTIONAL AND THE MEAN FIELD VIA THE $3S_{1/2}$ STATE IN ^{206}PB

A Dissertation

by

MASON ROBERT ANDERS

Submitted to the Office of Graduate and Professional Studies of
Texas A&M University
in partial fulfillment of the requirements for the degree of

DOCTOR OF PHILOSOPHY

Chair of Committee,	Shalom Shlomo
Committee Members,	Dave H. Youngblood
	Ralf Rapp
	William H. Bassichis
	Sherry J. Yennello
Head of Department,	George R. Welch

August 2015

Major Subject: Physics

ABSTRACT

In the first part of this study, we present results of fully self-consistent Hartree-Fock based random phase approximation calculations of the strength functions S(E) and centroid energies E_{CEN} of isoscalar (*T = 0*) and isovector (*T = 1*) giant resonances of multipolarities *L = 0 - 3* in ^{40}Ca, ^{48}Ca, and ^{208}Pb using a wide range of 34 commonly employed Skyrme type nucleon-nucleon effective interactions. We determined the sensitivities of E_{CEN} and of the isotopic differences $E_{CEN}(^{48}Ca) - E_{CEN}(^{40}Ca)$ to physical quantities, such as nuclear matter incompressibility coefficient, symmetry energy density and effective mass, associated with the Skyrme interactions and compare the results with the available experimental data.

In the second part of this study, we present a novel method, using the single particle Schrodinger equation, to determine the central potential directly from the single particle matter density and its first and second derivatives. As an example, we consider the experimental data for the charge density difference between the isotones ^{206}Pb – ^{205}Tl, deduced by analysis of elastic electron scattering measurements which corresponds to the shell model $3s_{1/2}$ proton orbit, and determine the corresponding single particle potential (mean-field). We also present results of least-square fits to parametrized single particle potentials. The $3s_{1/2}$ wave functions of the determined potentials reproduce fairly well the experimental data within the quoted errors. More accurate experimental data, with uncertainty smaller by a factor of two or more, may answer the question how well can the data be reproduced by a calculated $3s_{1/2}$ wave function.

ACKNOWLEDGEMENTS

I would like to thank my advisor, Dr. Shalom Shlomo, and my committee members, Dr. Youngblood, Dr. Rapp, Dr. Bassichis, and Dr. Yennello, for their guidance and support throughout the course of this research. I also would like to thank Dr. Natowitz for substituting for my final defense. I also want to extend my gratitude to the Department of Energy and the Cyclotron Institute for providing funding to pursue my research.

I want to thank the physics professors at Austin College, Dr. Salisbury, Dr. Baker, Dr. Robinson, and Dr. Troncalli for inspiring me and helping me through my formative years in physics research. I also want to thank my first physics teacher who got me started down this path. Mr. Acker, thank you for all of the time and kindness you gave to me preparing me for college.

Also, thank you to all of my physics friends, Mike, Elizabeth, Jimmy, Andrew, Danny, and Ellie for getting me through my coursework. I hope I was as helpful to you. Additionally, I want to thank Clement, Vaikunth, and Miguel for all of the fun lunches we had together. Thank you Matteo for giving me laughs throughout the workday.

Finally, I want to say thank you and I love you to my family who has sacrificed so much for me over the years. Specifically, thanks mom and dad for all of your support and love. Thanks Brittney and Grant for always ganging up on me over the years. Last but not least, I want to say thank you and I love you to my beautiful wife, Courtney, who is always there for me and keeps me motivated to succeed.

NOMENCLATURE

α_D	Electric polarizability
A, Z, N	Number of nucleons, protons, and neutrons
CM	Center of mass
E/A	Energy per nucleon at saturation density
E_{CEN}	Centroid energy
EDF	Energy density functional
EOS	Equation of state
EWSR, m_1	Energy weighted sum rule
GR	Giant resonance
HF	Hartree-Fock
HIC	Heavy ion collision
IEWSR, m_{-1}	Inverse energy weighted sum rule
ISGMR (E0) ($T0L0$)	Isoscalar giant monopole resonance
ISGDR (E1) ($T0L1$)	Isoscalar giant dipole resonance
ISGQR (E2) ($T0L2$)	Isoscalar giant quadrupole resonance
ISGOR (E3) ($T0L3$)	Isoscalar giant octopole resonance
IVGMR ($T1L0$)	Isovector giant monopole resonance
IVGDR ($T1L1$)	Isovector giant dipole resonance
IVGQR ($T1L2$)	Isovector giant quadrupole resonance
IVGOR ($T1L3$)	Isovector giant octopole resonance
J	Symmetry energy at ρ_0

κ	NM value of the enhancement factor of the EWSR of the IVGDR
K_{NM}	Incompressibility of nuclear matter
K_{sym}	Related to second derivative of symmetry energy at ρ_0
L	Related to first derivative of symmetry energy at ρ_0
m*/m	Effective mass
NM	Nuclear matter
ρ_0	saturation density of nuclear matter
RPA	Random Phase Approximation
$r_n - r_p$	Neutron skin of a nucleus
WS	Woods-Saxon

TABLE OF CONTENTS

LIST OF FIGURES

LIST OF TABLES

CHAPTER I

INTRODUCTION*

Collective modes in nuclei, which are composed of two kinds of nucleons, protons (*Z*) and neutrons (*N*), have been the subject of extensive theoretical and experimental studies during several decades [1-3], since they contribute significantly to our understanding of bulk properties of nuclei, their non-equilibrium properties and properties of the nuclear force. Of particular interest is the equation of state (EOS), i.e. the binding energy per nucleon as a function of the neutron and proton number densities, of infinite nuclear matter (no Coulomb interaction). The EOS is an important ingredient in the study of properties of nuclei at and away from stability, the study of structure and evolution of compact astrophysical objects, such as neutron stars and core-collapse supernovae, and the study of heavy-ion collisions (HIC) [4,5]. The saturation point of the equation of state (EOS) for symmetric (*N*=*Z*) nuclear matter (NM) is well determined from the measured binding energies and central matter densities of nuclei, by extrapolation to infinite NM [1,2]. To extend our knowledge of the EOS beyond the saturation point of symmetric NM, an accurate value of the NM incompressibility coefficient K_{NM}, which is directly related to the curvature of the EOS of symmetric NM, is needed. An accurate knowledge of the dependence of the symmetry energy, $E_{sym}(\rho)$, on the matter density ρ is needed for the EOS of asymmetric NM.

*Part of this chapter is reprinted with permission from "Giant Resonances in ^{40}Ca and ^{48}Ca" by M. R. Anders *et. al.*, 2013. *Physical Review C*, **87**, 024303, Copyright [2013] by American Physical Society.

There have been many attempts over the years to determine K_{NM} and $E_{sym}(\rho)$ by considering physical quantities which are sensitive to the values of K_{NM} and $E_{sym}(\rho)$ [3,4,6,7]. We investigate the sensitivity of the strength function distributions of the isoscalar and isovector giant resonances with multipolarities L = 0-3 of the isotopes ^{40}Ca and ^{48}Ca to bulk properties of NM, such as K_{NM}, E_{sym} and the effective mass m*. It is well known that the energies of the compression modes, the isoscalar giant monopole resonance (ISGMR) and isoscalar giant dipole resonance (ISGDR), are very sensitive to the value of K_{NM} [1,3,8]. Also the energies of the isovector giant resonances, in particular, the isovector giant dipole resonance (IVGDR), are sensitive to the density dependence of E_{sym} [9,10], commonly parameterized in terms of the quantities J, L and K_{sym}, which are the value of $E_{sym}(\rho)$ at saturation density (also known as symmetry energy coefficient), and the quantities directly related to the derivative and the curvature of $E_{sym}(\rho)$ at the saturation density, respectively. Furthermore, information on the density dependence of E_{sym} can also be obtained by studying the isotopic dependence of strength functions, such as the difference between the isovector strength functions of ^{40}Ca and ^{48}Ca and between ^{112}Sn and ^{124}Sn. We note that the value of the neutron-proton asymmetry parameter $\delta = (N-Z)/A$ increases from ^{40}Ca to ^{48}Ca by a value of 0.167 which is significantly larger than the change of 0.087 between ^{112}Sn and ^{124}Sn.

In early analysis of the experimental data on the ISGMR [11,12], a semiclassical model was adopted in order to relate the energy of the ISGMR to an incompressibility coefficient K_A of the nucleus and carry out a Leptodermous ($A^{-1/3}$) expansion of K_A, similar to a mass formula, to parameterize K_A into volume (K_{NM}), surface (K_S),

symmetry (K_τ) and coulomb (K_C) terms [11,13,14]. Shlomo and Youngblood [14] showed that this type of analysis could not provide a unique solution even including all available world data as of that time. More recently [15] a semiclassical analysis of the ISGMR data in the Sn isotopes demonstrated that the value obtained for K_τ is quite sensitive to the number of terms employed in the Leptodermous expansion. We adopt the microscopic approach of fully self-consistent Hartree-Fock (HF) based random phase approximation (RPA), employing an effective nucleon-nucleon interaction. In the HF-RPA approach, the values of K_{NM} and the density dependence of E_{sym} are then deduced from the interaction that best reproduces the experimental data on the strength functions of the giant resonance. (see the review in Ref. [3]). It is important to note that ground state properties of nuclei are well described by the HF approximation, using an effective nucleon-nucleon interaction, such as the Skyrme type interaction [16-18], with parameters obtained by a fit to a selected set of experimental data on binding energies and radii of nuclei [1,2]. It has also been demonstrated that HF-based RPA nicely reproduces the properties of low lying collective states as well as of giant resonances [1,2].

Recently the giant resonance region from 9.5 MeV < E_x < 40 MeV in ^{48}Ca was studied with inelastic scattering of 240 MeV α particles at small angles, including 0º. Close to 100% of the ISGMR (E0), ISGDR (E1) and isoscalar giant quadrupole resonance (E2) strengths have been located between 9.5 and 40 MeV in ^{48}Ca [19]. To study the effect of neutron-proton asymmetry, a comparison with the available data for ^{40}Ca [20-22], as well as with the results obtained within the HF-based RPA, was carried

out in Ref. [19]. The ISGMR has been found at somewhat higher energy in ^{48}Ca than in ^{40}Ca, whereas self-consistent HF-RPA calculations obtained using the SGII [23], KDE0 [24], SKM* [25] and SK255 [26] Skyrme interactions predict a centroid energy in this neutron rich Ca isotope lower than in ^{40}Ca.

We extend our theoretical investigation by considering the isoscalar and isovector giant resonances of multipolarities $L = 0 - 3$ in ^{40}Ca and ^{48}Ca. In chapter II we review the basic elements of the self-consistent HF-based RPA theory for the strength functions of isoscalar ($T = 0$) and isovector ($T = 1$) giant resonances and the EOS of NM and asymmetric NM. In chapter III we present results of our calculations for the strength functions S(E) and centroid energies E_{CEN} obtained for giant resonances of $T = 0, 1$ and multipolarities $L = 0 - 3$ in ^{40}Ca and ^{48}Ca, using a wide range of 18 commonly used Skyrme type nucleon-nucleon effective interactions. We pay attention to the issue of self-consistency and investigate the sensitivities of E_{CEN} and of the isotopic differences $E_{CEN}(^{48}Ca) - E_{CEN}(^{40}Ca)$ to physical quantities, such as nuclear matter incompressibility coefficient, symmetry energy density and effective mass, associated with the effective nucleon-nucleon interactions, and compare the results with available experimental data. In chapter IV we present results of our calculations for the strength functions S(E) and centroid energies E_{CEN} obtained for giant resonances of $T = 0, 1$ and multipolarities $L = 0 - 3$ in ^{208}Pb, using a wide range of 34 commonly used Skyrme type nucleon-nucleon effective interactions. In particular we are looking at the correlation between the electric polarizability and the neutron skin of ^{208}Pb as there has been recent work that suggests a

strong correlation between two and thus an indirect method of extracting the neutron skin.

In chapter V we describe our investigation to see if we can glean any information about the $3s_{1/2}$ mean field from the charge and proton densities of ^{206}Pb and ^{205}Tl. Thus to review, the shell model, which is based on the assumption that nucleons in the atomic nucleus move independently in single particle orbits associated with a single particle potential, has been very successful in explaining many features of nuclei [27]. In determining the nuclear mean-field potential, it is common to: (i) parametrize the central potential, using for example the Woods-Saxon (WS) form, and determine the parameters by a fit of calculated properties, such as single particle energy and reaction cross-sections, to the corresponding experimental data [1]; and (ii) carry out HF calculations using a parametrized effective two-body interaction and determine the parameters by a fit to experimental data and deduce the mean-field potential [28]. We present a novel method, using the single particle Schrödinger equation for a wave function $\Psi(\vec{r})$ with eigenenergy E, to determine the central potential $V(\vec{r})$ directly from the measured single particle matter density, $\rho(\vec{r}) = [\Psi(\vec{r})]^2$ and its first and second derivatives, assuming these are known for all $\vec{r}$.

A well-known important test of the shell model is the experimental measurement of the charge distribution of the proton $3s_{1/2}$ orbit given by the charge density difference, $\Delta\rho_c(r)$, between charge density distributions of the isotones ^{206}Pb – ^{205}Tl, determined by analysis of elastic electron scattering measurements [29,30]. The experimental data for the $3s_{1/2}$ charge density shows a clear maximum at the center of ^{206}Pb with two

additional maxima, which nicely corresponds to the shape of the shell model $3s_{1/2}$ proton orbit, in agreement with the simple shell model. It was pointed out [31] that commonly used central potentials, such as the WS potential, lead to a $3s_{1/2}$ charge density in disagreement with experimental data. In particular, the central density obtained from the WS potential is too large by 40%.

This difference between data and the WS results was attributed in Ref. [31] to be due to the effects of two-body short range correlations. Using our new method, we look for the single particle nuclear potential that corresponds to the experimental charge density associated with the proton $3s_{1/2}$ orbit in ^{206}Pb. We point out that the resulting single particle potential, if found, will provide a stringent limit on the effects of short correlations on the expected values of long-range operators, an important test for the shell model. The potential can also be used as an additional experimental constraint in determining a modern energy density functional (EDF) for more reliable prediction of properties of nuclei and nuclear matter [28,32].

In the second section of chapter V we consider the single particle Schrödinger equation and describe the method for determining the single particle potential $V(\vec{r})$ from a given single particle wave function $\Psi(\vec{r})$ or matter density, $\rho(\vec{r}) = [\Psi(\vec{r})]^2$, assuming it is known for all $\vec{r}$ [27]. In particular, we consider the case of spherical symmetry. We also describe the method of deducing the point proton density from the charge distribution determined in electron scattering measurements. In the third section of chapter V we present results for the case of the experimental data [29,30] for the charge density difference between the close $(\Delta Z = 1)$ isotones ^{206}Pb – ^{205}Tl, associated

with the $3s_{1/2}$ proton single particle orbit, and determine the corresponding single particle potential. In the last section of chapter V we present our conclusions.

CHAPTER II

SELF-CONSISTENT HARTREE-FOCK BASED RANDOM PHASE APPROXIMATION APPROACH TO CALCULATION OF GIANT RESONANCES AND EQUATION OF STATE OF NUCLEAR MATTER*

Introduction

In numerical calculations of the properties of giant resonances in nuclei within the HF-based RPA theory, one starts by adopting an effective nucleon-nucleon interaction V_{12}, such as the Skyrme interaction, with parameters determined by a fit of the HF predictions to experimental data on ground state properties, such as binding energies and radii, of a selected set of a wide range of nuclei. Then, the RPA equations are solved using the particle-hole interaction deduced from V_{12}, by employing a certain numerical method [33-35], and the physical quantities of interest, such as the strength functions S(E) and transition densities, are calculated. We point out that in fully self-consistent HF-based RPA calculations; one should include all the components of V_{12} in the RPA calculations and use a sufficiently large particle-hole configuration space to insure convergence. Necessary conditions for fully self-consistent calculations are; (i) The spurious isoscalar dipole state (due to center of mass motion) is obtained at zero energy; and (ii) The energy weighted sum rules (EWSRs) are fulfilled.

* Part of this chapter is reprinted with permission from "Giant Resonances in ^{40}Ca and ^{48}Ca" by M. R. Anders *et. al.,* 2013. *Physical Review C,* **87**, 024303, Copyright [2013] by American Physical Society.

Skyrme Energy Density Functional

The total wave function Φ of the nucleus with *A* nucleons in the HF approximation is a Slater determinant made up of single-particle wave functions $\phi_i(\vec{r}_i, \sigma_i, \tau_i)$ where $\vec{r}_i$, σ_i, and τ_i are the spatial, spin, and isospin coordinates of the *i*-th nucleon. $\tau_i = 1/2$ for protons and $\tau_i = -1/2$ for neutrons.

$$\Phi = \frac{1}{\sqrt{A!}} \det \begin{bmatrix} \phi_1(\vec{r}_1, \sigma_1, \tau_1) & \cdots & \phi_A(\vec{r}_1, \sigma_1, \tau_1) \\ \vdots & \ddots & \vdots \\ \phi_1(\vec{r}_A, \sigma_A, \tau_A) & \cdots & \phi_A(\vec{r}_A, \sigma_A, \tau_A) \end{bmatrix} \tag{2.1}$$

In a spherical nucleus, the single-particle wave function is composed of three parts, the radial function $R_\alpha(r)$, the spherical harmonic function $Y_{jlm}(\vec{r}, \sigma)$ and the isospin function $\chi_{m_\tau}(\tau)$.

$$\phi_i(\vec{r}_i, \sigma_i, \tau_i) = \frac{R_\alpha(r_i)}{r_i} Y_{jlm}(\vec{r}_i, \sigma_i) \chi_{m_\tau}(\tau_i) \tag{2.2}$$

The total Hamiltonian H of the nucleus for *A* nucleons is

$$\mathrm{H} = T + \sum_{i<j}^{A} V(\vec{r}_i, \vec{r}_j) = T + \sum_{i<j}^{A} V_{ij} + V_{Coul}, \tag{2.3}$$

where the kinetic energy operator T is given by

$$T = -\frac{\hbar^2}{2} \sum_{i=1}^{A} \frac{\nabla_i^2}{m_{\tau_i}}, \tag{2.4}$$

and the Coulomb potential V_{Coul} is given by

$$V_{Coul} = e^2 \sum_{i<j}^{Z} \frac{1}{|r_{ij}|}, \tag{2.5}$$

where the sum is over the *Z* protons. We adopt the Skyrme type effective nucleon-nucleon interaction for the two-body potential V_{ij} [36]:

$$V_{ij} = t_0\left(1 + x_0 P_{ij}^{\sigma}\right)\delta\left(\vec{r}_i - \vec{r}_j\right) + \frac{1}{2}t_1\left(1 + x_1 P_{ij}^{\sigma}\right)\left[\overleftarrow{k}_{ij}^2\delta\left(\vec{r}_i - \vec{r}_j\right) + \delta\left(\vec{r}_i - \vec{r}_j\right)\vec{k}_{ij}^2\right]$$

$$+ t_2\left(1 + x_2 P_{ij}^{\sigma}\right)\overleftarrow{k}_{ij}\delta\left(\vec{r}_i - \vec{r}_j\right)\vec{k}_{ij} + \frac{1}{6}t_3\left(1 + x_3 P_{ij}^{\sigma}\right)\rho^{\alpha}\left(\frac{\vec{r}_i + \vec{r}_j}{2}\right)\delta\left(\vec{r}_i - \vec{r}_j\right) \tag{2.6}$$

$$+ iW_0\overleftarrow{k}_{ij}\delta\left(\vec{r}_i - \vec{r}_j\right)\left(\vec{\sigma}_1 + \vec{\sigma}_2\right) \times \vec{k}_{ij} .$$

$\vec{k}_{ij} = -i\left(\vec{\nabla}_i - \vec{\nabla}_j\right)/2$ and $\overleftarrow{k}_{ij} = -i\left(\overleftarrow{\nabla}_i - \overleftarrow{\nabla}_j\right)/2$, $\vec{\sigma}_i$ is the Pauli spin operator, and P_{ij}^{σ} is the spin exchange operator . The Skyrme parameters t_0 and t_3 are associated with volume properties, x_0 and x_3 are associated with symmetry volume properties and α is associated with both. The parameters t_1, t_2, x_1, and x_2 are associated with the volume, surface, symmetry volume and symmetry surface properties, respectively, and W_0 is associated with spin properties. The right and left arrows give the direction that the momentum operators act.

The total energy E is found from the expectation value of the total Hamiltonian, H, with Φ with σ_i and τ_i suppressed in the arguemnts of the ϕ_i,

$$E = \langle\Phi|\mathrm{H}|\Phi\rangle =$$

$$-\frac{\hbar^2}{2}\sum_{i=1}^{A}\frac{1}{m_{\tau_i}}\int \phi_i^*(\vec{r})\,\nabla^2\phi_i(\vec{r})d\vec{r} + \sum_{i<j}^{A}\int \phi_i^*(\vec{r})\,\phi_j^*(\vec{r}')V(\vec{r},\vec{r}')\phi_i(\vec{r})\phi_j(\vec{r}')d\vec{r}d\vec{r}'$$

$$-\sum_{i<j}^{A}\int \phi_i^*(\vec{r})\,\phi_j^*(\vec{r}')V(\vec{r},\vec{r}')\phi_i(\vec{r}')\phi_j(\vec{r})d\vec{r}d\vec{r}'. \tag{2.7}$$

The variational method is then used with the following requirement that

$$\langle\delta\Phi|\mathrm{H}|\Phi\rangle = 0, \tag{2.8}$$

under the constraint, $\langle\phi_i(\vec{r}_i,\sigma_i,\tau_i)|\phi_i(\vec{r}_i,\sigma_i,\tau_i)\rangle = 1$ with ε_i as Lagrange multipliers

$$\delta\left(E - \sum_i^A \varepsilon_i \int \phi_i^*(\vec{r})\phi_i(\vec{r})\,d\vec{r}\right) = 0, \qquad \delta = \frac{\partial}{\partial\phi_i^*(\vec{r})}\delta\phi_i^*(\vec{r}), \tag{2.9}$$

thus obtaining the HF equations with the ε_i being single particle energies,

$$-\frac{\hbar^2}{2m_{\tau_i}}\nabla^2\phi_i(\vec{r}) + \sum_j^A \int \phi_j^*(\vec{r}')\, V(\vec{r},\vec{r}')\phi_j(\vec{r}')\phi_i(\vec{r})d\vec{r}'$$

$$-\sum_j^A \int \phi_j^*(\vec{r}')\, V(\vec{r},\vec{r}')\phi_i(\vec{r}')\phi_j(\vec{r})d\vec{r}' = \varepsilon_i\phi_i(\vec{r}) \qquad (2.10)$$

The first term is the kinetic energy term, the second term is related to the local direct potential, and the third term is related to the non-local exchange potential. Note for $\vec{r} = \vec{r}'$ the potential terms cancel each other. The HF equations are *A* coupled integro-differential equations that cannot be solved analytically but only numerically through an iterative process of guessing the initial set of single particle orbits $\phi_j(\vec{r})$ and obtaining the new set of $\phi_i(\vec{r})$ until convergence is reached. This is also known as the self-consistent field method.

The total energy *E* of the system and the corresponding mean-field V_{HF} are given by

$$E = \int H\big(\rho_p(r), \rho_n(r)\big)\, d^3r, \qquad V_{HF} = \frac{\delta H_I}{\delta \rho} \qquad (2.11)$$

respectively, where $H\big(\rho_p(r), \rho_n(r)\big)$ is the total Skyrme energy-density functional [37], obtained using Eq. (2.6). H_I is the energy-density functional associated with the Skyrme and Coulomb interactions excluding the kinetic part. It is given by [36],

$$H = K + H_I = K + H_0 + H_3 + H_{eff} + H_{fin} + H_{so} + H_{sg} + H_{Coul}\,, \qquad (2.12)$$

where,

$$K = \frac{\hbar^2}{2m_p}\tau_p + \frac{\hbar^2}{2m_n}\tau_n\,, \qquad (2.13)$$

is the kinetic-energy term. For the Skyrme interaction of Eq. (2.6), we have

$$H_0 = \frac{1}{4}t_0\big[(2+x_0)\rho^2 - (2x_0+1)\big(\rho_p^2 + \rho_n^2\big)\big], \qquad (2.14)$$

$$H_3 = \frac{1}{24} t_3 \rho^{\alpha} \left[(2 + x_3)\rho^2 - (2x_3 + 1)\left(\rho_p^2 + \rho_n^2\right) \right], \tag{2.15}$$

$$H_{eff} = \frac{1}{8}[t_1(2 + x_1) + t_2(2 + x_2)]\tau\rho + \frac{1}{8}[t_2(2x_2 + 1) - t_1(2x_1 + 1)]\left(\tau_p\rho_p + \tau_n\rho_n\right), \tag{2.16}$$

$$H_{fin} = \frac{1}{32}[3t_1(2 + x_1) - t_2(2 + x_2)]\left(\vec{\nabla}\rho\right)^2 - \frac{1}{32}[3t_1(2x_1 + 1) + t_2(2x_2 + 1)]\left[\left(\vec{\nabla}\rho_p\right)^2 + \left(\vec{\nabla}\rho_n\right)^2\right], \tag{2.17}$$

$$H_{so} = \frac{W_0}{2}\left[\vec{J} \cdot \vec{\nabla}\rho + x_w\left(\overrightarrow{J_p} \cdot \vec{\nabla}\rho_p + \overrightarrow{J_n} \cdot \vec{\nabla}\rho_n\right)\right], \tag{2.18}$$

and

$$H_{sg} = -\frac{1}{16}(t_1 x_1 + t_2 x_2)J^2 + \frac{1}{16}(t_1 - t_2)\left(J_p^2 + J_n^2\right), \tag{2.19}$$

which are calculated in Ref [18]. ρ_τ is the nucleon density, τ_τ is the kinetic energy density, and $\overrightarrow{J_\tau}$ is the spin current density with subscript $\tau = p\ (n)$ for protons (neutrons). Here, H_0 is the zero-range term, H_3 is the density dependent term, H_{eff} is an effective-mass term, H_{fin} is a finite-range term, H_{so} is a spin-orbit term, H_{sg} is a term that is due to tensor coupling with spin and gradient and H_{Coul} is the contribution to the energy-density that is due to the Coulomb interaction. In Eqs. (2.14) – (2.19) $\rho = \rho_p + \rho_n$, $\tau = \tau_p + \tau_n$, and $\vec{J} = \overrightarrow{J_p} + \overrightarrow{J_n}$, are the total particle number density, total kinetic energy-density and total spin-density with *p* and *n* denoting the protons and neutrons, respectively [36]. Note that the additional parameter x_w, introduced in Eq. (2.18), allows us to modify the isospin dependence of the spin-orbit term.

The contribution to the energy-density, Eq. (2.12), from the Coulomb interaction can be written as a sum of a direct and an exchange terms:

$$H_{Coul}(r) = H_{Coul}^{dir}(r) + H_{Coul}^{ex}(r). \tag{2.20}$$

For the direct term it is common to adopt the expression

$$H_{Coul}^{dir}(r) = \frac{1}{2}e^2\rho_p(r)\int\frac{\rho_p(r')}{|r-r'|}d^3r' \ , \tag{2.21}$$

and for the corresponding exchange term to use the Slater approximation

$$H_{Coul}^{ex}(r) = -\frac{3}{4}e^2\rho_p(r)\left[\frac{3\rho_p(r)}{\pi}\right]^{1/3} . \tag{2.22}$$

It is very important to emphasize that the definitions of Eqs. (2.21) and (2.22) are not for the bona fide direct and exchange terms since each of them includes the contributions of the self-interaction term, which appear in opposite signs and cancel out in Eq. (2.20), see Ref. [38].

The HF approach applied to finite nuclei violates translational invariance, introducing a spurious center of mass (CM) motion. Thus, one must extract the contributions of the CM motion to the binding energy B, rms radii and other observables. To account for the CM correction to the total binding energy, one must subtract from it the so-called CM energy given as,

$$E_{CM} = \frac{1}{2mA}\langle\hat{P}^2\rangle \ , \tag{2.23}$$

where, $P = -i\hbar\sum_i \nabla_i$ is the total linear momentum operator.

During the last four decades, many Skyrme type effective nucleon-nucleon interactions of different forms were obtained by fitting the HF results to selected sets of experimental data [39,40]. We emphasize that we consider the specific form of Eq. (2.6) for the Skyrme type interaction. The values of the Skyrme parameters of the interactions adopted are listed in Table 1.

Table 1. Skyrme parameters. Values for the parameters for the following Skyrme interactions: SGII [23], KDE0 [24], KDE0v1 [24], SKM* [25], SK255 [26], SkI3 [41], SkI4 [41], SkI5 [41], SV-bas [42], SV-min [42], SV-sym32 [42], SV-m56-O [43], SV-m64-O [43], SLy4 [36], SLy5 [36], SLy6 [36], SkMP [44], SkP [45], SkO' [46], SkO [46], LNS [47], MSL0 [48], NRAPR [49] SQMC650 [50], SQMC700 [50], SkT1 [51], SkT2 [51], SkT3 [51], SkT8 [51], SkT9 [51], SkT1* [51], SkT3* [51], Skxs20 [52], and Z_σ [53]. These parameters are given in the following units: t_0 [MeV fm^3], t_1 [MeV fm^5], t_2 [MeV fm^5], t_3 [MeV fm$^{3(\alpha+1)}$], W_0 [MeV], and the remaining parameters are dimensionless.

Force	t_0	t_1	t_2	t_3	W_0	x_0	x_1	x_2	x_3	X_w	α
SGII	-2645.00	340.00	-41.90	15595.00	105.00	0.0900	-0.0588	1.4250	0.0604	1.0000	1/6
KDE0	-2526.51	430.94	-398.38	14235.52	128.96	0.7583	-0.3087	-0.9495	1.1445	1.0000	0.1676
KDE0v1	-2553.08	411.70	-419.87	14603.61	124.41	0.6483	-0.3472	-0.9268	0.9475	1.0000	0.1673
SKM*	-2645.00	410.00	-135.00	15595.00	130.00	0.0900	0.0000	0.0000	0.0000	1.0000	1/6
SK255	-1689.35	389.30	-126.07	10989.60	95.39	-0.1461	0.1660	0.0012	-0.7449	1.0000	0.3563
SkI3	-1762.88	561.61	-227.09	8106.20	188.51	0.3083	-1.1722	-1.0907	1.2926	0.0000	1/4
SkI4	-1885.83	473.83	1006.86	9703.61	366.19	0.4051	-2.8891	-1.3252	1.1452	-0.9850	1/4
SkI5	-1772.91	550.84	-126.69	8206.25	123.63	-0.1171	-1.3088	-1.0487	0.3410	1.0000	1/4
SV-bas	-1879.64	313.75	112.68	12527.38	124.63	0.2585	-0.3817	-2.8236	0.1232	0.5474	0.3000
SV-min	-2112.25	295.78	142.27	13988.57	111.29	0.2439	-1.4349	-2.6259	0.2581	0.8255	0.2554
SV-sym32	-1883.28	319.18	197.33	12559.47	132.75	0.0077	-0.5943	-2.1692	-0.3095	0.4019	0.3
SV-m56-O	-1905.40	571.19	1594.80	8439.04	133.27	0.6440	-2.9737	-1.2553	1.7966	0.7949	0.2000
SV-m64-O	-2083.86	484.60	1134.35	10720.67	113.97	0.6198	-2.3327	-1.3059	1.2101	1.1042	0.2000
SLy4	-2488.91	486.82	-546.39	13777.00	123.00	0.8340	-0.3440	-1.0000	1.3540	1.0000	1/6
SLy5	-2484.88	483.13	-549.40	13763.00	126.00	0.7780	-0.3280	-1.0000	1.2670	1.0000	1/6
SLy6	-2479.50	462.18	-448.61	13673.00	122.00	0.8250	-0.4650	-1.0000	1.3550	1.0000	1/6
SkMP	-2372.24	503.62	57.28	12585.30	160.00	-0.1576	-0.4029	-2.9557	-0.2679	1.0000	1/6
SkP	-2931.70	320.62	-337.41	18708.97	100.00	0.2922	0.6532	-0.5373	0.1810	1.0000	1/6
SkO	-2103.65	303.35	791.67	13553.25	353.16	-0.2107	-2.8108	-1.4616	-0.4299	-1.1256	1/4
SkO'	-2099.42	301.53	154.78	13526.46	287.79	-0.0295	-1.3257	-2.3234	-0.1474	-0.5760	1/4
LNS	-2484.97	266.74	-337.14	14588.20	96.00	0.0628	0.6585	-0.9538	-0.0341	1.0000	0.1667
MSL0	-2118.06	395.20	-63.95	12857.70	133.30	-0.0709	-0.3323	1.3583	-0.2282	1.0000	0.2359
NRAPR	-2719.70	417.64	-66.69	15042.00	41.96	0.1615	-0.0480	0.0272	0.1361	1.0000	0.1442
SQMC650	-2462.70	436.10	-151.90	14154.50	110.50	0.1300	0.0000	0.0000	0.0000	1.3899	0.1667
SQMC700	-2429.10	371.00	-96.70	13773.60	104.60	0.1000	0.0000	0.0000	0.0000	1.3910	0.1667
SkT1	-1794.00	298.00	-298.00	12812.00	110.00	0.1540	-0.5000	-0.5000	0.0890	1.0000	1/3
SkT2	-1791.60	300.00	-300.00	12792.00	120.00	0.1540	-0.5000	-0.5000	0.0890	1.0000	1/3
SkT3	-1791.80	298.50	-99.50	12794.00	126.00	0.1380	-1.0000	1.0000	0.0750	1.0000	1/3
SkT8	-1892.50	367.00	-228.76	11983.00	109.00	0.4480	-0.5000	-0.5000	0.6950	1.0000	0.2850
SkT9	-1891.40	377.40	-239.16	11982.00	130.00	0.4410	-0.5000	-0.5000	0.6860	1.0000	0.2850
SkT1*	-1800.50	296.00	-296.00	12884.00	95.00	0.1570	-0.5000	-0.5000	0.0920	1.0000	1/3
SkT3*	-1800.50	296.00	-98.67	12884.00	95.00	0.1420	-1.0000	1.0000	0.0760	1.0000	1/3
Skxs20	-2885.24	302.73	-323.42	18237.49	162.73	0.1375	-0.2555	-0.6074	0.0543	0.0000	1/6
Z_σ	-1983.76	362.25	-104.27	11861.40	123.69	1.1717	0.0000	0.0000	1.7620	1.0000	1/4

It is very important to note that in determining the parameters of the Skyrme interaction, Eq. (2.6), several approximations, concerning the terms of Eqs. (2.13), (2.19), (2.20) and (2.23), were made in the HF calculations. These approximations, which should be taken into account for a proper application of the specific interaction in fully self-consistent HF based RPA calculations, are:

(i) **The kinetic term, Eq. (2.13)**. In some interactions the mass of the proton is taken to be equal to that of the neutron and a certain value for the nucleon mass is adopted. In other interactions the mass of the proton is taken to be different than that of the neutron.

(ii) **The spin-density terms, Eq**. **(2.19)**. In some interactions the contributions from the spin-density term as given by Eq. (2.19), are ignored. We note that contributions from Eq. (2.19) are crucial for the calculation of the Landau parameter $G_0^{'}$.

(iii) **The Coulomb term, Eq**. **(2.20)**. In some interactions the Coulomb term of Eq. (2.22) is omitted. It is important to note that by neglecting the exchange Coulomb term of Eq. (2.22), one neglects the bona fide Coulomb exchange term together with the spurious contribution of the self-interaction term. This leads to a contribution to Coulomb displacement energies, obtained from Eq. (2.21), which is in better agreement with experimental data [54], since in the HF calculations with Skyrme interactions one neglects the contributions due to charge symmetry breaking in the nucleon-nucleon interaction and the contribution to Coulomb energy associated with long range correlations.

Also, in some interactions the charge density is used in Eq. (2.20), instead of the point proton density.

(iv) **The center of mass correction, Eq. (2.23)**. Traditionally, one simplifies the computation of Eq. (2.23) by taking into account only the one-body parts of it, which can be easily achieved by replacing $\frac{1}{m} \rightarrow \frac{1}{m}\left[1 - \frac{1}{A}\right]$ in the kinetic-energy term. In this case, the effects of neglecting the two-body part of Eq. (2.23) are compensated by renormalization of the force parameters. This may induce in the forces an incorrect trend with respect to the nucleon number A that becomes visible in the nuclear matter properties. A more appropriate approach, used in some interactions, is to take into account the contribution of the two body terms by using the HF single particle wavefunctions or by employing a simple scheme to evaluate Eq. (2.23).

The approximations that were used to obtain the Skyrme interactions adopted are listed for each interaction in Table 2.

Table 2. Force Options. Same as Table 1 with the following conditions defining the interactions: HBTM, for proton and neutron $\hbar^2/2m$ = 20.7525 MeV fm^2 for 0, for proton $\hbar^2/2m$ = 20.7213 MeV fm^2 and neutron $\hbar^2/2m$ = 20.7498 MeV fm^2 for 1, and for proton and neutron $\hbar^2/2m$ = 20.7355 MeV fm^2 for 2, JTM, contribution to the spin-orbit potential from t_1 and t_2 is taken for 1 and not for 0, CEX, coulomb-exchange on for 1 and off for 0, RHOC, proton-density is used for coulomb potential for 0 and charge-density is used for coulomb potential for 1, and ZPE, center of mass correction is taken as (1-1/A) factor on the mass for 1 and is computed explicitly a posteriori as $E_{CM} = \frac{1}{2mA}\langle \hat{P}^2 \rangle$ for 0.

Force	HBTM	JTM	CEX	RHOC	ZPE
SGII	0	0	1	0	0
KDE0	2	1	0	0	1
KDE0v1	2	1	0	0	1
SKM*	0	0	1	0	0
SK255	2	1	0	0	1
SkI3	0	0	1	0	1
SkI4	0	0	1	0	1
SkI5	0	0	1	0	1
SV-bas	1	0	1	0	1
SV-min	1	0	1	0	1
SV-sym32	1	0	1	0	1
SV-m56-O	1	0	1	0	1
SV-m64-O	1	0	1	0	1
SLy4	2	0	1	0	0
SLy5	2	1	1	0	0
SLy6	2	0	1	0	1
SkMP	0	0	1	0	0
SkP	2	1	1	0	0
SkO	2	0	1	0	1
SkO'	2	1	1	0	1
LNS	2	0	1	0	0
MSL0	2	1	0	0	1
NRAPR	2	1	1	0	1
SQMC650	2	0	1	0	0
SQMC700	2	0	1	0	0
SkT1	1	1	1	1	0
SkT2	1	1	1	1	0
SkT3	1	1	1	1	0
SkT8	1	1	1	1	0
SkT9	1	1	1	1	0
SkT1*	1	1	1	1	0
SkT3*	1	1	1	1	0
Skxs20	0	1	0	0	1
Z_σ	0	1	1	0	1

The matter densities, ρ, kinetic energy densities, τ, and spin current densities, $\vec{J}$, are given by the following equations in terms of the single particle wave functions.

$$\rho_\tau(\vec{r}) = \sum_{i=1}^{A} \sum_\sigma \phi_i^*(\vec{r},\sigma,\tau)\phi_i(\vec{r},\sigma,\tau) \qquad \rho(\vec{r}) = \sum_\tau \rho_\tau(\vec{r}) \tag{2.24}$$

$$\tau_\tau(\vec{r}) = \sum_{i=1}^{A} \sum_\sigma \vec{\nabla}\phi_i^*(\vec{r},\sigma,\tau)\vec{\nabla}\phi_i(\vec{r},\sigma,\tau) \qquad \tau(\vec{r}) = \sum_\tau \tau_\tau(\vec{r}) \tag{2.25}$$

$$\vec{J}_\tau(\vec{r}) = -i \sum_{i=1}^{A} \sum_{\sigma\sigma'} \phi_i^*(\vec{r},\sigma,\tau)\left[\vec{\nabla}\phi_i(\vec{r},\sigma',\tau) \times \langle\sigma|\vec{\sigma}|\sigma'\rangle\right] \quad \vec{J}(\vec{r}) = \sum_\tau \vec{J}_\tau(\vec{r}) \tag{2.26}$$

The variational method is then used with the following requirement that

$$\langle \delta\Phi | H | \Phi \rangle = 0, \tag{2.27}$$

under the constraint, $\sum_{\sigma,\tau} \int \rho_{\sigma,\tau}\, d\vec{r} = A$, where A is the number of nucleons in the nucleus. The Skyrme HF equations are then found [18] with

$$\frac{\delta}{\delta\rho_{\sigma,\tau}}\left(E - \sum_{\sigma,\tau} \varepsilon_i \int \rho_{\sigma,\tau}\, d\vec{r}\right) = 0\ ; \tag{2.28}$$

$$\delta E = \sum_{\sigma,\tau} \int \left(\frac{\hbar^2}{2m_\tau^*(\vec{r})} \delta\tau_{\sigma,\tau}(\vec{r}) + U_\tau(\vec{r})\delta\rho_{\sigma,\tau}(\vec{r}) + W_\tau(\vec{r})\delta\vec{J}_{\sigma,\tau}(\vec{r}) \right) d\vec{r}. \tag{2.29}$$

$\delta\tau_{\sigma,\tau}(\vec{r})$, $\delta\rho_{\sigma,\tau}(\vec{r})$, and $\delta\vec{J}_{\sigma,\tau}(\vec{r})$ are the variations of the kinetic energy densities, matter densities, and spin current densities, respectively. $m_\tau^*(\vec{r})$, $U_\tau(\vec{r})$, and $W_\tau(\vec{r})$ are the effective mass, the central potential, and the spin-orbit potential, respectively and given in terms of the current densities, charge density, matter densities, and the Skyrme parameters as the following,

$$\frac{\hbar^2}{2m_\tau^*(\vec{r})} = \frac{\hbar^2}{2m_\tau} + \frac{1}{8}[t_1(2+x_1) + t_2(2+x_2)]\rho(\vec{r})$$

$$-\frac{1}{8}[t_1(1+2x_1) - t_2(1+2x_2)]\rho_\tau(\vec{r}), \tag{2.30}$$

$$U_\tau(\vec{r}) = t_0\left(1 + \frac{x_0}{2}\right)\rho(\vec{r}) - t_0\left(\frac{1}{2} + x_0\right)\rho_\tau(\vec{r}) + \frac{1}{8}[t_1(2+x_1) + t_2(2+x_2)]\tau(\vec{r})$$

$$-\frac{1}{8}[t_1(1+2x_1)+t_2(1+2x_2)]\tau_\tau(\vec{r})+\frac{\alpha+2}{24}t_3(2+x_3)\rho^{\alpha+1}(\vec{r})$$

$$-\frac{\alpha}{24}t_3(1+2x_3)\rho^{\alpha-1}(\vec{r})\left[\rho_p^2(\vec{r})+\rho_n^2(\vec{r})\right]-\frac{1}{12}t_3(1+2x_3)\rho^{\alpha}(\vec{r})\rho_\tau(\vec{r})$$

$$-\frac{1}{16}[3t_1(2+x_1)-t_2(2+x_2)]\vec{\nabla}^2\rho(\vec{r})+\frac{1}{16}[3t_1(1+2x_1)+t_2(1+2x_2)]\vec{\nabla}^2\rho_\tau(\vec{r})$$

$$-\frac{1}{2}W_0\left(\vec{\nabla}\vec{J}(\vec{r})+\vec{\nabla}\vec{J}_\tau(\vec{r})\right)+\delta_{\frac{1}{2},\tau}e^2\int\frac{\rho_p(\vec{r})}{|\vec{r}-\vec{r}'|}d\vec{r}', \tag{2.31}$$

$$W_\tau(\vec{r})=\frac{1}{2}W_0\left(\vec{\nabla}\rho(\vec{r})+\vec{\nabla}\rho_\tau(\vec{r})\right)+\frac{1}{8}(t_1-t_2)\vec{J}_\tau(\vec{r})-\frac{1}{8}(t_1x_1-t_2x_2)\vec{J}(\vec{r}) \tag{2.32}$$

Because time-reversal invariance is required, $\delta\phi_{\bar{\imath}}(\vec{r},\sigma,\tau)=-2\sigma\delta\phi_i^*(\vec{r},-\sigma,\tau)$[18].

Therefore, the expressions for $\delta\tau_{\sigma,\tau}(\vec{r})$, $\delta\rho_{\sigma,\tau}(\vec{r})$, and $\delta\vec{J}_{\sigma,\tau}(\vec{r})$ can be simplified [18] to

$$\delta\tau_{\sigma,\tau}(\vec{r})=2\sum_{i,\sigma}\vec{\nabla}\delta\phi_i^*(\vec{r},\sigma,\tau)\cdot\vec{\nabla}\phi_i(\vec{r},\sigma,\tau) \tag{2.33}$$

$$\delta\rho_{\sigma,\tau}(\vec{r})=2\sum_{i,\sigma}\delta\phi_i^*(\vec{r},\sigma,\tau)\phi_i(\vec{r},\sigma,\tau) \tag{2.34}$$

$$\delta\vec{J}_{\sigma,\tau}(\vec{r})=-2i\sum_{i,\sigma_1,\sigma_2}\delta\phi_i^*(\vec{r},\sigma_1,\tau)\vec{\nabla}\phi_i(\vec{r},\sigma_2,\tau)\times\langle\sigma_1|\vec{\sigma}|\sigma_2\rangle \tag{2.35}$$

We then substitute $\delta\tau_{\sigma,\tau}(\vec{r})$, $\delta\rho_{\sigma,\tau}(\vec{r})$, and $\delta\vec{J}_{\sigma,\tau}(\vec{r})$ into equation (2.18b):

$$\sum_{i,\sigma_1}\int\delta\phi_i^*(\vec{r},\sigma_1,\tau)\left[\frac{\hbar^2}{2m_\tau^*(\vec{r})}\vec{\nabla}\phi_i(\vec{r},\sigma_1,\tau)\vec{\nabla}+U_\tau(\vec{r})\,\phi_i(\vec{r},\sigma_1,\tau)\right.$$

$$\left.-iW_\tau(\vec{r})\sum_{\sigma_2}\vec{\nabla}\times\langle\sigma_1|\vec{\sigma}|\sigma_2\rangle\phi_i(\vec{r},\sigma_2,\tau)-\varepsilon_i\phi_i(\vec{r},\sigma_1,\tau)\right]d\vec{r}=0. \tag{2.36}$$

All coefficients of the variation $\delta\phi_i^*(\vec{r},\sigma_1,\tau)=0$, so we achieve the following

$$\sum_{i,\sigma_1}\int\left[\frac{\hbar^2}{2m_\tau^*(\vec{r})}\vec{\nabla}\phi_i(\vec{r},\sigma_1,\tau)\vec{\nabla}+U_\tau(\vec{r})\,\phi_i(\vec{r},\sigma_1,\tau)\right.$$

$$\left.-iW_\tau(\vec{r})\sum_{\sigma_2}\vec{\nabla}\times\langle\sigma_1|\vec{\sigma}|\sigma_2\rangle\phi_i(\vec{r},\sigma_2,\tau)-\varepsilon_i\phi_i(\vec{r},\sigma_1,\tau)\right]d\vec{r}=0. \tag{2.37}$$

Finally, we derive the HF equations by integrating by parts [18]:

$$\left[-\vec{\nabla}\frac{\hbar^2}{2m_\tau^*(\vec{r})}\vec{\nabla}+U_\tau(\vec{r})-iW_\tau(\vec{r})\vec{\nabla}\times\vec{\sigma}\right]\phi_i(\vec{r},\sigma,\tau)=\varepsilon_i\phi_i(\vec{r},\sigma,\tau) \tag{2.38}$$

Assuming a closed-shell spherical nucleus, we use Eq. (2.5) to achieve the final form of the HF equations for spherical coordinates:

$$\frac{\hbar^2}{2m_\tau^*(\vec{r})}\left[-R_\alpha''(\vec{r})+\frac{l_\sigma(l_\sigma+1)}{r^2}R_\alpha(\vec{r})\right]-\frac{d}{dr}\left(\frac{\hbar^2}{2m_\tau^*(\vec{r})}\right)R_\alpha'(\vec{r})$$

$$+\left[U_\tau(\vec{r})+\frac{1}{r}\frac{d}{dr}\left(\frac{\hbar^2}{2m_\tau^*(\vec{r})}\right)+\frac{\left[j_\sigma(j_\sigma+1)-l_\sigma(l_\sigma+1)-\frac{3}{4}\right]}{r}W_\tau(\vec{r})\right]R_\alpha(\vec{r})=\varepsilon_\alpha R_\alpha(\vec{r}),\quad(2.39)$$

where $m_\tau^*(r)$, $U_\tau(r)$ and $W_\tau(r)$ are the effective mass, the potential and the spin orbit potential. They are given in terms of the Skyrme parameters and the nuclear densities. An initial guess is taken for the single-particle wave functions such as WS wave functions. The HF equations are then solved which produce a new set of wave functions which are then used until convergence is reached iteratively.

RPA calculations of strength functions

We have carried out fully self-consistent HF-based RPA calculations for electric giant resonances in ^{40}Ca, ^{48}Ca, and ^{208}Pb and using the EDF given by Eqs. (2.4) to (2.19) with Tables 1 and 2 and employing the numerical method for RPA described in Ref. [34, 55, 56],

$$C_n^+=\sum_{ph}\left[x_n^{ph}a_p^+a_h-y_n^{ph}a_h^+a_p\right];\quad(2.40)$$

$$|n\rangle=C_n^+|RPA\rangle_{G.S.};\quad(2.41)$$

$$C_n|RPA\rangle_{G.S.}=0\quad(2.42)$$

$$[H,C_n^+]|RPA\rangle_{G.S.}=(E_n-E_0)\,C_n^+|RPA\rangle_{G.S.}=(E_n-E_0)|n\rangle\quad(2.43)$$

where C_n^+ creates and annihilates HF particle-hole pairs in an N-dimensional particle-hole (p-h) space. $|RPA\rangle_{G.S.}$ is the RPA ground state. This is reformulated in terms of

coordinate like Q_n (time-even) and momentum like P^n (time-odd) p-h operators and adapted for a given EDF.

$$Q_n = \frac{1}{\sqrt{2\hbar\omega_n}}(C_n^+ + C_n) \qquad P^n = \sqrt{\frac{\hbar\omega_n}{2}}(C_n^+ - C_n) \tag{2.44}$$

x_n^{ph} and y_n^{ph} are the eigenvectors belonging to the RPA secular matrix:

$$\begin{pmatrix} A & B \\ -B & A \end{pmatrix}\begin{pmatrix} x_n^{ph} \\ y_n^{ph} \end{pmatrix} = E_n \begin{pmatrix} x_n^{ph} \\ y_n^{ph} \end{pmatrix}, \tag{2.45}$$

where A and B are symmetric $N \times N$ matrices and E_n are the RPA mode excitation energy eigenvalues of the RPA secular matrix. The values of $A_{mi,nj}$ and $B_{mi,nj}$ are given by the following expressions [57]:

$$A_{mi,nj} = (\epsilon_m - \epsilon_i)\delta_{mn}\delta_{ij} + \langle mj|V_{res}|in\rangle\ ; \tag{2.46}$$

$$B_{mi,nj} = \langle mn|V_{res}|ij\rangle\ ; \tag{2.47}$$

$$V_{res} = \frac{\delta^2 H}{\delta\rho_\tau \delta\rho'_\tau}\ ; \tag{2.48}$$

where V_{res} is the residual interaction and H is the Skyrme-HF EDF given by Eq. (2.12) and ϵ_m and ϵ_i are single-particle energies of HF p-h states.

We point out that in order to insure self-consistency we have carried out the calculations using a large p-h space and included all the terms of the p-h residual interaction (time-even and time-odd) which are associated with the EDF used in the HF calculations. No additional time-odd residual interactions were added. For a given scattering operator F_L, we have calculated the strength function

$$S(E) = \sum_j |\langle 0|F_L|j\rangle|^2 \delta\big(E_j - E_0\big). \tag{2.49}$$

Here, $|0\rangle$ is the RPA ground state, $|RPA\rangle_{G.S.}$, and the sum is over all RPA excited states $|j\rangle$ with the corresponding excitation energies E_j. We adopt the single particle scattering operator

$$F_L = \sum_i f(r_i) Y_{L0}(i) \,, \tag{2.50}$$

for isocalar (T = 0) excitations and

$$F_L = \frac{Z}{A}\sum_n f(r_n) Y_{L0}(n) - \frac{N}{A}\sum_p f(r_p) Y_{L0}(p) \,, \tag{2.51}$$

for isovector excitations (T = 1). In Eqs. (2.50) and (2.51) we use the operator $f(r) = r$, for the isovector dipole (T = 1, L = 1) and $f(r) = r^3 - (5/3)\langle r^2\rangle r$ for the isoscalar dipole (T = 0, L = 1), to eliminate possible contribution of the spurious state mixing [58,59]. For the isoscalar and isovector monopole (L = 0), quadrupole (L = 2) and octopole (L=3) excitations we use the operators r^2, r^2, and r^3, respectively. The nucleus is excited by a virtual photon. These operators are determined by the long wavelength limit, q is the photon momentum, (qr << 1) of the Bessel functions $j_l(qr)$ which correspond to the multipole decomposition of the photon plane wave involved in electromagnetic excitation of the giant resonance modes of the nucleus [57]. We then determine the energy moments of the strength function,

$$m_k = \int_0^\infty E^k S(E)\, dE \,. \tag{2.52}$$

The centroid energy, E_{CEN}, is then obtained from

$$\mathrm{E_{CEN}} = \frac{m_1}{m_0} \,. \tag{2.53}$$

The energy moment m_1 can also be calculated using the HF ground state wave function, thereby leading to an energy weighted sum rule (EWSR) [1, 10]. For the isoscalar F_L in Eq. (2.50), the EWSR is given by,

$$m_1(L, T=0) = \frac{1}{4\pi}\frac{\hbar^2}{2m}\int g_L(r)\,\rho(r) 4\pi r^2 dr\ , \tag{2.54}$$

where $\rho(r)$ is the HF ground-state matter density distribution and

$$g_L(r) = \left(\frac{df}{dr}\right)^2 + L(L+1)\left(\frac{f}{r}\right)^2\ . \tag{2.55}$$

For the isovector (T=1) operator F_L of Eq. (2.51), the EWSR is given by

$$m_1(L, T=1) = \frac{NZ}{A^2} m_1(L, T=0)\left[1 + \kappa - \kappa_{np}\right], \tag{2.56}$$

where κ is the enhancement factor which is due to the momentum dependence of the effective nucleon-nucleon interaction and is given by

$$\kappa = \frac{(1/2)[t_1(1+x_1/2)+t_2(1+x_1/2)]}{(\hbar^2/2m)(4NZ/A^2)}\ \frac{2\int g_L(r)\rho_p(r)\rho_n(r)4\pi r^2 dr}{\int g_L(r)\rho(r)4\pi r^2 dr}\ , \tag{2.57}$$

where t_i and x_i are the parameters of the Skyrme interaction. The correction κ_{np}, which arises because of the difference in the profiles of the neutron and proton density distributions [i.e., because $\rho_n(r) - \rho_p(r) \neq \frac{N-Z}{A}\rho(r)$], is given by

$$\kappa_{np} = \frac{(N-Z)}{A}\frac{A}{NZ}\frac{\int g_L(r)[Z\rho_n(r) - N\rho_p(r)]4\pi r^2 dr}{\int g_L(r)\rho(r)4\pi r^2 dr}\ . \tag{2.58}$$

We have carried out fully self-consistent Hartree-Fock (HF) based RPA calculations of the isoscalar giant monopole resonance (ISGMR), dipole (ISGDR), quadrupole (ISGQR), and the octopole (ISGOR) strength functions, adopting the scattering operator of Eq. (2.50), and for the isovector giant monopole resonance (IVGMR), dipole (IVGDR), quadrupole (IVGQR) and octopole (IVGOR) strength

functions, adopting the scattering operator of Eq. (2.51), for ^{40}Ca and for ^{48}Ca, using a wide range of 18 Skyrme type effective interactions (Table 1). In the next section we present the results of our calculations and compare with available experimental data**.**

Equation of state of nuclear matter

In the vicinity of the saturation density ρ_0 of symmetric NM, the EOS can be approximated by

$$E_0[\rho] = E[\rho_0] + \frac{1}{18} K_{NM} \left(\frac{\rho-\rho_0}{\rho_0}\right)^2, \tag{2.59}$$

$$\rho_0^2 \frac{dE/A}{d\rho}\Big|_{\rho_0} = 0 \tag{2.60}$$

where $E_0[\rho]$ is the binding energy per nucleon and K_{NM} is the incompressibility coefficient which is directly related to the curvature of the EOS, $K_{NM} = 9\rho_0^2 \frac{\partial^2 E_0}{\partial \rho^2}\Big|_{\rho_0}$. Similarly, the EOS of asymmetric NM, with proton density ρ_p and neutron density ρ_n, can be approximated by

$$E[\rho_p, \rho_n] = E_0[\rho] + E_{sym}[\rho] \left(\frac{\rho_n-\rho_p}{\rho}\right)^2, \tag{2.61}$$

where $E_{sym}[\rho]$ is the symmetry energy at matter density ρ, approximated as

$$E_{sym}[\rho] = J + \frac{1}{3} L \left(\frac{\rho-\rho_0}{\rho_0}\right) + \frac{1}{18} K_{sym} \left(\frac{\rho-\rho_0}{\rho_0}\right)^2, \tag{2.62}$$

where $J = E_{sym}[\rho_0]$ is the symmetry energy at saturation density ρ_0, $L = 3\rho_0 \frac{\partial E_{sym}}{\partial \rho}\Big|_{\rho_0}$, and $K_{sym} = 9\rho_0 \frac{\partial^2 E_{sym}}{\partial \rho^2}\Big|_{\rho_0}$. In terms of the Skyrme parameters, ρ_0, $E/A[\rho_0] = E_0[\rho_0]$, m*/m, K_{NM}, J, L, K_{sym}, and κ are given by the following [40] with $\beta = (3\pi^2/2)^{2/3}$ and $\gamma = 3t_1 + t_2(5 + 4x_2)$,

$$\beta\frac{\hbar^2}{5\mathrm{m}}\rho_0^{5/3}+\frac{3}{8}t_0\rho_0^2+\frac{\alpha+1}{16}t_3{\rho_0}^{\alpha+2}+\frac{1}{16}\beta\gamma{\rho_0}^{8/3}=0 \tag{2.63}$$

$$\frac{\mathrm{E}}{\mathrm{A}}(\rho_0)=\frac{H(\rho_0)}{\rho_0}=\beta\frac{3\hbar^2}{10\mathrm{m}}\rho_0^{2/3}+\frac{3}{8}t_0\rho_0+\frac{1}{16}t_3{\rho_0}^{\alpha+1}+\frac{3}{80}\beta\gamma\rho_0^{5/3} \tag{2.64}$$

$$\mathrm{m}^*/\mathrm{m}=\left(1+\gamma\frac{\mathrm{m}}{8\hbar^2}\rho_0\right)^{-1} \tag{2.65}$$

$$\mathrm{J}=\beta\frac{\hbar^2}{6\mathrm{m}}\rho_0^{2/3}-\frac{1}{8}t_0(2x_0+1)\rho_0+\frac{1}{24}\beta[t_2(5+4x_2)-3t_1x_1]\rho_0^{5/3}$$

$$-\frac{1}{48}t_3(2x_3+1){\rho_0}^{\alpha+1} \tag{2.66}$$

$$\mathrm{L}=\beta\frac{\hbar^2}{3\mathrm{m}}\rho_0^{2/3}-\frac{3}{8}t_0(2x_0+1)\rho_0+\frac{5}{24}\beta[t_2(5+4x_2)-3t_1x_1]\rho_0^{5/3}$$

$$-\frac{1}{16}t_3(2x_3+1)(\alpha+1){\rho_0}^{\alpha+1} \tag{2.67}$$

$$\mathrm{K_{sym}}=-\beta\frac{\hbar^2}{3\mathrm{m}}\rho_0^{2/3}+\frac{5}{12}\beta[t_2(5+4x_2)-3t_1x_1]\rho_0^{5/3}$$

$$-\frac{3}{16}t_3(2x_3+1)(\alpha+1)\alpha{\rho_0}^{\alpha+1} \tag{2.68}$$

$$\kappa=\frac{\mathrm{m}}{4\hbar^2}[t_1(2+x_1)+t_2(2+x_2)]\rho_0 \tag{2.69}$$

Table 3 contains the values of the physical quantities of symmetric nuclear matter associated with these Skyrme interactions: the binding energy per nucleon E/A, the saturation matter density ρ_0, the effective mass m*/m, the incompressibility coefficient of SNM, K_{NM}, the coefficients associated with the symmetry energy density J, L and K_{sym} at saturation density ρ_0 (Eq. (2.62)) and κ , the NM value of the enhancement factor of the EWSR of the IVGDR, Eqs (2.56), obtained from (2.57) with using the NM saturation matter density.

Table 3. Nuclear matter properties. Properties of symmetric nuclear matter at nuclear saturation density ρ_0 [fm^3] associated with the Skyrme interactions of Table 1. Also shown are the total binding energy per nucleon E/A [MeV], isoscalar effective mass m*/m, incompressibility modulus K_{NM} [MeV], the coefficients related to the symmetry energy density J [MeV], L [MeV] and K_{sym} [MeV], and the enhancement factor of the EWSR of the IVGDR, κ.

Force	E/A	ρ_0	m*/m	K_{NM}	J	L	K_{sym}	κ
SGII	15.59	0.159	0.79	215.0	26.80	37.63	-145.90	0.49
KDE0	16.11	0.161	0.72	228.8	33.00	45.22	-144.78	0.30
KDE0v1	16.23	0.165	0.74	227.5	34.58	54.70	-127.12	0.23
SKM*	15.78	0.160	0.79	216.7	30.03	45.78	-155.94	0.53
SK255	16.33	0.157	0.80	255.0	37.40	95.00	-58.33	0.54
SkI3	15.96	0.158	0.58	258.1	34.80	100.52	73.04	0.25
SkI4	15.92	0.160	0.65	247.9	29.50	60.39	-40.56	0.25
SkI5	15.83	0.156	0.58	255.7	36.70	129.33	159.57	0.25
SV-bas	15.90	0.160	0.90	234.0	30.00	45.21	-221.75	0.40
SV-min	15.91	0.161	0.95	222.0	30.01	44.76	-156.57	0.08
SV-sym32	15.94	0.159	0.90	233.8	32.00	57.07	-148.79	0.40
SV-m56-O	15.81	0.157	0.56	254.6	27.00	49.96	-45.04	0.60
SV-m64-O	15.82	0.159	0.64	241.4	27.01	30.63	-144.76	0.60
SLy4	15.97	0.160	0.70	229.9	32.00	45.96	-119.73	0.25
SLy5	15.98	0.160	0.70	229.9	32.03	48.27	-112.76	0.25
SLy6	15.92	0.159	0.69	229.8	31.96	47.44	-112.71	0.25
SkMP	15.56	0.157	0.65	230.9	29.88	70.31	-49.82	0.71
SkP	15.93	0.162	1.00	200.8	32.98	45.21	-266.60	0.30
SkO	15.84	0.160	0.90	223.3	31.97	79.14	-43.17	0.17
SkO'	15.75	0.160	0.90	222.3	31.95	68.93	-78.82	0.15
LNS	15.32	0.175	0.83	210.8	33.43	61.45	-127.36	0.38
MSL0	16.00	0.160	0.80	230.0	30.00	60.00	-99.33	0.43
NRAPR	15.85	0.161	0.69	225.7	32.78	59.63	-123.32	0.66
SQMC650	15.57	0.172	0.78	218.1	33.65	52.92	-173.15	0.59
SQMC700	15.49	0.171	0.76	222.2	33.47	59.06	-140.84	0.56
SkT1	15.98	0.161	1.00	236.2	32.02	56.18	-134.83	0.00
SkT2	15.94	0.161	1.00	235.7	32.00	56.16	-134.67	0.00
SkT3	15.95	0.161	1.00	235.7	31.50	55.31	-132.05	0.00
SkT8	15.94	0.161	0.83	235.7	29.92	33.72	-187.52	0.20
SkT9	15.88	0.160	0.83	234.9	29.76	33.74	-185.62	0.20
SkT1*	16.20	0.162	1.00	239.0	32.31	56.58	-136.66	0.00
SkT3*	16.20	0.162	1.00	239.0	31.97	56.32	-133.65	0.00
Skxs20	15.79	0.162	0.96	201.8	35.49	67.07	-122.25	0.08
Z_σ	15.88	0.163	0.78	233.3	26.69	-29.38	-401.43	0.51

CHAPTER III

GIANT RESONANCES IN ^{40}CA AND ^{48}CA*

We now present results of our fully self-consistent HF based RPA calculations of the strength functions and centroid energies of isoscalar and isovector giant resonances of multipolarities L = 0 - 3 in ^{40}Ca and ^{48}Ca [60], obtained for 18 widely used Skyrme type interactions shown in Table 1: SGII [23], KDE0 [24], KDE0v1 [24], SKM* [25], SK255 [26], SkI3 [41], SkI4 [41], SkI5 [41], SV-bas [42], SV-min [42], SV-m56-O [43], SV-m64-O [43], SLy4 [36], SLy5 [36], SLy6 [36], SkMP [44], SkP [45], and SkO' [46]. These interactions are associated with the ranges of NM properties (see Table 3): E/A = 15.56 – 16.33 MeV, ρ_0 = 0.156 - 0.165 fm^{-3}, K_{NM} = 201 – 258 MeV, J = 26.80 – 37.40 MeV, L = 31 – 129 MeV, K_{sym} = -267 – 160 MeV, m*/m = 0.56 – 1.00 and κ = 0.08 – 0.71.

In Figures 1-4 we display the HF-based RPA results (solid lines) for the distribution of the energy-weighted strength normalized to one (ES(E)/EWSR) for the isoscalar and isovector giant resonances of multipolarities L = 0-3 in ^{40}Ca and ^{48}Ca, obtained using the KDE0 [24] interaction that is representative of the strength distributions for the rest of the interactions. For the purpose of comparison with experiment a Lorenzian smearing of a 3 MeV width was used in the calculation. The experimental data [19,21] are shown as histograms.

---

* Part of this chapter is reprinted with permission from "Giant Resonances in ^{40}Ca and ^{48}Ca" by M. R. Anders *et. al.*, 2013. *Physical Review C*, **87**, 024303, Copyright [2013] by American Physical Society.

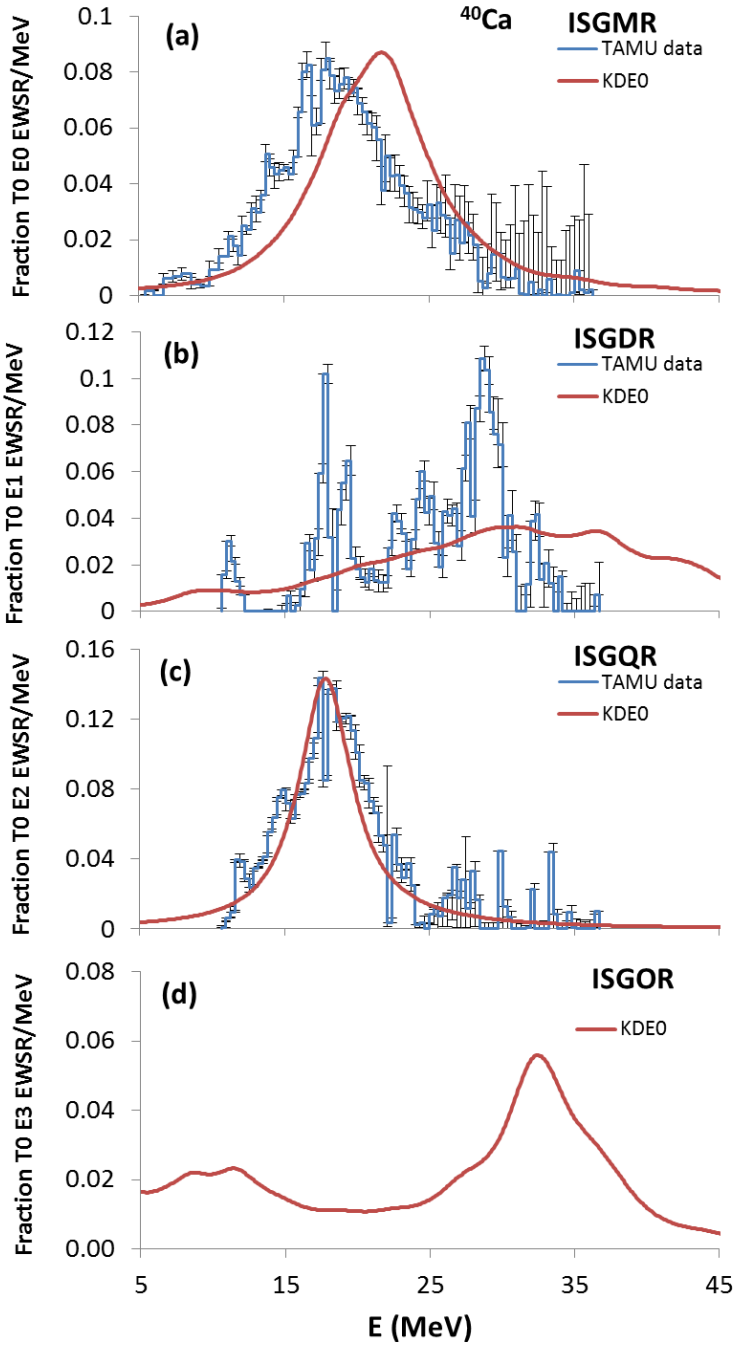

Figure 1 [60] Self-consistent HF-based RPA results (solid lines) for the distribution of the energy-weighted strength normalized to one (fraction of EWSR) for the isoscalar monopole (E0), dipole (E1), quadrupole (E2), and octopole (E3) in ^{40}Ca, obtained using the KDE0 [24] Skyrme interaction. A Lorenzian smearing of a 3 MeV width was used in the calculation. The experimental data [21] are shown as histograms.

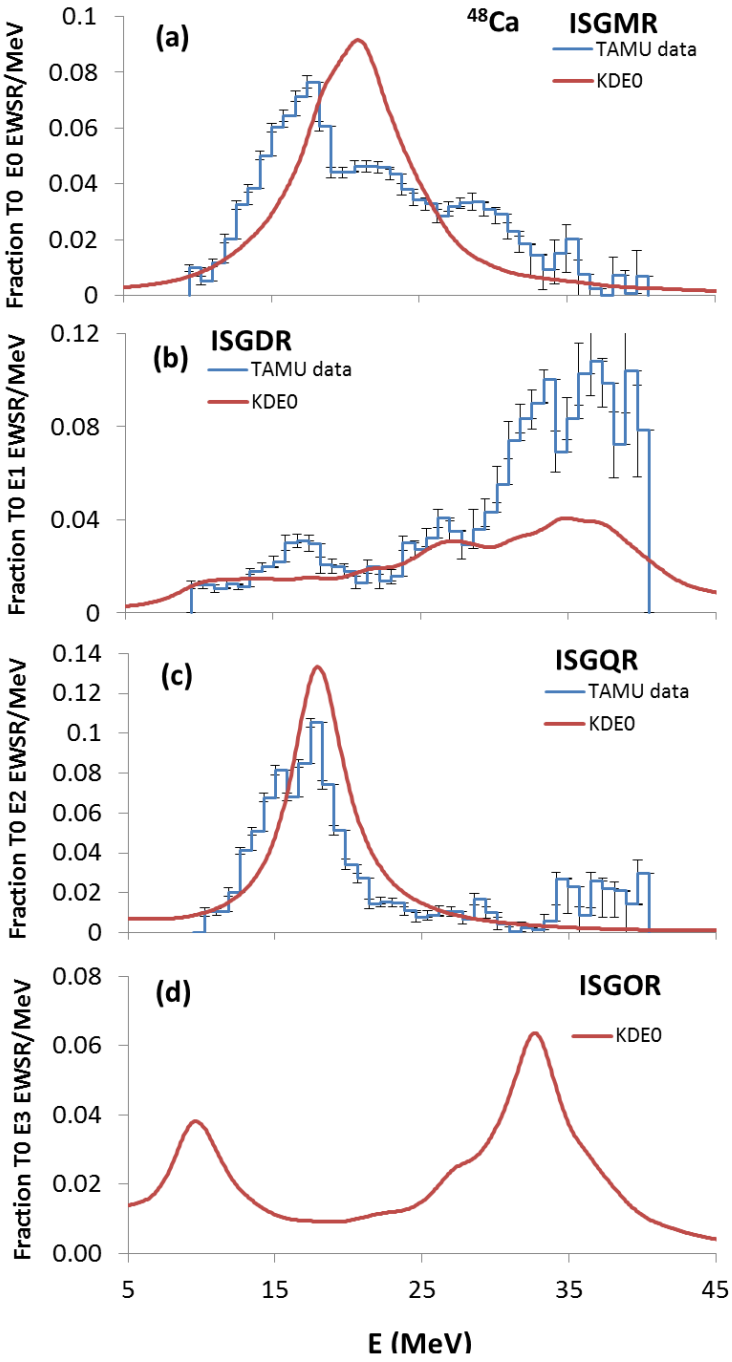

Figure 2 [60] Same as Fig. 1 except for ^{48}Ca. Experimental data is from Ref. [19].

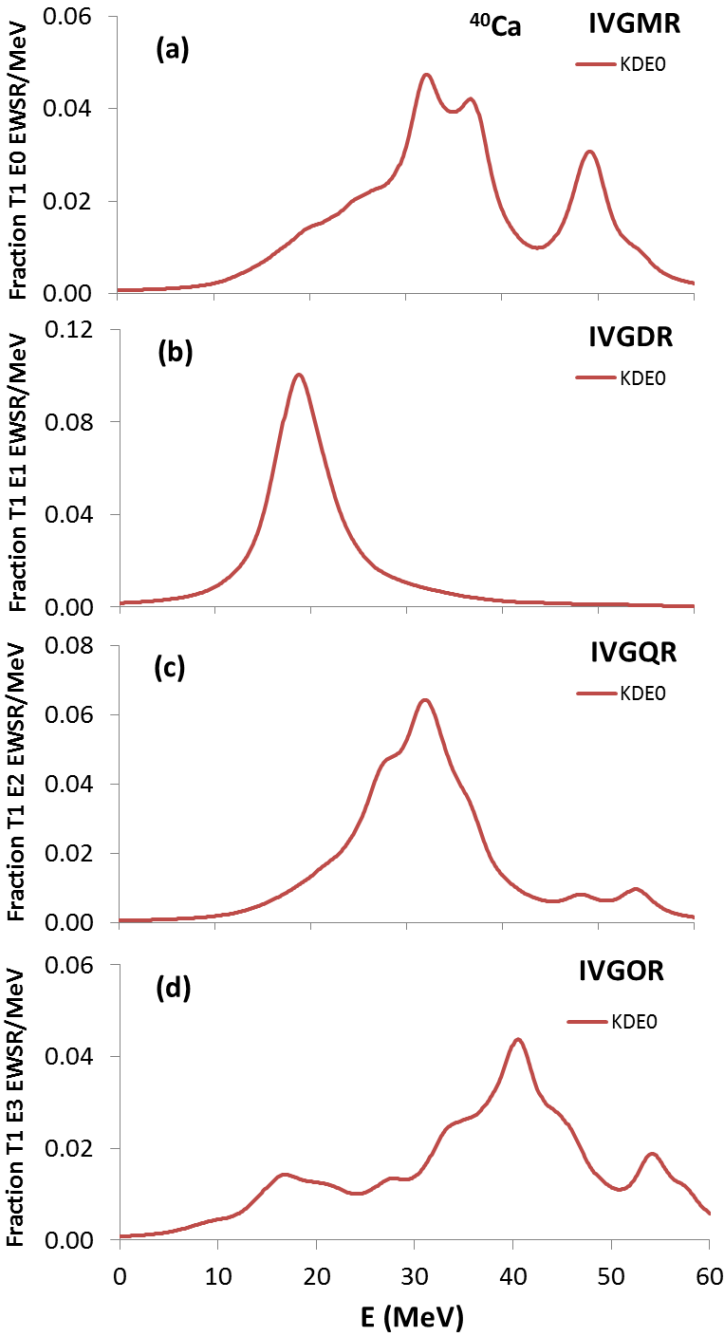

Figure 3 [60] Self-consistent HF-based RPA results (solid lines) for the distribution of the energy-weighted strength, normalized to one (fraction of EWSR), for the isovector monopole (E0), dipole (E1), quadrupole (E2), and octopole (E3) in ^{40}Ca, obtained using the KDE0 [24] Skyrme interaction. A Lorenzian smearing of a 3 MeV width was used in the calculation.

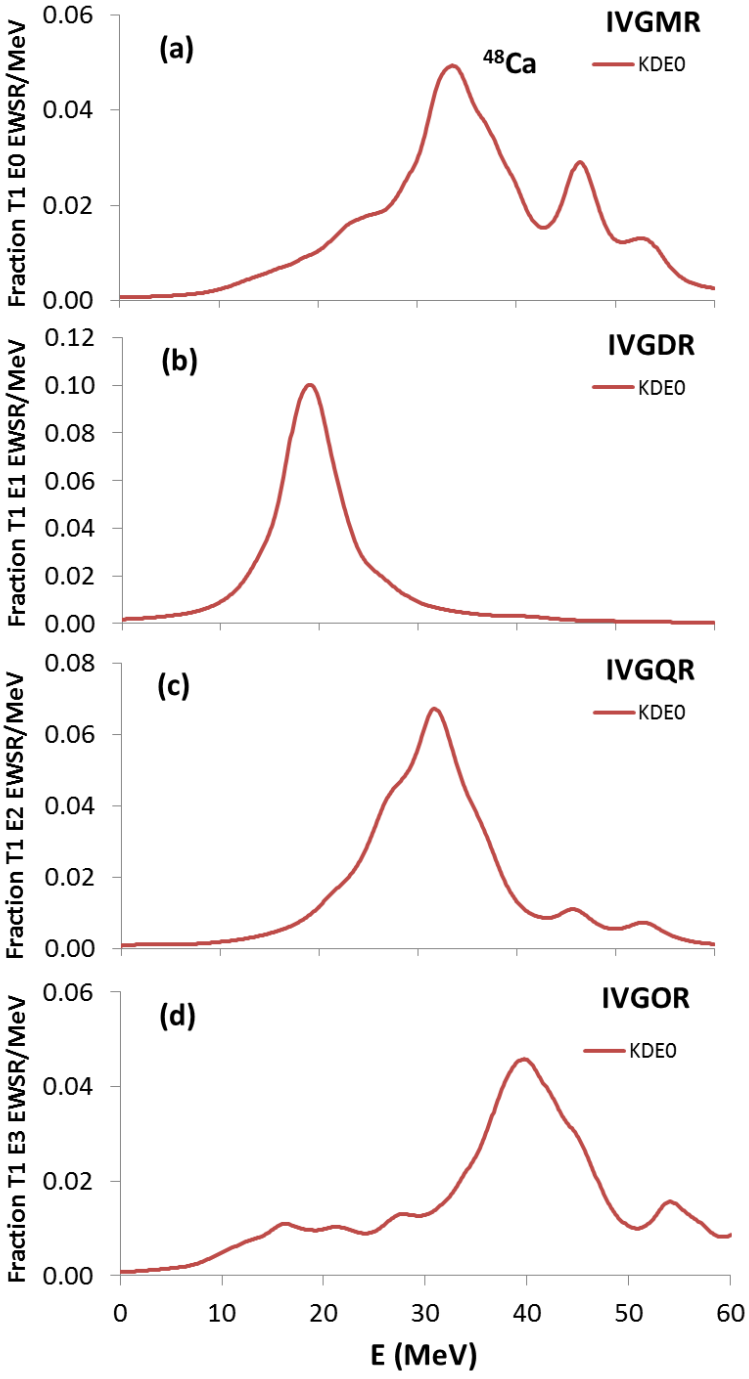

Figure 4 [60] Same as Fig. 3 except for ^{48}Ca.

To investigate the sensitivity of the energies of the giant resonances in ^{40}Ca and ^{48}Ca to NM properties (Table 3) we calculated the Pearson correlation coefficients (a measure of linear correlation) between the centroid energies E_{CEN}, Eq. (2.53), and the properties of NM. We used a small smearing width (0.05 MeV) to insure accuracy for E_{CEN}. For a proper comparison with experiment, we used the experimental excitation energy ranges in determining the centroid energies. We use the excitation energy range of 9.5 – 40 MeV [19,21] for the ISGMR and the ISGQR and the range of 20 – 40 MeV [19,21] for the ISGDR. For the ISGOR we use the appropriate excitation energy range of 20 – 60 MeV. We use the excitation energy range of 0 – 60 MeV for the IVGMR [10,61], the range of 0 – 40 MeV for the IVGDR [62,63,64], the range of 9 – 60 MeV for the IVGQR [65] and the range of 25 – 60 MeV for the IVGOR (see also Figures 1-4).

ISGMR

In Figure 5 we compare the experimental data [19,21] of the ISGMR centroid energies of ^{40}Ca (a), ^{48}Ca (b), and the energy difference, $\Delta E_{CEN} = E_{CEN}(^{48}Ca) - E_{CEN}(^{40}Ca)$, between ^{48}Ca and ^{40}Ca (c) with the results of fully self-consistent HF-based RPA calculations (full circles), obtained using the 18 Skyrme interactions from Table 1. The results obtained with violation of self-consistency, by the neglecting the Coulomb and the spin orbit particle-hole interactions in the RPA calculations, are shown in Fig. 5d. The calculated values are plotted as a function of K_{NM}. The experimental values of E_{CEN} = 19.18 +/- 0.37 MeV for ^{40}Ca, E_{CEN} = 19.88 +/- 0.16 MeV for ^{48}Ca [19,21] and their difference are shown in Figure 5 as the regions between the dashed lines.

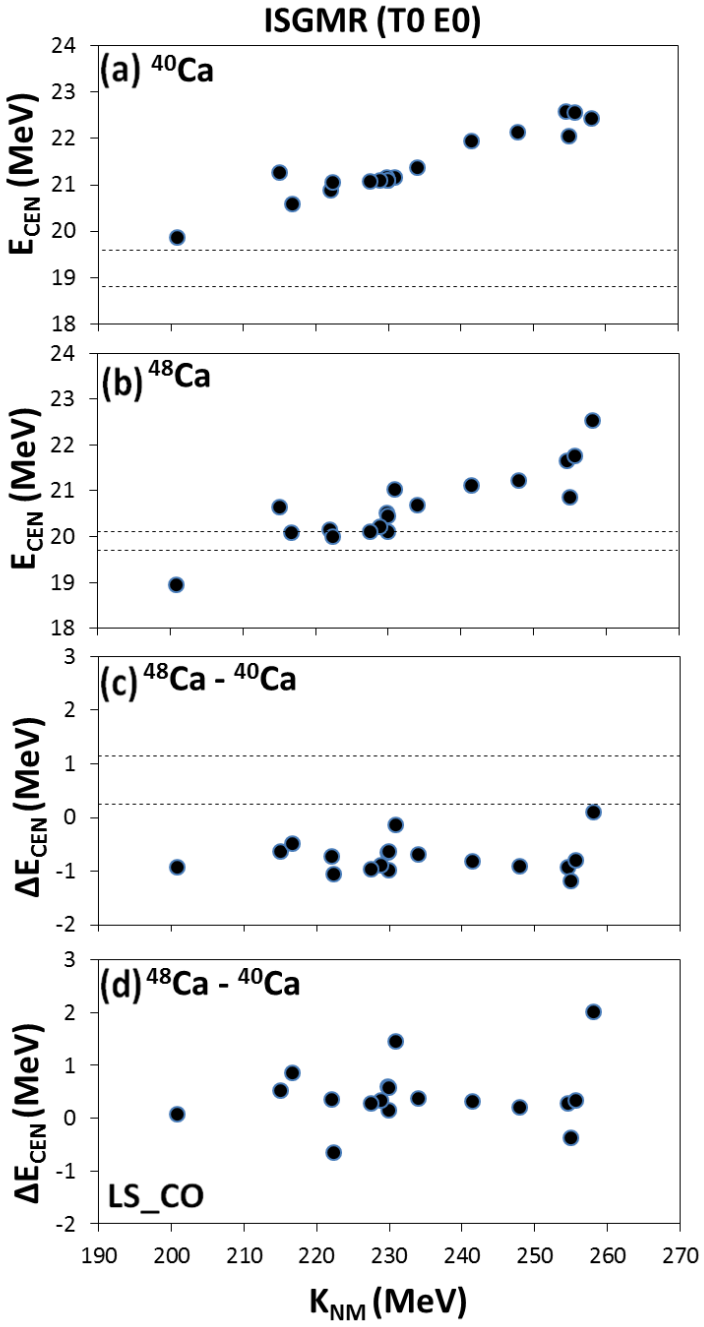

Figure 5 [60] Comparison of experimental data [19,21] of the ISGMR centroid energies of ^{40}Ca (a), ^{48}Ca (b), and the ^{48}Ca – ^{40}Ca energy difference (c), shown as the regions between the dashed lines, with the results of fully self-consistent HF based RPA calculations (full circles) obtained using the Skyrme interactions of Table 1, plotted vis. K_{NM}. The results obtained with violation of self-consistency in the RPA calculations, are shown in (d).

A very strong correlation between E_{CEN} of ^{40}Ca and E_{CEN} of ^{48}Ca can be seen with K_{NM}. This is expected, since the ISGMR centroid energy is very sensitive to the value of K_{NM} [1,3,8]. The ISGMR centroid energies for ^{40}Ca are all higher than the experimental value 19.18 +/- 0.37 MeV. The ^{48}Ca ISGMR centroid energies are more consistent with the experimental value 19.88 +/- 0.16 MeV. While the experimental data show that the ISGMR in ^{40}Ca lies at lower energy than in ^{48}Ca, 17 of the Skyrme interactions (Table 1) show the ISGMR in ^{40}Ca at a higher energy than in ^{48}Ca, while the 18th interaction (SkI3) shows them at essentially the same energy in ^{40}Ca and ^{48}Ca. For not fully self-consistent RPA calculations, the results for some interactions leads to spurious agreement with the experimental data for the ^{48}Ca – ^{40}Ca energy difference as can be seen in Figure 5d. We also found a medium correlation between the ISGMR energies and the effective mass m*/m, which is a reflection of the strong correlation between K_{NM} and m*/m seen in Figure 6 (see also Ref. [8]). Figure 6 also shows the correlation of the saturation symmetric NM density ρ_0 and the symmetry energy coefficient J with K_{NM} .

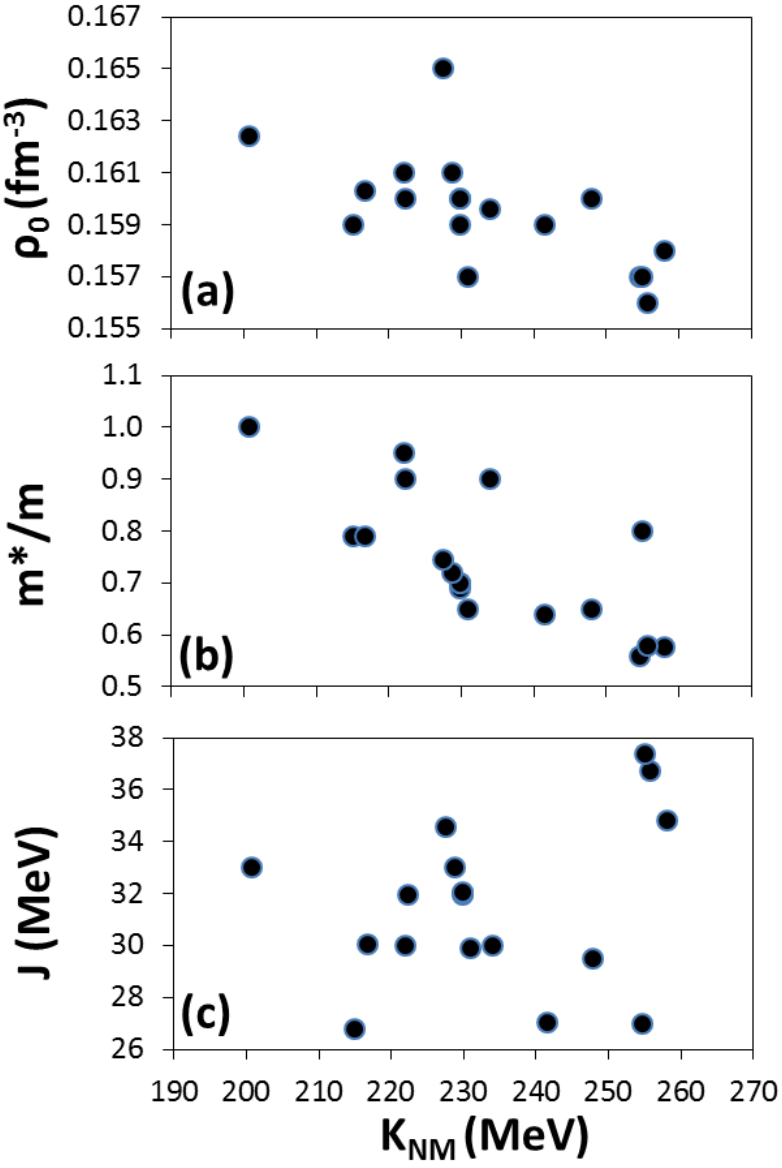

Figure 6 [60] The values of ρ_0, m*/m, and J are plotted vs. $K_{NM,}$ for the Skyrme interactions of Table 1.

To investigate the dependence of the energy difference $\Delta E_{CEN} = E_{CEN}(^{48}Ca) - E_{CEN}(^{40}Ca)$ between the ISGMR in ^{48}Ca and in ^{40}Ca on the symmetry energy density, Figure 7 shows the results of our fully self-consistent HF based RPA calculations (full circles), using the Skyrme interactions (Table 1) having nuclear matter symmetry energy coefficient J = 26.80 –36.7 MeV. No correlation is found between ΔE_{CEN} and J. Similar results were obtained for L, K_{sym} and K_{NM}, which can be easily understood as a reflection of the correlation of K_{sym}, J and K_{NM} with L shown in Figure 8.

Figure 9 shows the correlation of the ISGMR centroid energies with W_0, the strength of the spin-orbit interaction. There is a positive strong correlation between the ^{48}Ca - ^{40}Ca energy difference and W_0. Similar results were obtained for the ISGDR, ISGQR and the ISGOR.

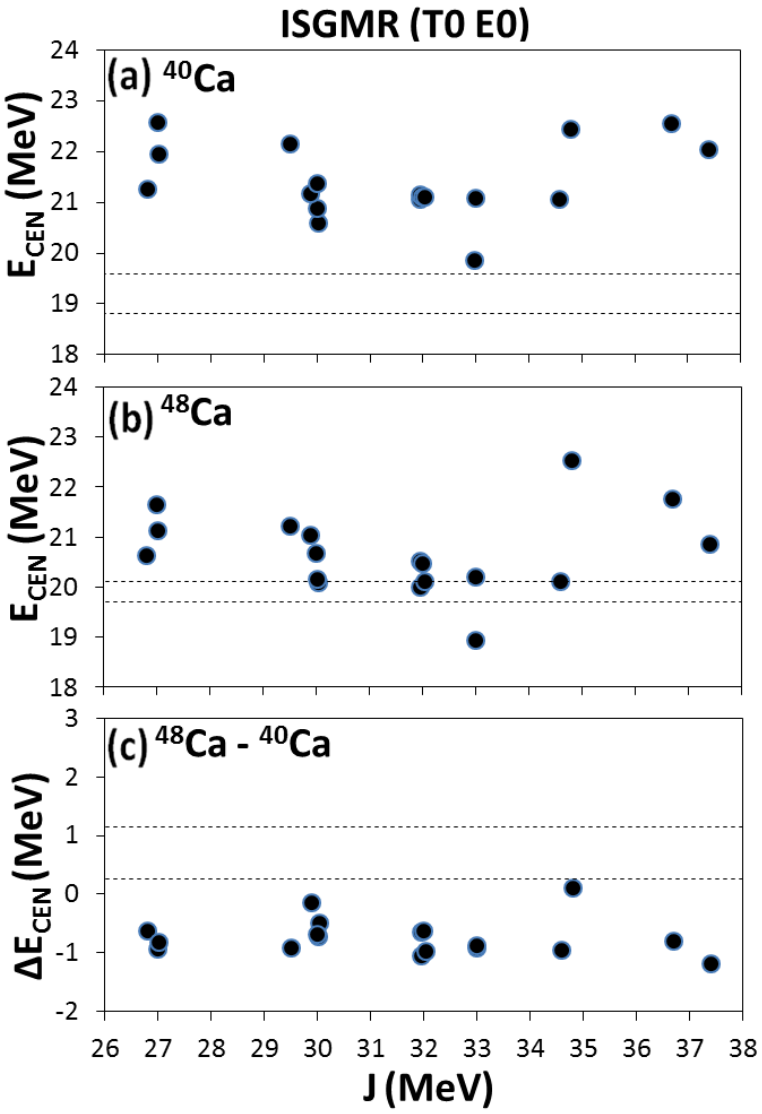

Figure 7 [60] The HF based RPA results (full circles) of the ISGMR centroid energies E_{CEN} of ^{40}Ca (a), ^{48}Ca (b) and the ^{48}Ca – ^{40}Ca energy difference (c), obtained using the Skyrme type interactions of Table 1, as a function of the NM symmetry energy at saturation density J. The limits on the experimental data are shown by the dashed lines.

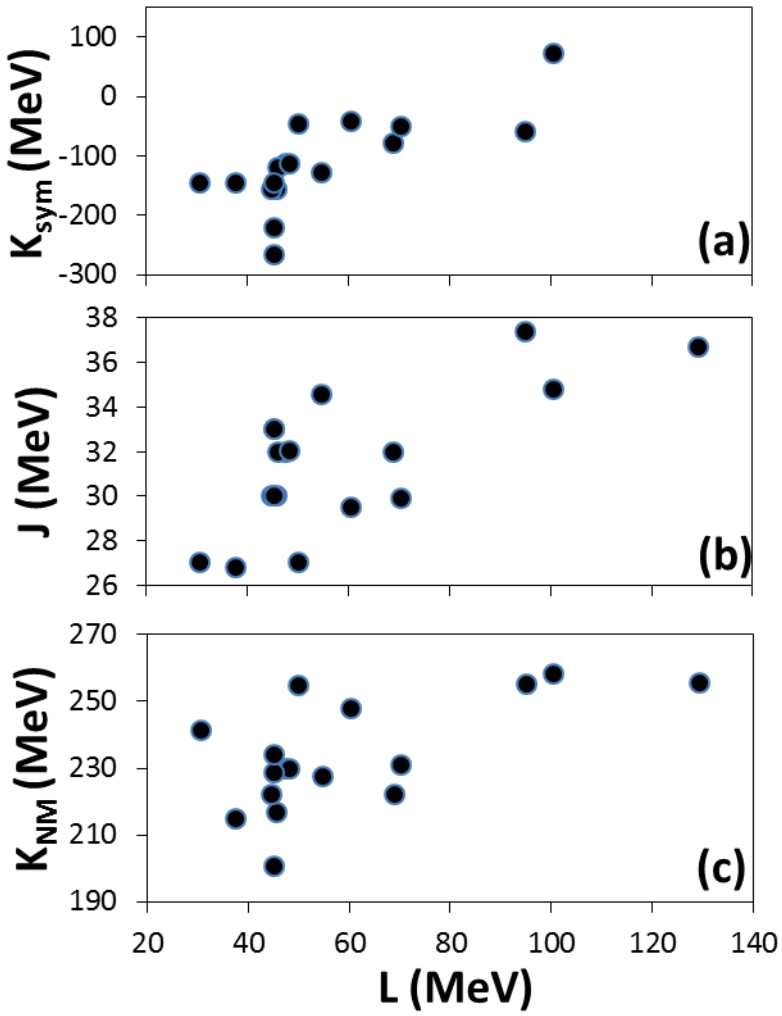

Figure 8 [60] The values of K_{sym}, J, and K_{NM} are plotted vs. L, for the Skyrme interactions of Table 1.

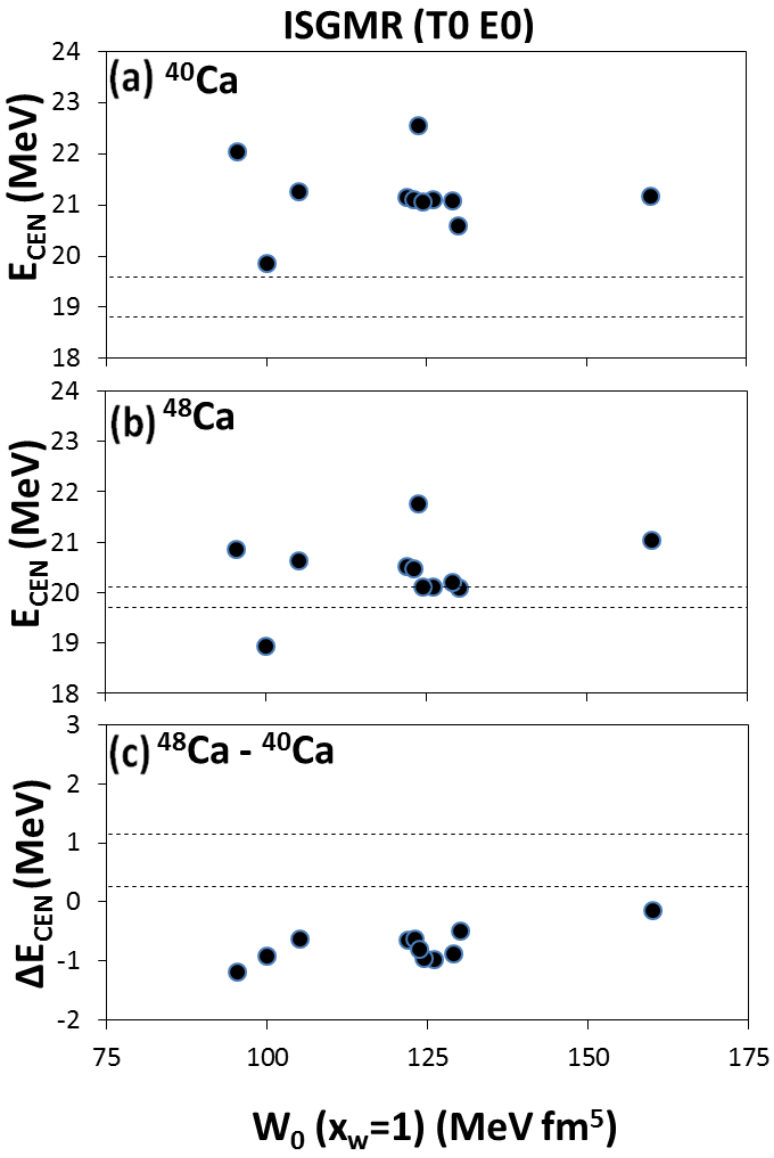

Figure 9 [60] Same as Figure 7 except as a function of the strength W_0 of the spin-orbit interaction.

ISGDR

In Figure 10 the results of the self-consistent HF-based RPA calculations (full circles) for the ISGDR centroid energies of ^{40}Ca (a), ^{48}Ca (b), and the ^{48}Ca – ^{40}Ca energy difference (c), are compared with the experimental data [19,21]. The experimental values of E_{CEN} = 23.36 +/- 0.70 MeV for ^{40}Ca, E_{CEN} = 27.30 +/- 0.15 MeV for ^{48}Ca and their difference are shown in Figure 10 as the regions between the dashed lines. The HF-RPA energies, obtained for the 18 interactions from Table 1, are plotted as a function of K_{NM}. For the 18 Skyrme interactions, the calculated ISGDR centroid energies are higher than the experimental values by 1.5 – 6 MeV and the calculated ^{48}Ca - ^{40}Ca energy difference, although positive, are smaller than the experimental value. We note that the experimental results for the fraction of the EWSR for the ISGDR in ^{48}Ca and ^{40}Ca are 137 +/- 20% and 62 +/- 20% [19,21], respectively, compared to the calculated values of 100%. Therefore, the comparison between the ISGDR in ^{48}Ca and ^{40}Ca might be misleading since only 62 +/- 20% of the EWSR of the ISGDR in ^{40}Ca was found experimentally. A strong correlation is also found between the ISGDR energy of ^{40}Ca with both K_{NM} and m*/m and similarly for ^{48}Ca.

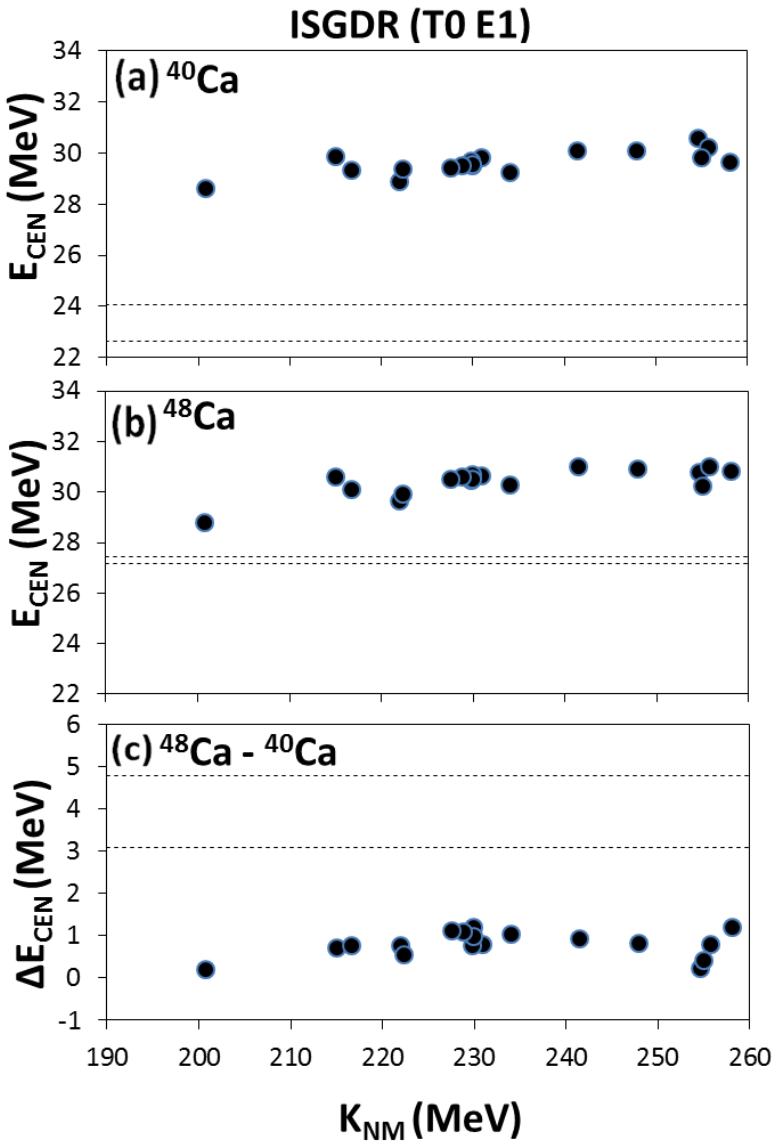

Figure 10 [60] Same as Figure 7 except for the ISGDR as a function of K_{NM}..

ISGQR

Figure 11 shows, as a function of m*/m, our HF based RPA results (full circles) of the ISGQR centroid energies E_{CEN}, of ^{40}Ca (a), ^{48}Ca (b), and the ^{48}Ca - ^{40}Ca energy difference (c), obtained using 18 Skyrme type interactions from Table 1. The experimental values of E_{CEN} = 17.84 +/- 0.43 MeV for ^{40}Ca [19], E_{CEN} = 18.61 +/- 0.24 MeV for ^{48}Ca [21] and their difference are shown in Figure 11 as the regions between the dashed lines. As seen in Figure 11, a very strong correlation exists between the ISGQR energy of ^{40}Ca with m*/m and similarly for ^{48}Ca. We find that interactions having m*/m = 0.65 – 0.8 reproducing the experimental data of the ISGQR.

ISGOR

Figure 12 shows our HF based RPA results (full circles) of the ISGOR centroid energies E_{CEN}, of ^{40}Ca (a), ^{48}Ca (b), and the ^{48}Ca - ^{40}Ca energy difference (c), using the 18 Skyrme type interactions from Table 1. A very strong correlation exists between the ISGOR of ^{40}Ca and ^{48}Ca with m*/m as can be seen in Figure 12. Using the result that interactions having m*/m = 0.65 – 0.8 reproduce the experimental data of the ISGQR we can predict the values of the E_{CEN} of the ISGOR in ^{40}Ca and ^{48}Ca to be in the region of 30 – 34 MeV.

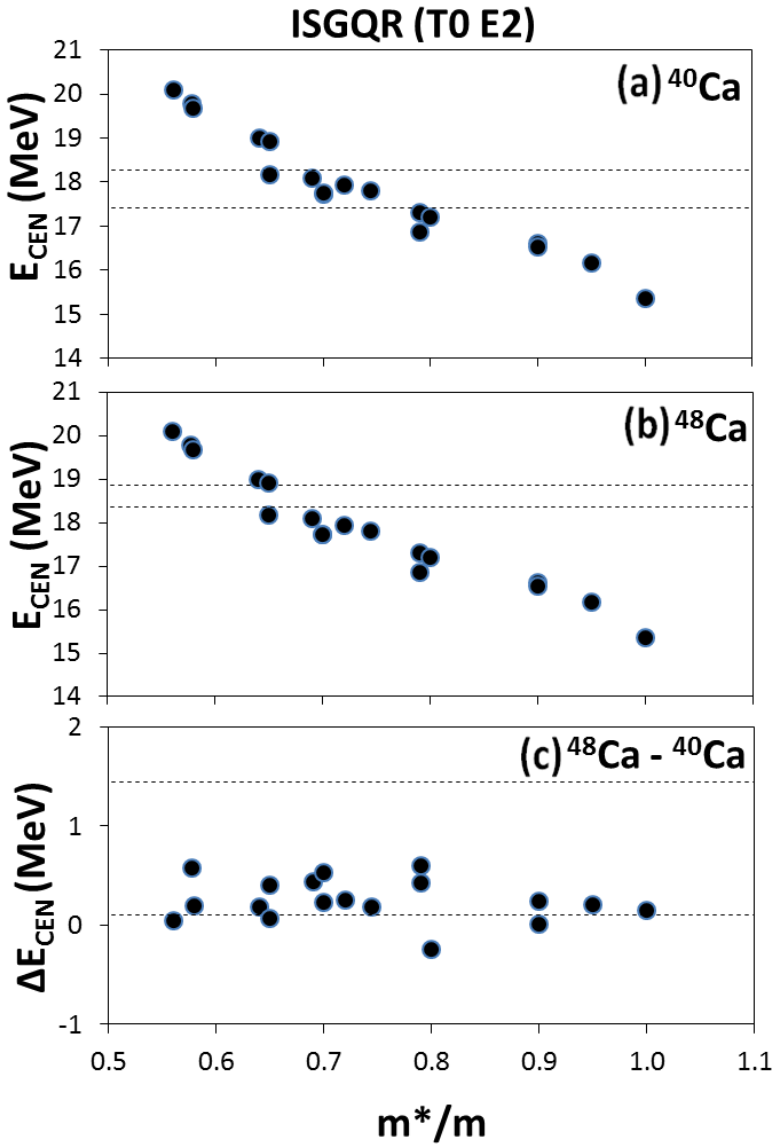

Figure 11 [60] Same as Figure 7 except for the ISGQR as a function of m*/m.

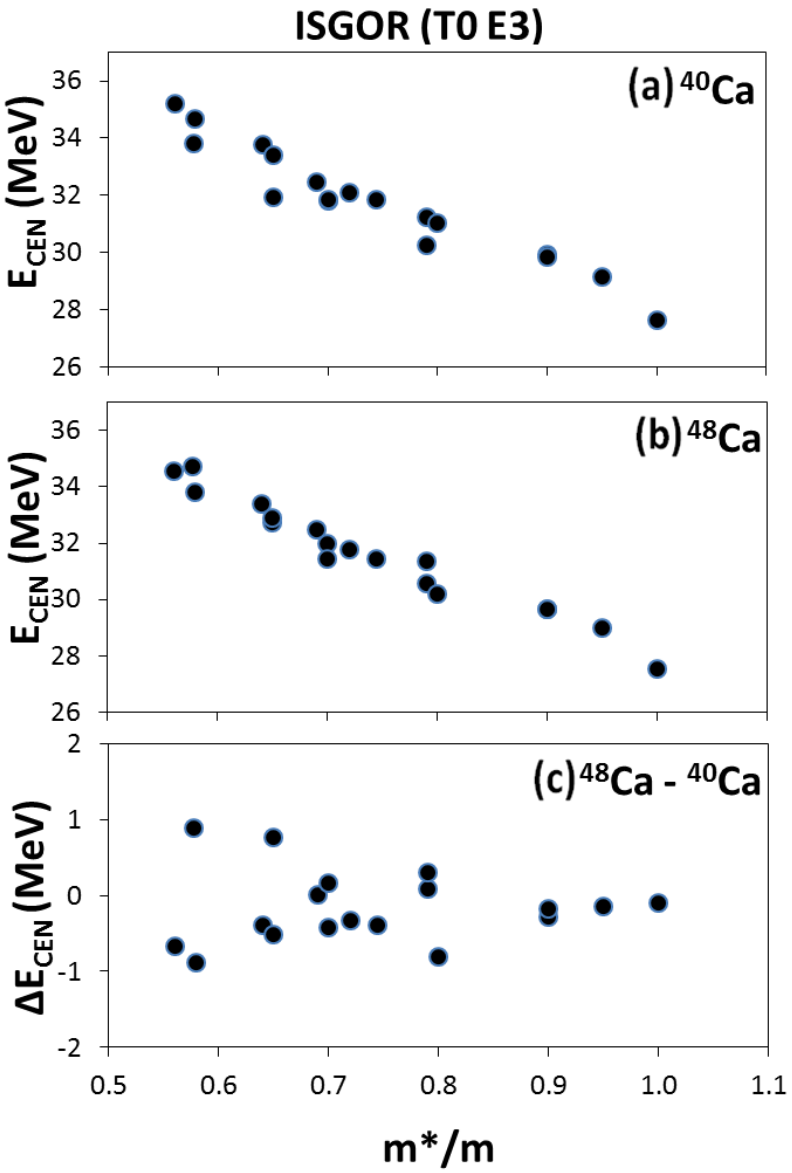

Figure 12 [60] Same as Figure 11 except for the ISGOR.

For completeness we present in Table 4 the centroid energies of the isoscalar (T0) giant resonances of multipolarities $L = 0 - 3$ for each of 18 interactions used and in Table 5 the values of the Pearson correlations coefficients among the various NM properties and spin-orbit strength W_0 with the centroid energies of the isoscalar (T0) giant resonances of multipolarities $L = 0 - 3$. We find no correlations or very weak correlations between the ^{48}Ca – ^{40}Ca centroid energy differences of the isoscalar giant resonances with the coefficients J, L, or K_{sym}, associated with the density dependence of the symmetry energy and a strong correlation with the value of W_0.

Table 4. Isoscalar centroid energies. Isoscalar centroid energies of ^{40}Ca or ^{48}Ca for the 18 Skyrme interactions for multipolarities *L= 0 – 3*.

	^{40}Ca				^{48}Ca			
	L0	L1	L2	L3	L0	L1	L2	L3
SGII	21.27	29.88	17.31	31.26	20.64	30.59	17.73	31.34
KDE0	21.09	29.51	17.93	32.11	20.21	30.60	18.18	31.77
KDE0v1	21.07	29.40	17.80	31.85	20.12	30.51	17.99	31.46
SKM*	20.58	29.34	16.86	30.26	20.09	30.10	17.45	30.56
SK255	22.04	29.83	17.20	31.03	20.86	30.25	16.95	30.22
SkI3	22.43	29.64	19.78	33.82	22.54	30.84	20.36	34.71
SkI4	22.14	30.10	18.91	33.40	21.23	30.90	18.97	32.89
SkI5	22.56	30.21	19.67	34.67	21.76	30.99	19.86	33.79
SV-bas	21.37	29.24	16.54	29.85	20.68	30.28	16.77	29.68
SV-min	20.88	28.90	16.18	29.14	20.16	29.66	16.38	29.00
SV-m56-O	22.58	30.56	20.10	35.21	21.65	30.79	20.15	34.54
SV-m64-O	21.94	30.08	19.00	33.79	21.12	30.99	19.18	33.39
SLy4	21.09	29.51	17.72	31.81	20.46	30.70	18.24	31.97
SLy5	21.09	29.55	17.74	31.86	20.11	30.52	17.96	31.44
SLy6	21.16	29.69	18.09	32.48	20.52	30.45	18.53	32.48
SkMP	21.17	29.84	18.18	31.95	21.03	30.63	18.58	32.71
SkP	19.86	28.60	15.35	27.64	18.94	28.78	15.51	27.54
SkO'	21.05	29.37	16.61	29.95	19.99	29.92	16.62	29.67
Experiment	19.18	23.36	17.84		19.88	27.3	18.61	
+/- error	0.37	0.7	0.43		0.16	0.15	0.24	

Table 5. [60] Isoscalar Pearson correlation coefficients. Pearson correlation coefficients among the various NM properties and spin-orbit strength W_0 with the centroid energies of the isoscalar T0 giant resonances of ^{40}Ca or ^{48}Ca of multipolarities $L = 0 - 3$.

			m*/m	K_{NM}	J	L	K_{sym}	κ	W_0 (X_W=1)
L0 T0	Ca 40	E_{CEN}	-0.75	0.95	0.07	0.56	0.78	0.20	0.00
L0 T0	Ca 48	E_{CEN}	-0.79	0.88	0.02	0.56	0.80	0.24	0.30
L0 T0		ΔE_{CEN}	-0.31	0.07	-0.11	0.16	0.25	0.18	0.73
L1 T0	Ca 40	E_{CEN}	-0.84	0.74	-0.20	0.30	0.64	0.47	0.24
L1 T0	Ca 48	E_{CEN}	-0.89	0.71	-0.11	0.25	0.62	0.25	0.46
L1 T0		ΔE_{CEN}	-0.30	0.14	0.11	-0.02	0.12	-0.28	0.54
L2 T0	Ca 40	E_{CEN}	-0.97	0.81	-0.03	0.40	0.76	0.22	0.48
L2 T0	Ca 48	E_{CEN}	-0.97	0.75	-0.06	0.36	0.74	0.22	0.57
L2 T0		ΔE_{CEN}	-0.20	-0.26	-0.20	-0.18	-0.02	0.00	0.52
L3 T0	Ca 40	E_{CEN}	-0.96	0.80	-0.05	0.35	0.73	0.23	0.41
L3 T0	Ca 48	E_{CEN}	-0.98	0.73	-0.08	0.33	0.72	0.27	0.59
L3 T0		ΔE_{CEN}	-0.11	-0.25	-0.13	-0.07	-0.01	0.16	0.56

IVGMR

For the IVGMR, an isovector compression mode, we show the HF-RPA results (full circles), obtained using the 18 Skyrme interactions from Table 1, for the centroid energies E_{CEN} of ^{40}Ca (a), ^{48}Ca (b) and the ^{48}Ca - ^{40}Ca energy difference (c) as a function of K_{NM} in Figure 13 and as a function of J in Figure 14. The experimental value of E_{CEN} = 31 +/- 2 MeV for ^{40}Ca [10,46] is shown as the region between the dashed lines. We find a medium correlation between E_{CEN} of the IVGMR with K_{NM} and a weak correlation with J, L or $K_{sym.}$ It can be seen from Figure 14 that a stronger correlation between the IVGMR energy and K_{NM} is obtained for a fixed value of J (at 27 and 30 MeV). Figure 15 shows the IVGMR centroid energies as a function of W_0, the

strength of the spin-orbit interaction. A strong positive correlation between the ^{48}Ca - ^{40}Ca energy difference and the value of W_0 is seen. Similar results were obtained for the IVGDR, and the IVGQR.

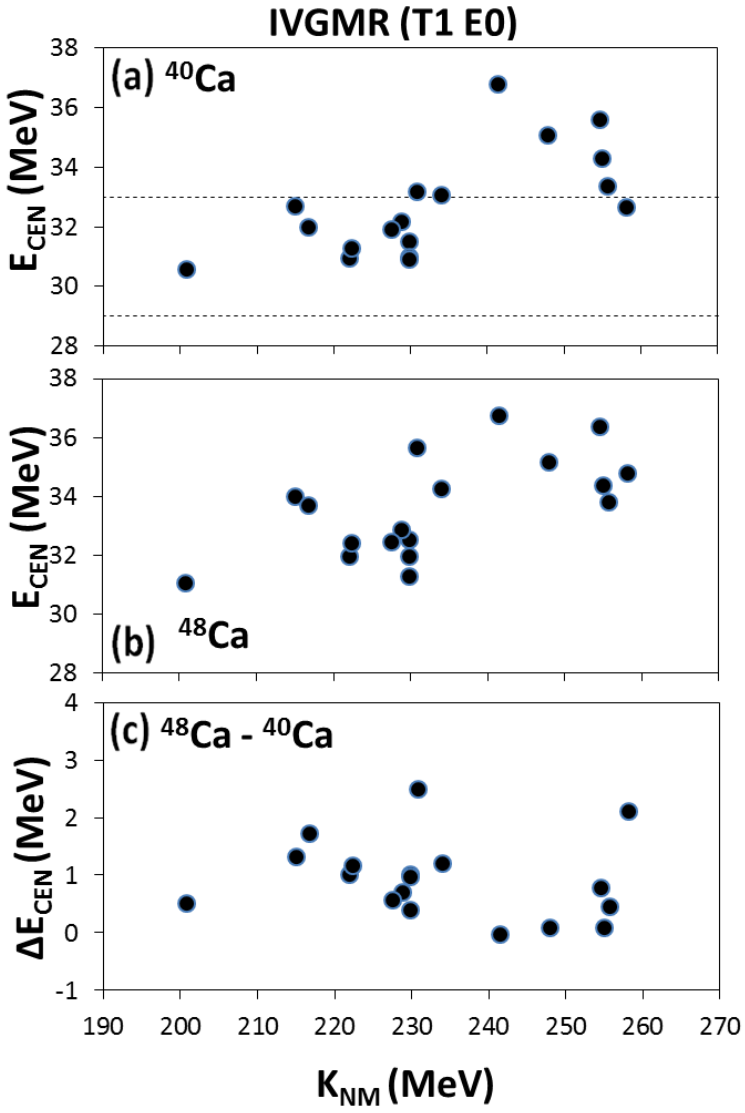

Figure 13 [60] Same as Figure 7 except for the IVGMR as a function of $K_{NM.}$ The experimental data is taken from Ref. [10,61].

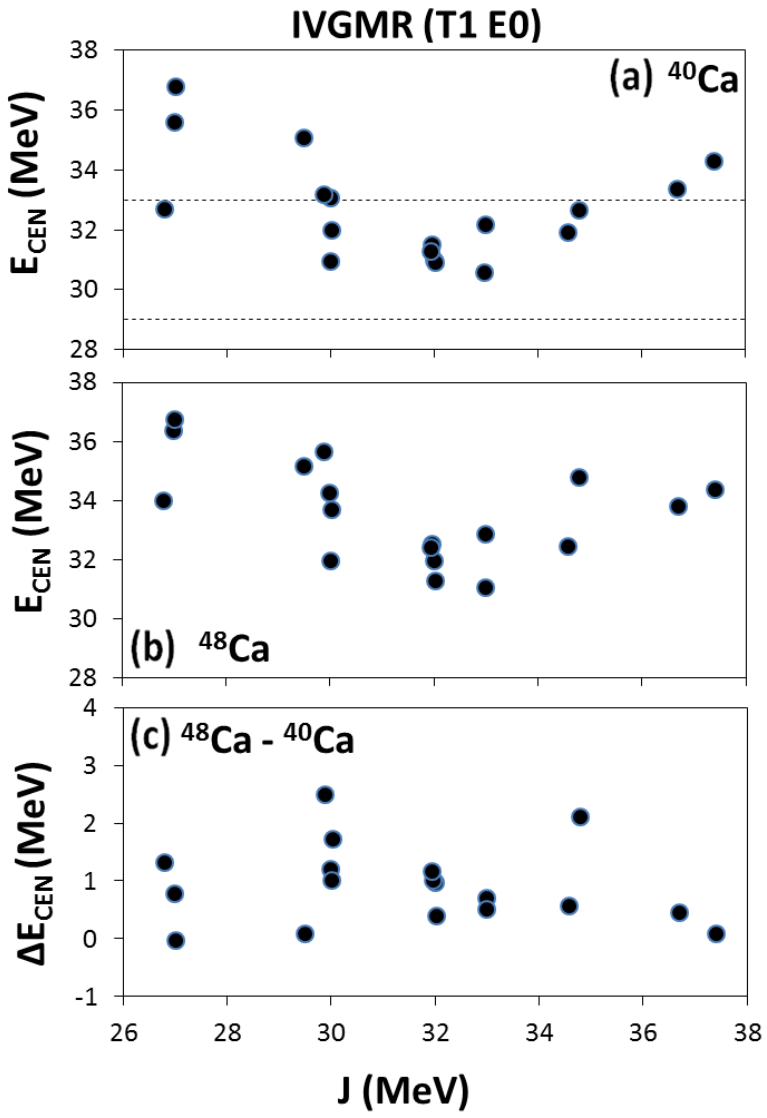

Figure 14 [60] Same as Figure 13 except as a function of J.

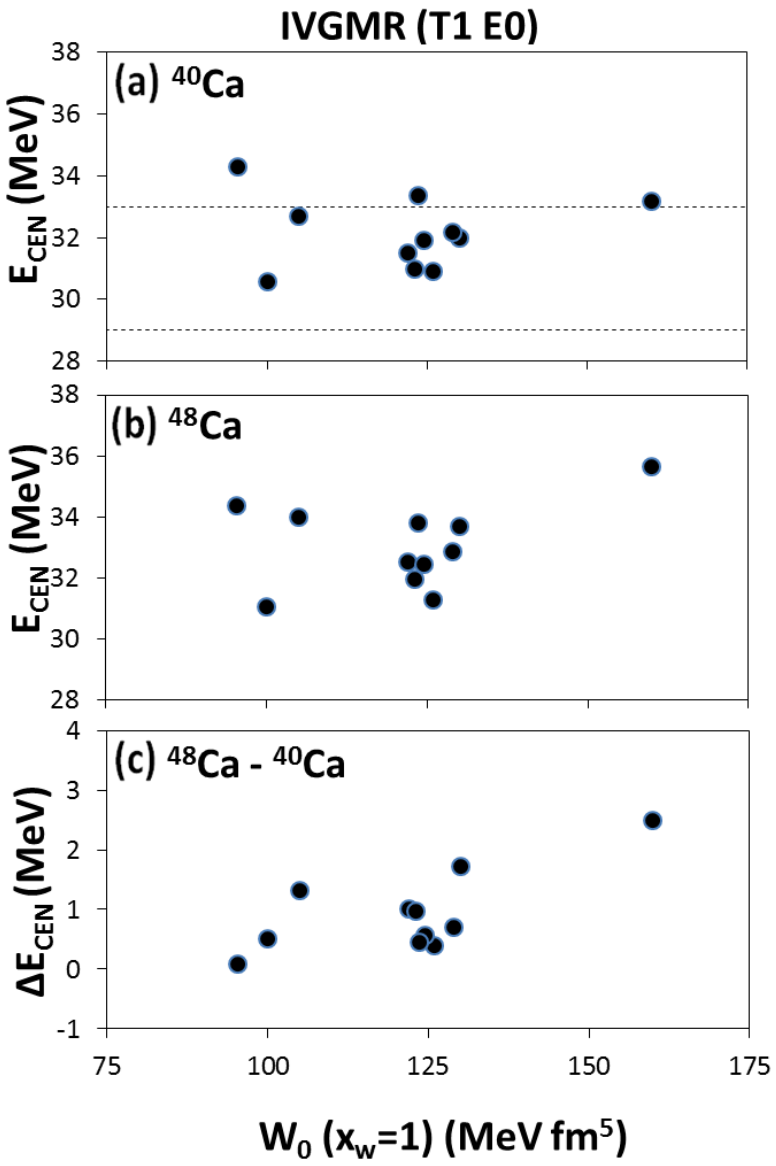

Figure 15 [60] Same as Figure 13 except as a function of W_0.

IVGDR

Figure 16 shows, as a function of J, our HF based RPA results (full circles) of the IVGDR centroid energies E_{CEN} of ^{40}Ca (a), ^{48}Ca (b), and the ^{48}Ca - ^{40}Ca energy difference (c), obtained using the 18 Skyrme type interactions from Table 1. The experimental values of E_{CEN} = 19.8 +/- 0.5 MeV for ^{40}Ca, E_{CEN} = 19.5 +/- 0.5 MeV for ^{48}Ca [62,63,64] and their difference are shown in Figure 16 as the regions between the dashed lines. Weak correlations can be seen between E_{CEN} of ^{40}Ca and E_{CEN} of ^{48}Ca with J. Similar results were obtained for L and K_{sym}.

Figure 17 shows the IVGDR centroid energies as a function of κ, the enhancement factor in the EWSR of the IVGDR. Strong positive correlations between the IVGDR centroid energy of ^{40}Ca and of ^{48}Ca with κ is seen in the Figure.

IVGQR

Figure 18 shows, as a function of m*/m, the HF based RPA results (full circles) of the IVGQR centroid energies E_{CEN} of ^{40}Ca (a), ^{48}Ca (b) and the ^{48}Ca - ^{40}Ca energy difference (c), obtained using the 18 Skyrme type interactions from Table 1. The experimental data of E_{CEN} = 31 +/- 1.5 MeV for ^{40}Ca [65] is shown as the region between the dashed lines. Medium correlations between m*/m and E_{CEN} of ^{40}Ca and E_{CEN} of ^{48}Ca can be seen in Figure 18.

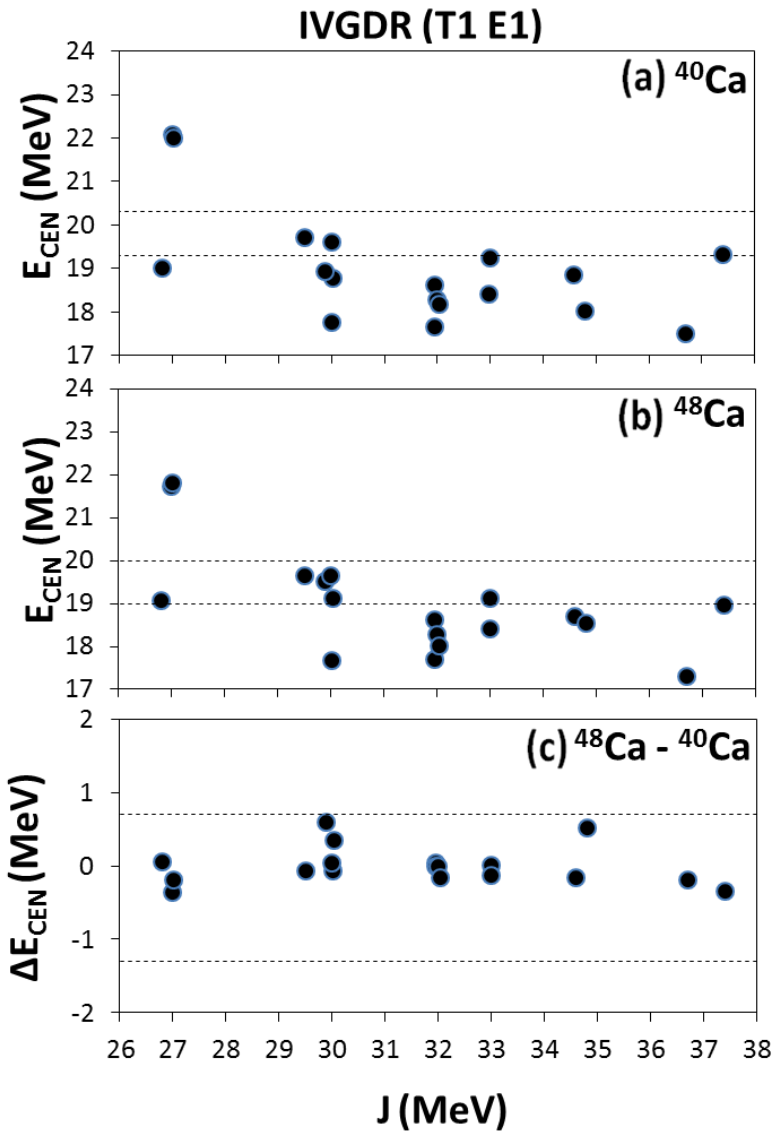

Figure 16 [60] Same as Figure 7 except for the IVGDR. The experimental data is taken from Refs. [62,63,64].

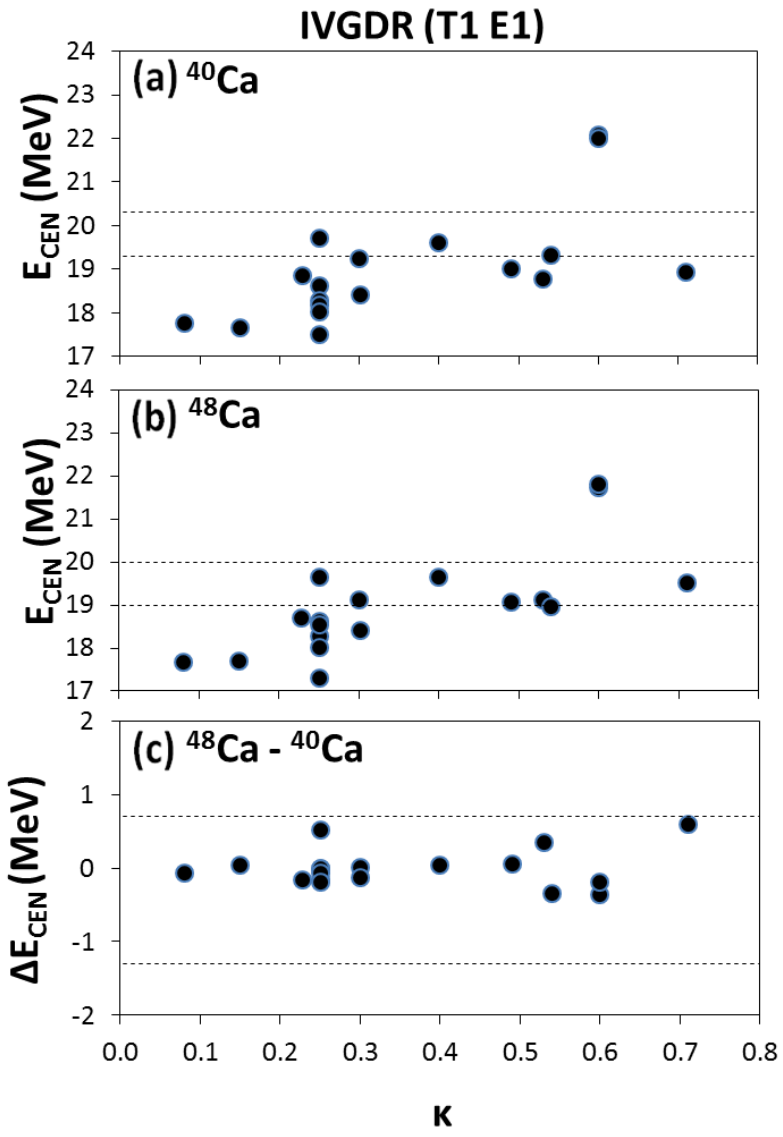

Figure 17 [60] Similar to Figure 16 as a function of κ.

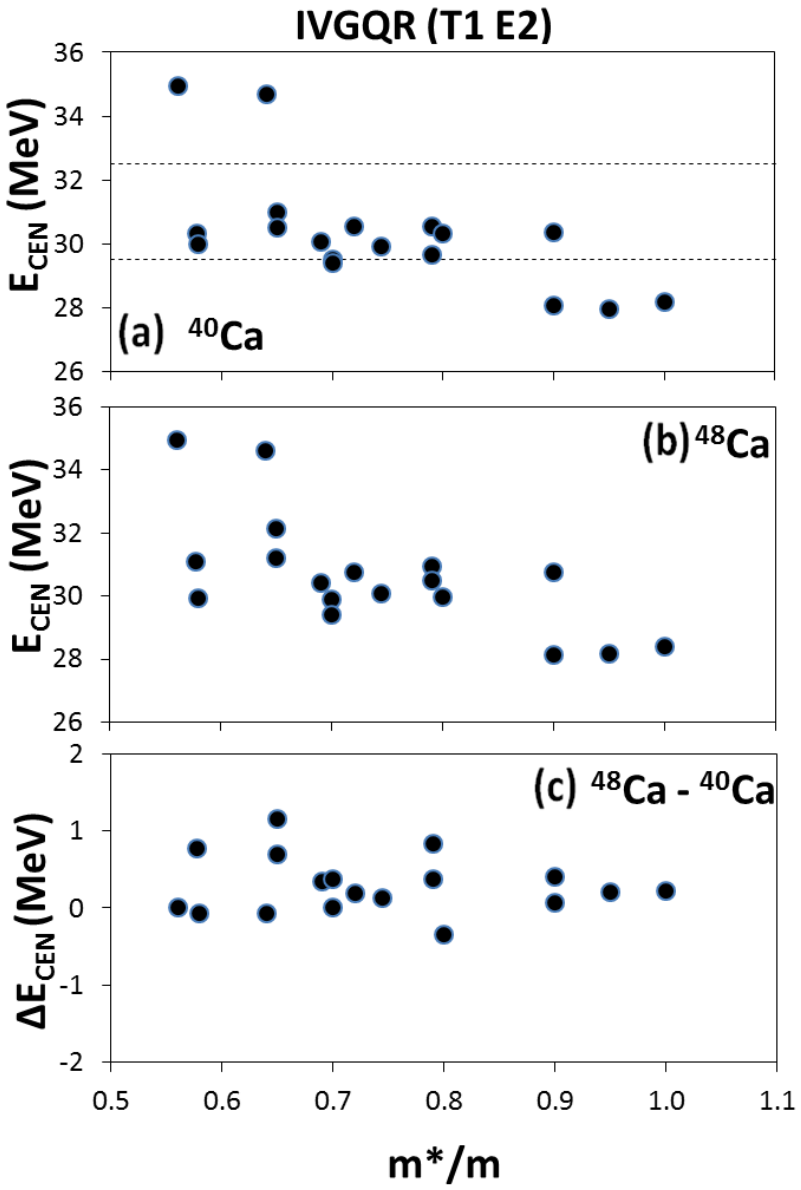

Figure 18 [60] Same as Figure 11 except for the IVGQR. The experimental data is taken from Reference [65].

IVGOR

Figure 19 shows, as a function of m*/m, the HF based RPA results (full circles) of the IVGOR centroid energies E_{CEN} of ^{40}Ca (a), ^{48}Ca (b) and the ^{48}Ca - ^{40}Ca energy difference (c), obtained using the 18 Skyrme type interactions from Table 1. Medium correlations between m*/m and E_{CEN} of ^{40}Ca and E_{CEN} of ^{48}Ca can be seen in Figure 19.

For completeness we present in Table 6 the centroid energies of the isovector (T1) giant resonances of multipolarities $L = 0 - 3$ for each of 18 interactions used and in Table 7 the values of the Pearson correlation coefficients among the various NM properties and spin-orbit strength W_0 with the centroid energies of the isovector (T1) giant resonances of multipolarities $L = 0 - 3$. As shown in Table 7, only weak correlations exist between the E_{CEN} of the isovector giant resonances of ^{40}Ca or ^{48}Ca with J, L and K_{sym}. A strong correlation is found between the ^{48}Ca - ^{40}Ca centroid energy difference of the IVGMRs, IVDGRs, and IVGQRs with W_0. We also note the strong correlation between the E_{CEN} of the IVGDR and the value of κ. Table 8 shows the correlations among the NM properties and the spin-orbit strength W_0 of the 18 Skyrme interactions.

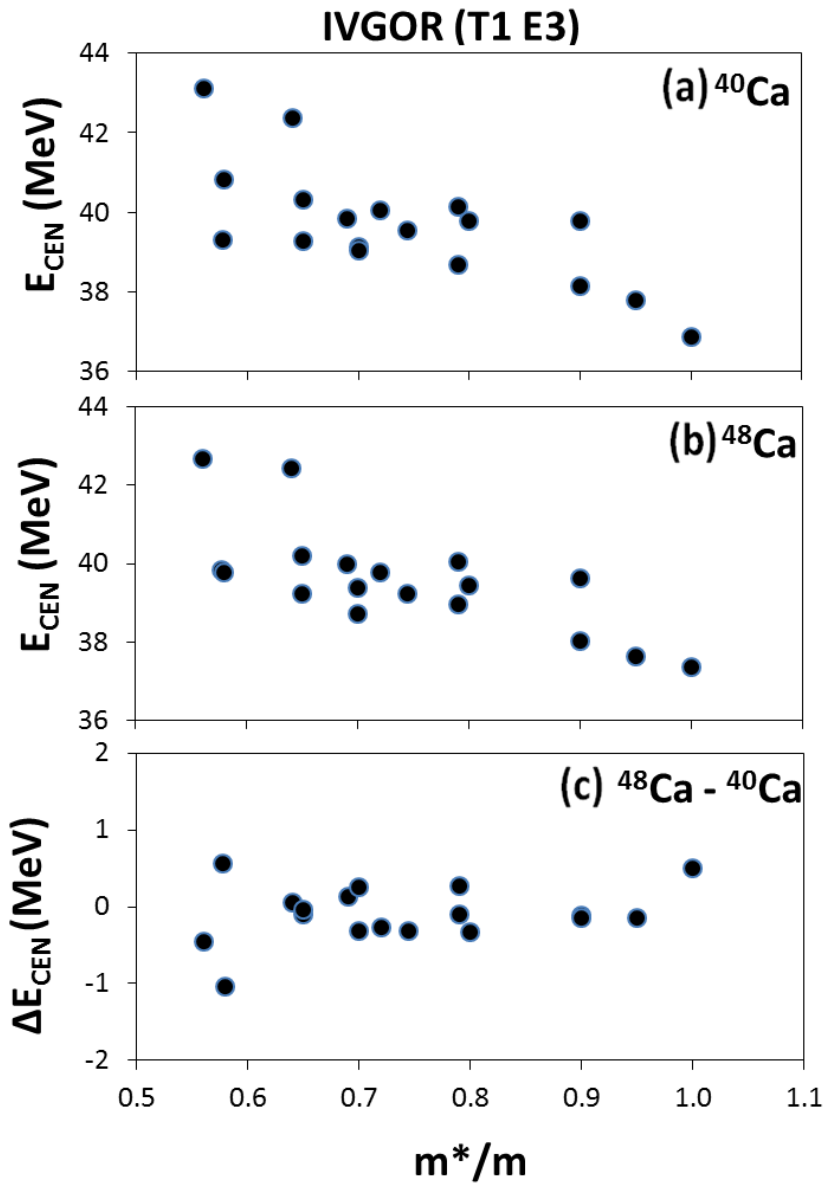

Figure 19 [60] Same as Figure 18 except for the IVGOR.

Table 6. Isovector centroid energies. Isovector centroid energies of ^{40}Ca or ^{48}Ca for the 18 Skyrme interactions for multipolarities $L = 0 - 3$.

	^{40}Ca				^{48}Ca			
	L0	L1	L2	L3	L0	L1	L2	L3
SGII	32.69	19.01	30.55	40.15	34.01	19.06	30.93	40.05
KDE0	32.19	19.25	30.56	40.06	32.88	19.12	30.75	39.79
KDE0v1	31.90	18.87	29.93	39.56	32.47	18.71	30.06	39.25
SKM*	31.99	18.78	29.66	38.69	33.71	19.12	30.49	38.95
SK255	34.29	19.32	30.33	39.77	34.37	18.97	29.98	39.44
SkI3	32.67	18.02	30.34	39.30	34.77	18.53	31.11	39.85
SkI4	35.08	19.70	30.50	39.28	35.17	19.64	31.19	39.24
SkI5	33.37	17.51	29.99	40.83	33.82	17.31	29.92	39.79
SV-bas	33.07	19.61	30.35	39.78	34.27	19.65	30.75	39.63
SV-min	30.94	17.76	27.97	37.79	31.96	17.68	28.17	37.64
SV-m56-O	35.60	22.07	34.95	43.12	36.37	21.72	34.95	42.66
SV-m64-O	36.79	21.99	34.69	42.37	36.75	21.80	34.61	42.43
SLy4	31.00	18.29	29.51	39.12	31.97	18.28	29.88	39.38
SLy5	30.92	18.17	29.39	39.05	31.31	18.01	29.39	38.73
SLy6	31.52	18.62	30.07	39.85	32.53	18.61	30.41	39.98
SkMP	33.16	18.92	30.98	40.31	35.66	19.51	32.13	40.21
SkP	30.56	18.40	28.20	36.87	31.08	18.41	28.41	37.37
SkO'	31.27	17.65	28.07	38.15	32.44	17.70	28.13	38.04
Experiment	31	19.8	31			19.5		
+/- error	2	0.5	1.5			0.5		

Table 7. [60] Isovector Pearson correlation coefficients. Pearson correlation coefficients among the various NM properties and spin-orbit strength W_0 with the centroid energies of the isovector T1 giant resonances of ^{40}Ca or ^{48}Ca of multipolarities $L = 0 - 3$.

			m*/m	K_{NM}	J	L	K_{sym}	κ	$W_0 (X_W=1)$
L0 T1	Ca 40	E_{CEN}	-0.54	0.66	-0.33	0.10	0.31	0.61	0.01
L0 T1	Ca 48	E_{CEN}	-0.64	0.62	-0.35	0.17	0.40	0.74	0.36
L0 T1		ΔE_{CEN}	-0.25	-0.10	-0.06	0.16	0.22	0.31	0.70
L1 T1	Ca 40	E_{CEN}	-0.34	0.31	-0.58	-0.40	-0.17	0.66	-0.07
L1 T1	Ca 48	E_{CEN}	-0.36	0.28	-0.63	-0.40	-0.17	0.73	0.23
L1 T1		ΔE_{CEN}	-0.01	-0.22	-0.09	0.09	0.07	0.14	0.67
L2 T1	Ca 40	E_{CEN}	-0.64	0.52	-0.47	-0.14	0.16	0.68	0.43
L2 T1	Ca 48	E_{CEN}	-0.70	0.49	-0.50	-0.14	0.19	0.73	0.66
L2 T1		ΔE_{CEN}	-0.33	-0.10	-0.18	0.02	0.14	0.27	0.71
L3 T1	Ca 40	E_{CEN}	-0.73	0.61	-0.33	0.04	0.36	0.60	0.37
L3 T1	Ca 48	E_{CEN}	-0.71	0.56	-0.43	-0.07	0.26	0.65	0.42
L3 T1		ΔE_{CEN}	0.34	-0.42	-0.21	-0.41	-0.47	-0.08	-0.11

Table 8. Nuclear matter Pearson correlation coefficients. Pearson correlation coefficients among the various NM properties and spin-orbit strength W_0 among the 18 Skyrme interactions used for the calculation of the ^{40}Ca and ^{48}Ca giant resonances.

	K_{NM}	J	L	K_{sym}	m*/m	κ	$W_0(X_W=1)$
K_{NM}	1.00	0.25	0.62	0.77	-0.73	0.16	0.07
J	0.25	1.00	0.72	0.40	0.01	-0.40	-0.28
L	0.62	0.72	1.00	0.86	-0.35	-0.11	0.00
K_{sym}	0.77	0.40	0.86	1.00	-0.72	-0.05	0.26
m*/m	-0.73	0.01	-0.35	-0.72	1.00	-0.29	-0.62
κ	0.16	-0.40	-0.11	-0.05	-0.29	1.00	0.26
$W_0(X_W=1)$	0.07	-0.28	0.00	0.26	-0.62	0.26	1.00

Conclusions

We have presented results of our fully self-consistent HF-RPA calculations using 18 commonly employed Skyrme type interactions of Table 1, for the centroid energies of isoscalar and isovector giant resonances of multipolarities $L = 0 - 3$ in ^{40}Ca and ^{48}Ca and compared with available experimental data. We have investigated and discussed the sensitivity of the E_{CEN} of the giant resonances to various properties of NM. In particular we point out that:

- For all the 18 Skyrme interactions used in our HF-based RPA calculations (Table 1) the ^{48}Ca – ^{40}Ca centroid energy differences of the ISGMR are smaller than the experimental data. For 17 of the Skyrme interactions used in our HF-based RPA calculations the ^{40}Ca ISGMR lies above that for ^{48}Ca. The 18th interaction (SkI3) predicts the ISGMR in about the same location in both nuclei.
- We have demonstrated the very strong correlations of the E_{CEN} of the compression modes, the ISGMR and the ISGDR, with the NM incompressibility coefficient K_{NM} and noted that the sensitivity of E_{CEN} to the effective mass is a reflection of the

correlation between m*/m and K_{NM}, existing in the Skyrme interactions used in our calculations.

- For all the adopted Skyrme interactions, the calculated centroid energies of the ISGDR in ^{40}Ca and ^{48}Ca are consistently higher than the experimental data (by about 1.5 – 6 MeV).
- We have demonstrated the very strong correlation of E_{CEN} of the ISGQR and the ISGOR with m*/m. We have found that an agreement with the experimental data for E_{CEN} of the ISGQR in ^{40}Ca and ^{48}Ca is obtained for a value of the effective mass in the range of m*/m = 0.65 – 0.8. Using this result we can predict that the values of the E_{CEN} of the ISGOR in ^{40}Ca and ^{48}Ca should be in the region of 30 – 34 MeV.
- We find no correlations or very weak correlations between the ^{48}Ca – ^{40}Ca centroid energy differences of the isoscalar giant resonances of multipolarities L = 0 -3 with the coefficients J, L, or K_{sym}, associated with the density dependence of the symmetry energy. Similar results were found for the isovector giant resonances of multipolarities L = 0 – 3.
- We find positive strong correlations between the ^{48}Ca – ^{40}Ca centroid energy differences (ΔE_{CEN}) of the isoscalar and isovector giant resonances with W_0.
- For the IVGMR, the isovector compression mode, we find a medium correlation with K_{NM} and a weak correlation with J, L or $K_{sym.}$
- We find a weak correlation between the energies of the IVGDR of ^{40}Ca (and ^{48}Ca) and the quantities associated with the density dependence of the symmetry energy.

- We find a strong correlation between the energies of the IVGDR of ^{40}Ca (and ^{48}Ca) and the value of κ.
- For the IVGQR and IVGOR we find a strong correlation between E_{CEN} and m*/m.

The disagreement between the HF-RPA results and the experimental data for the centroid energies of the ISGMR and ISGDR in ^{40}Ca and ^{48}Ca remain unsolved problems which call for possible extensions of the EDF used in this work, microscopic calculations of the excitation cross sections of giant resonances [58,66] and/or going beyond the HF-RPA theory [67].

CHAPTER IV

GIANT RESONANCES IN ^{208}PB[*]

We now present results of our fully self-consistent HF based RPA calculations of the strength functions and centroid energies of isoscalar and isovector giant resonances of multipolarities L = 0 - 3 in ^{208}Pb [68], obtained for 34 widely used Skyrme type interactions shown in Table 1: SGII [23], KDE0 [24], KDE0v1 [24], SKM* [25], SK255 [26], SkI3 [41], SkI4 [41], SkI5 [41], SV-bas [42], SV-min [42], SV-m56-O [43], SV-m64-O [43], SLy4 [36], SLy5 [36], SLy6 [36], SkMP [44], SkP [45], SkO' [46], SV-sym32 [42], SkO [46], LNS [47], MSL0 [48], NRAPR [49] SQMC650 [50], SQMC700 [50], SkT1 [51], SkT2 [51], SkT3 [51], SkT8 [51], SkT9 [51], SkT1* [51], SkT3* [51], Skxs20 [52], and Z_σ [53]. These interactions are associated with the ranges of NM properties (see Table 3): E/A = 15.32 – 16.33 MeV, ρ_0 = 0.156 - 0.175 fm^{-3}, K_{NM} = 201 – 258 MeV, J = 26.8 – 37.4 MeV, L = -29.4 – 129.3 MeV, K_{sym} = -401 – 160 MeV, m*/m = 0.56 – 1.00 and κ = 0.00 – 0.71.

In Figures 20 and 21 we display the HF-based RPA results (solid lines) for the distribution of the energy-weighted strength normalized to one (ES(E)/EWSR) for the isoscalar and isovector giant resonances of multipolarities L = 0-3 in ^{208}Pb, obtained using the KDE0 [24] interaction that is representative of the strength distributions for the rest of the interactions. For the purpose of comparison with experiment a Lorenzian

[*] Part of this chapter is reprinted with permission from "Giant Resonances in ^{40}Ca and ^{48}Ca" by M. R. Anders *et. al.*, 2013. *Physical Review C*, **87**, 024303, Copyright [2013] by American Physical Society.

smearing of a 3 MeV width was used in the calculation. The experimental data [69] are shown as histograms.

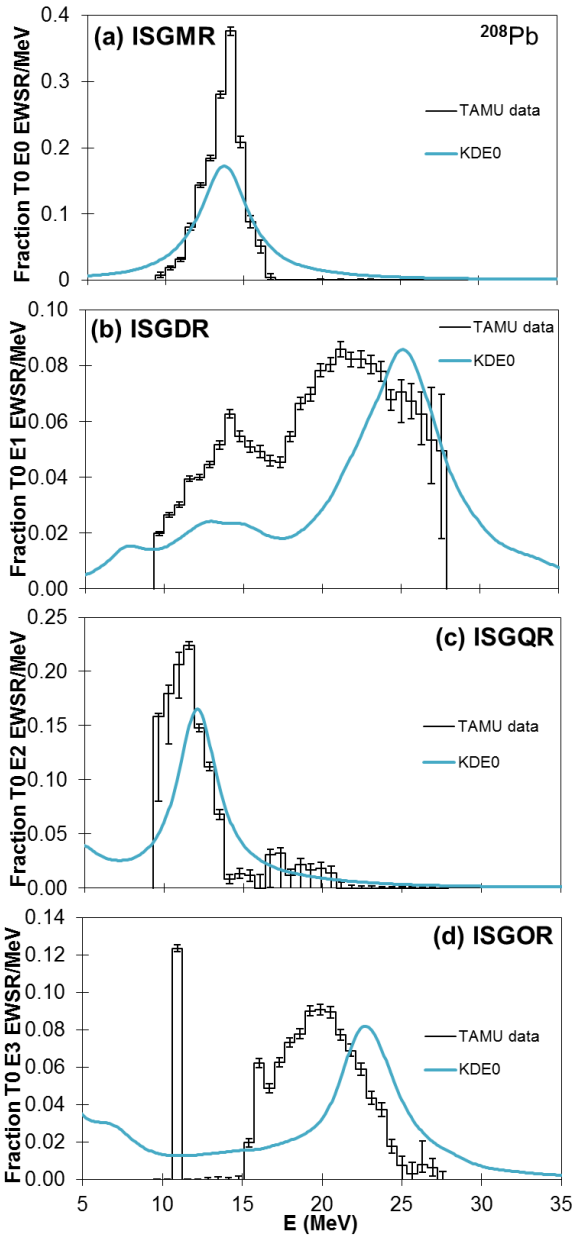

Figure 20 Self-consistent HF-based RPA results (solid lines) for the distribution of the energy-weighted strength normalized to one (fraction of EWSR) for the isoscalar monopole (E0), dipole (E1), quadrupole (E2), and octopole (E3) in ^{208}Pb, obtained using the KDE0 [24] Skyrme interaction. A Lorenzian smearing of a 3 MeV width was used in the calculation. The experimental data [69] are shown as histograms.

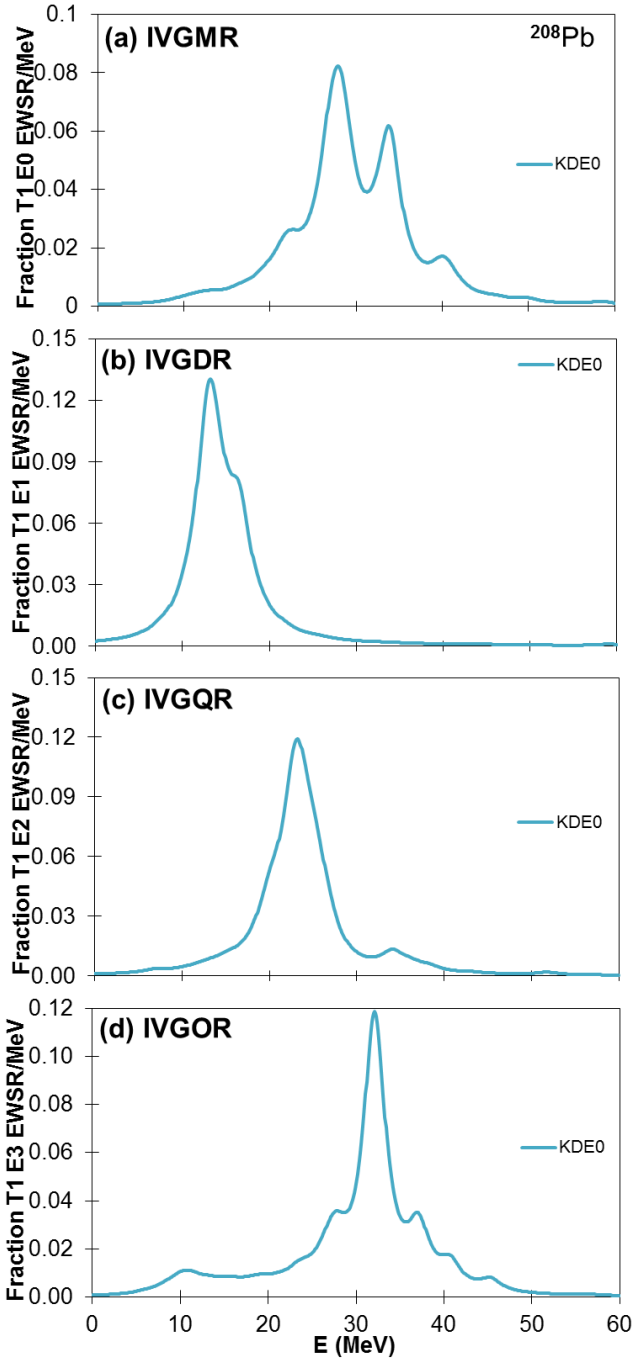

Figure 21 Self-consistent HF-based RPA results (solid lines) for the distribution of the energy-weighted strength, normalized to one (fraction of EWSR), for the isovector monopole (E0), dipole (E1), quadrupole (E2), and octopole (E3) in ^{208}Pb, obtained using the KDE0 [24] Skyrme interaction. A Lorenzian smearing of a 3 MeV width was used in the calculation.

To investigate the sensitivity of the energies of the giant resonances in ^{208}Pb to NM properties (Table 3) we calculated the Pearson correlation coefficients (a measure of linear correlation) between the centroid energies E_{CEN}, Eq. (2.53), and the properties of NM. We used a small smearing width (0.05 MeV) to insure accuracy for E_{CEN}. For a proper comparison with experiment, we used the experimental excitation energy ranges in determining the centroid energies. We use the excitation energy range of 5 – 30 MeV [69] for the ISGMR, the range of 16 – 40 MeV [69] for the ISGDR, and the range of 8 – 16 MeV [69] for the ISGQR. For the ISGOR we use the appropriate excitation energy range of 15 – 28 MeV [69]. We use the excitation energy range of 10 – 45 MeV for the IVGMR [10], the range of 5 – 30 MeV for the IVGDR [70], the range of 10 – 40 MeV for the IVGQR [71-75] and the range of 20 – 50 MeV for the IVGOR (see also Figures 20 and 21).

In Figures 22-26, we compare the experimental data [69] of the ISGMR (a), ISGDR (b), ISGQR (c), and ISGOR (d) centroid energies of ^{208}Pb with the results of fully self-consistent HF-based RPA calculations (full circles), obtained using the 34 Skyrme interactions of Table 1. The calculated values are plotted as a function of K_{NM}, J, L, $K_{sym,}$ and m*/m. Table 9 shows the correlations among the NM properties and the spin-orbit strength W_0 of the 34 Skyrme interactions of Table 1.

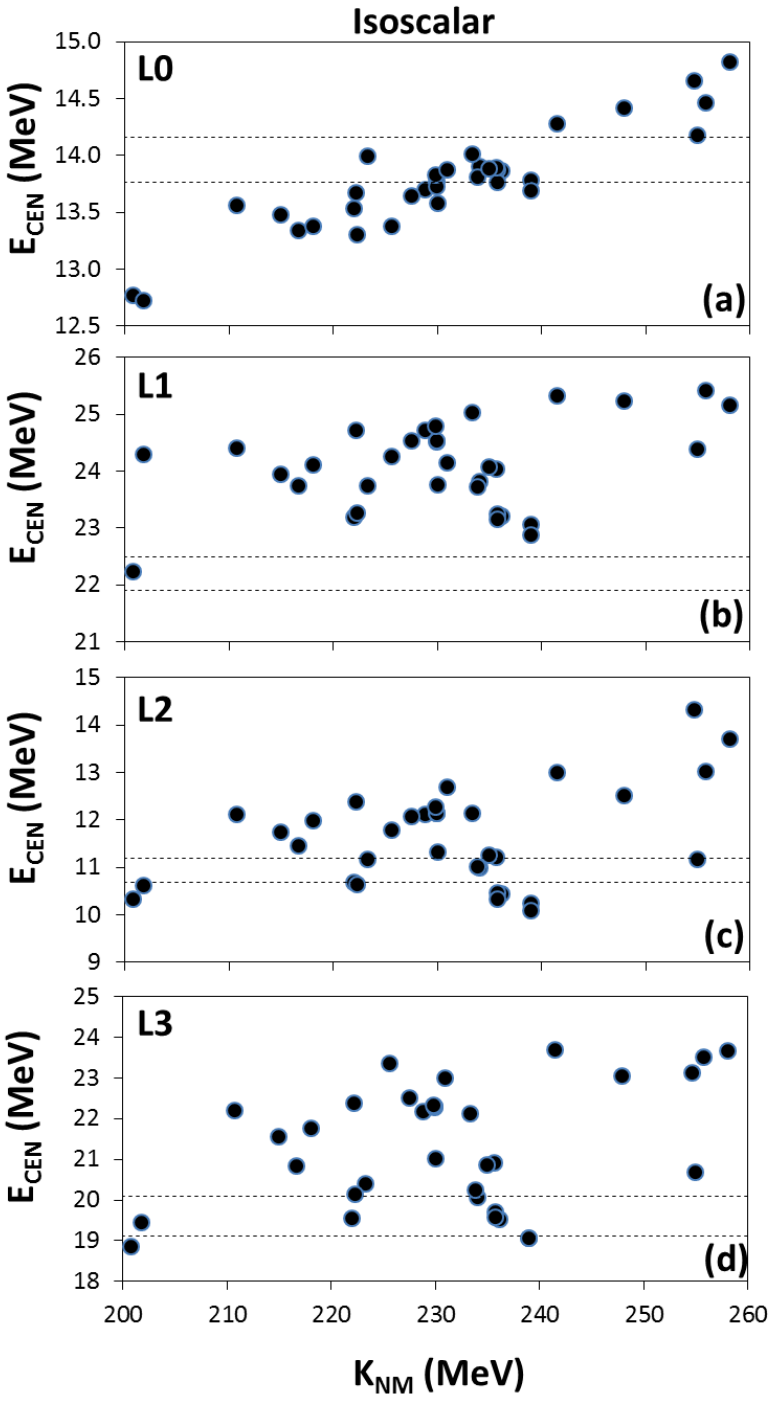

Figure 22 Comparison of experimental data [69] of the ISGMR (a), ISGDR (b), ISGQR (c), and ISGOR (d) centroid energies of ^{208}Pb, shown as the regions between the dashed lines, with the results of fully self-consistent HF based RPA calculations (full circles) obtained using the Skyrme interactions of Table 1, plotted vs. K_{NM}.

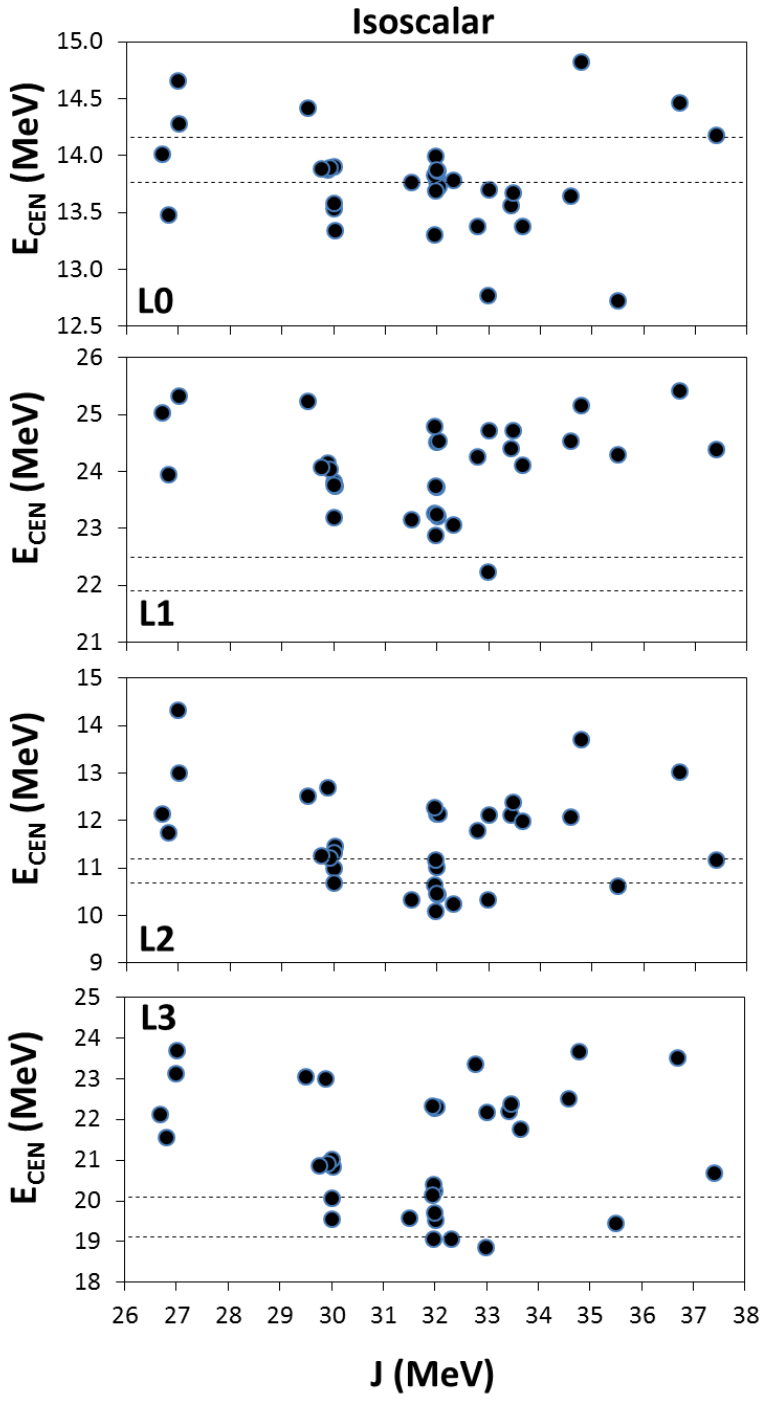

Figure 23 Same as Figure 22 except as a function of J.

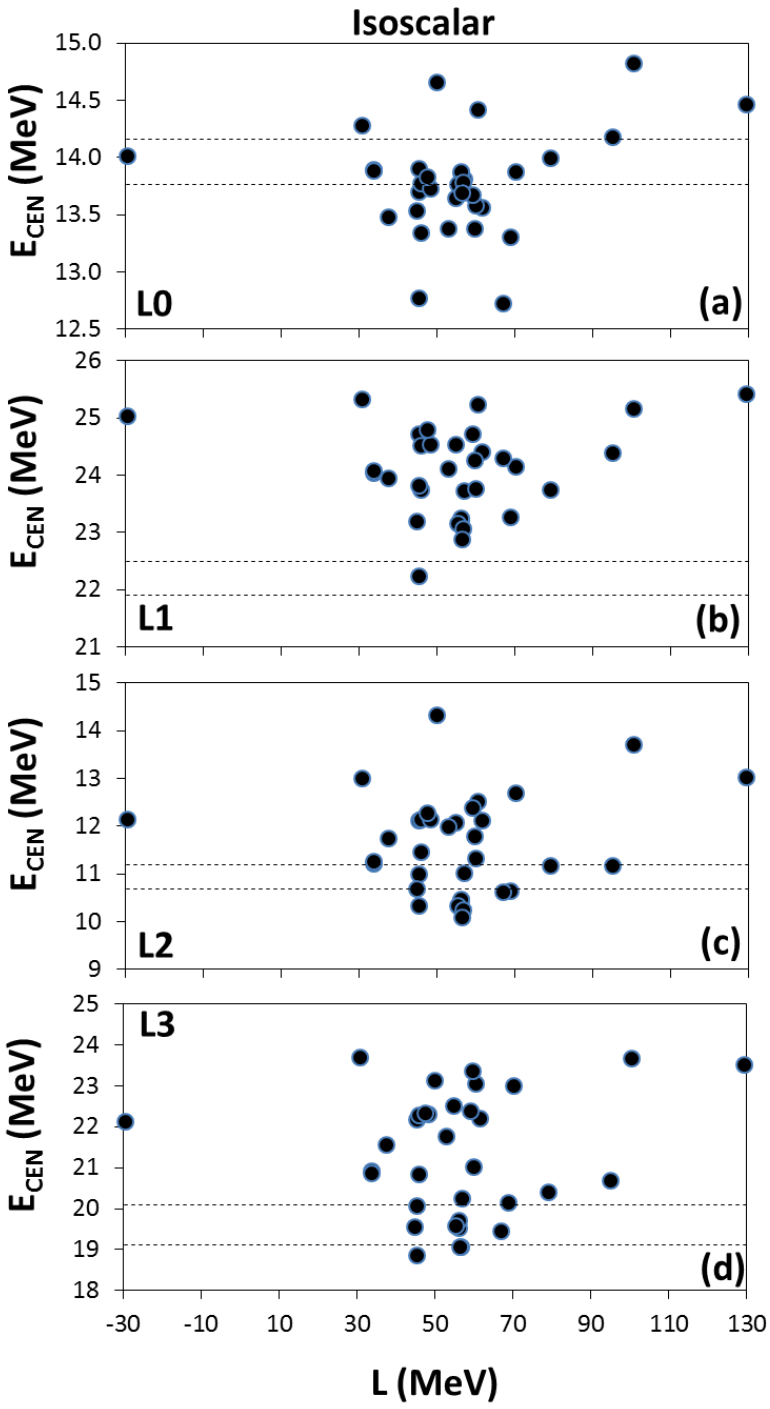

Figure 24 Same as Figure 22 except as a function of L.

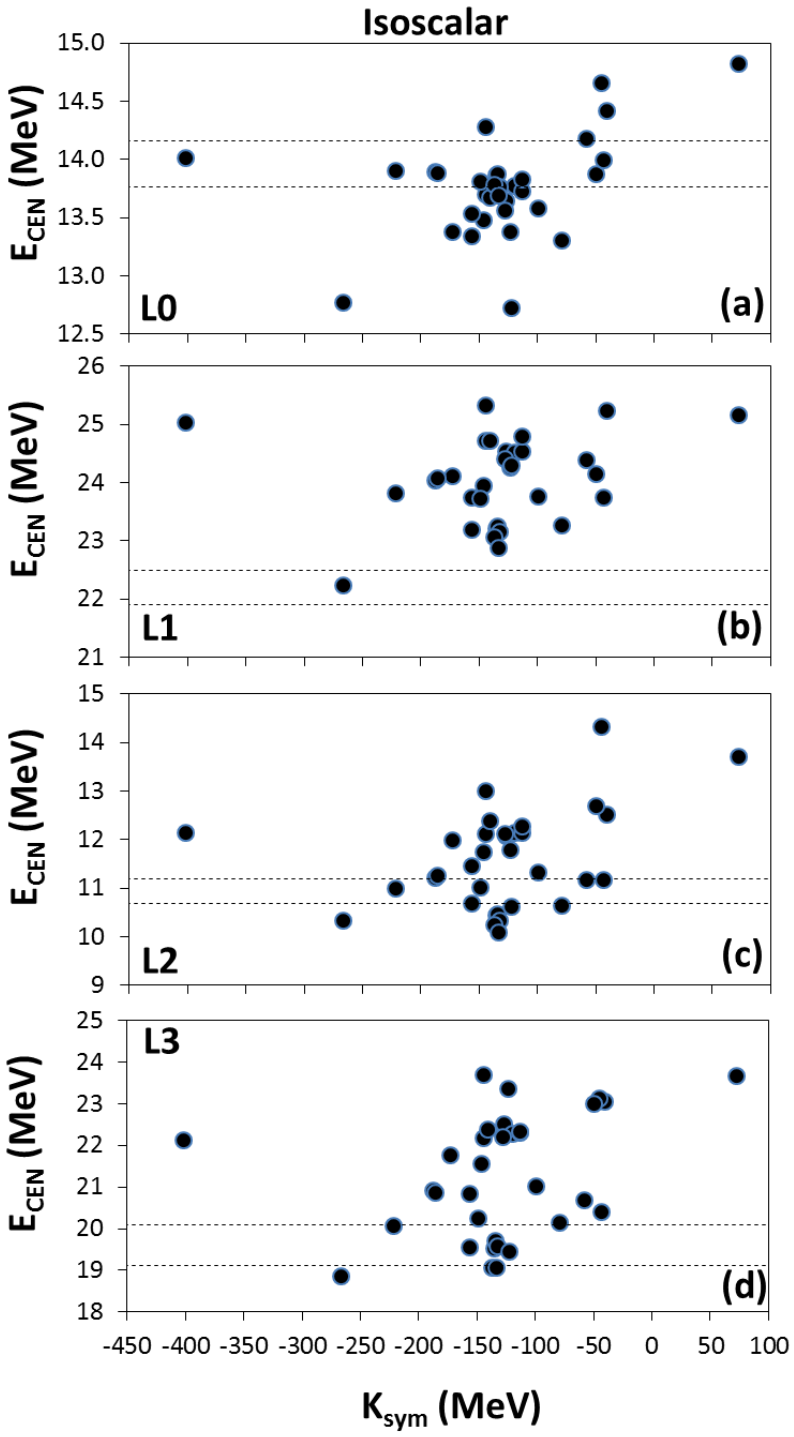

Figure 25 Same as Figure 22 except as a function of K_{sym}.

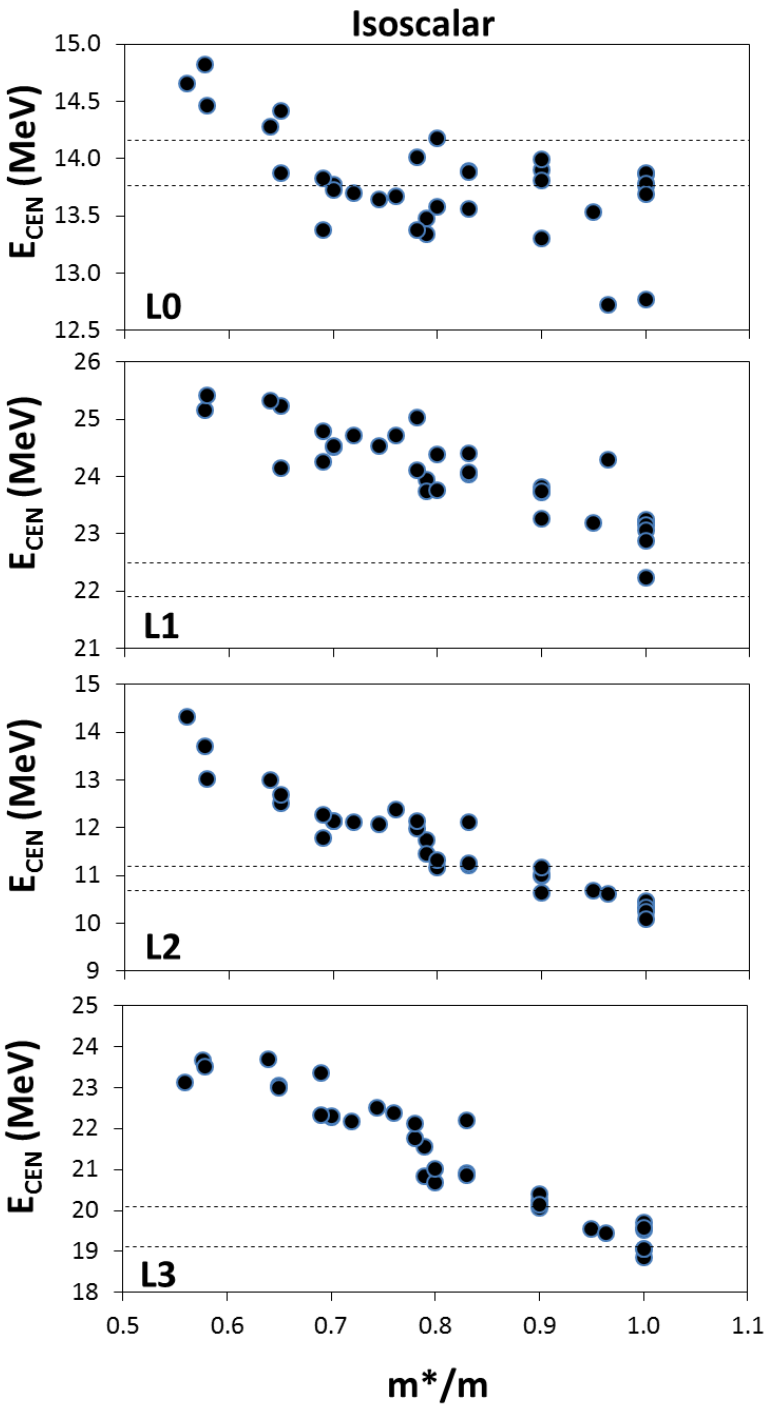

Figure 26 Same as Figure 22 except as a function of m*/m.

Table 9. Nuclear matter Pearson correlation coefficients. Pearson correlation coefficients among the various NM properties and spin-orbit strength W_0 among the 34 Skyrme interactions used for the calculation of the ^{208}Pb giant resonances.

	K_{NM}	J	L	K_{sym}	m*/m	κ	$W_0(x_w=1)$
K_{NM}	1.00	0.00	0.30	0.49	-0.43	-0.01	0.10
J	0.00	1.00	0.71	0.44	0.09	-0.24	-0.26
L	0.30	0.71	1.00	0.90	-0.17	-0.12	-0.07
K_{sym}	0.49	0.44	0.90	1.00	-0.45	-0.07	0.09
m*/m	-0.43	0.09	-0.17	-0.45	1.00	-0.61	-0.22
κ	-0.01	-0.24	-0.12	-0.07	-0.61	1.00	-0.03
$W_0(x_w=1)$	0.10	-0.26	-0.07	0.09	-0.22	-0.03	1.00

ISGMR

In Figures 22a, 23a, 24a, 25a, and 26a we compare the experimental data [69] of the ISGMR centroid energies of ^{208}Pb with the results of fully self-consistent HF-based RPA calculations (full circles), obtained using the 34 Skyrme interactions of Table 1 plotted as a function of K_{NM}, J, L, K_{sym}, and m*/m, respectively. The experimental values of E_{CEN} = 13.96 +/- 0.20 MeV [69] are plotted as the regions between the dashed lines. A very strong correlation between E_{CEN} of ^{208}Pb can be seen with K_{NM} and is consistent with value of K_{NM} = 220 – 240 MeV. This is expected, since the ISGMR centroid energy is very sensitive to the value of K_{NM} [1,3,8]. We also found a medium correlation between the ISGMR energies and the effective mass m*/m and K_{sym}, which is a reflection of the medium correlation between K_{NM} and m*/m seen in Table 9 (see also Ref. [8]). No correlations were found between the ISGMR energies and J or L.

ISGDR

In Figures 22b, 23b, 24b, 25b, and 26b we compare the experimental data [69] of the ISGDR centroid energies of ^{208}Pb with the results of fully self-consistent HF-based

RPA calculations (full circles), obtained using the 34 Skyrme interactions of Table 1 plotted as a function of K_{NM}, J, L, K_{sym}, and m*/m, respectively. The experimental values of E_{CEN} = 22.20 +/- 0.30 MeV [69] are plotted as the regions between the dashed lines. For all the Skyrme interactions of Table 1, the calculated ISGDR centroid energies are higher than the experimental values by 0.5 – 3 MeV except one interaction, SkP. We note that the experimental results for the fraction of the EWSR for the ISGDR in ^{208}Pb is 114 + 12 - 25 % [69] compared to the calculated values of 100%. A strong correlation is also found between the ISGDR energy of ^{208}Pb with m*/m and a medium correlation with K_{NM} reflecting the medium correlation between m*/m and K_{NM} shown in Table 9. No correlations were found with the symmetry energy parameters, J, L, or K_{sym}.

ISGQR

In Figures 22c, 23c, 24c, 25c, and 26c we compare the experimental data [69] of the ISGQR centroid energies of ^{208}Pb with the results of fully self-consistent HF-based RPA calculations (full circles), obtained using the 34 Skyrme interactions of Table 1 plotted as a function of K_{NM}, J, L, K_{sym}, and m*/m, respectively. The experimental values of E_{CEN} = 10.89 +/- 0.30 MeV [69] are plotted as the regions between the dashed lines. As seen in Figure 26c, a very strong correlation exists between the ISGQR energy of ^{208}Pb with m*/m. We find that interactions having m*/m = 0.9 – 1.0 reproduce the experimental data of the ISGQR.

ISGOR

In Figures 22d, 23d, 24d, 25d, and 26d we compare the experimental data [69] of the ISGOR centroid energies of ^{208}Pb with the results of fully self-consistent HF-based

RPA calculations (full circles), obtained using the 34 Skyrme interactions of Table 1 plotted as a function of K_{NM}, J, L, K_{sym}, and m*/m, respectively. The experimental values of E_{CEN} = 19.6 +/- 0.5 MeV [69] are plotted as the regions between the dashed lines. As seen in Figure 26d, a very strong correlation exists between the ISGOR energy of ^{208}Pb with m*/m. We find that interactions having m*/m = 0.9 – 1.0 reproduce the experimental data of the ISGOR.

For completeness we present in Table 10 the centroid energies of the isoscalar (T0) giant resonances of multipolarities L= 0 – 3 for each of 34 interactions used and in Table 11 the values of the Pearson correlations coefficients among the various NM properties and spin-orbit strength W_0 with the centroid energies of the isoscalar (T0) giant resonances of multipolarities L= 0 – 3. The isoscalar giant resonances for ^{208}Pb are consistent with K_{NM} ~ 230 MeV, J ~ 32 MeV, L ~ 45 MeV, K_{sym} ~ -140 MeV, and m*/m ~ 1.0.

Table 10. Isoscalar centroid energies. Isoscalar centroid energies of ^{208}Pb for the 34 Skyrme interactions for multipolarities $L = 0 - 3$.

	L0	L1	L2	L3
SGII	13.48	23.95	11.74	21.57
KDE0	13.70	24.72	12.12	22.19
KDE0v1	13.64	24.54	12.08	22.50
SKM*	13.34	23.74	11.47	20.85
SK255	14.18	24.38	11.17	20.68
SkI3	14.82	25.16	13.70	23.66
SkI4	14.42	25.23	12.52	23.06
SkI5	14.46	25.42	13.03	23.53
SV-bas	13.90	23.82	10.98	20.06
SV-min	13.53	23.19	10.68	19.56
SV-sym32	13.81	23.72	11.00	20.25
SV-m56-O	14.66	26.13	14.31	23.13
SV-m64-O	14.28	25.33	13.00	23.70
SLy4	13.77	24.52	12.14	22.27
SLy5	13.73	24.54	12.14	22.29
SLy6	13.83	24.80	12.26	22.33
SkMP	13.87	24.15	12.69	23.01
SkP	12.77	22.23	10.33	18.87
SkO	13.99	23.75	11.16	20.39
SkO'	13.31	23.26	10.65	20.14
LNS	13.57	24.41	12.11	22.20
MSL0	13.58	23.76	11.32	21.02
NRAPR	13.37	24.27	11.78	23.36
SQMC650	13.37	24.11	11.99	21.75
SQMC700	13.67	24.72	12.37	22.38
SkT1	13.86	23.21	10.43	19.52
SkT2	13.87	23.25	10.47	19.71
SkT3	13.77	23.16	10.32	19.59
SkT8	13.89	24.05	11.20	20.91
SkT9	13.88	24.08	11.26	20.87
SkT1*	13.79	23.07	10.25	19.05
SkT3*	13.69	22.89	10.08	19.07
Skxs20	12.73	24.29	10.61	19.46
Z_σ	14.01	25.03	12.13	22.12
Experiment	13.96	22.20	10.89	19.60
Error	0.20	0.30	0.30	0.50

Table 11. Isoscalar Pearson correlation coefficients. Pearson correlation coefficients among the various NM properties and spin-orbit strength W_0 with the centroid energies of the isoscalar T0 giant resonances of ^{208}Pb for multipolarities *L= 0 – 3*.

	L0	L1	L2	L3
K	0.91	0.46	0.41	0.35
J	-0.14	-0.08	-0.14	-0.08
L	0.23	0.07	0.12	0.11
K_{sym}	0.48	0.35	0.41	0.38
m*/m	-0.56	-0.88	-0.95	-0.96
κ	0.10	0.48	0.59	0.60
$W_0(x_w=1)$	0.29	0.20	0.31	0.12

In Figures 27-32, we compare the experimental data [69] of the IVGMR (a), IVGDR (b), and IVGQR (c) centroid energies of ^{208}Pb with the results of fully self-consistent HF-based RPA calculations (full circles), obtained using the 34 Skyrme interactions of Table 1. The results of ISGOR are also plotted in part (d) of these figures. The calculated values are plotted as a function of K_{NM}, J, L, K_{sym}, m*/m, and κ.

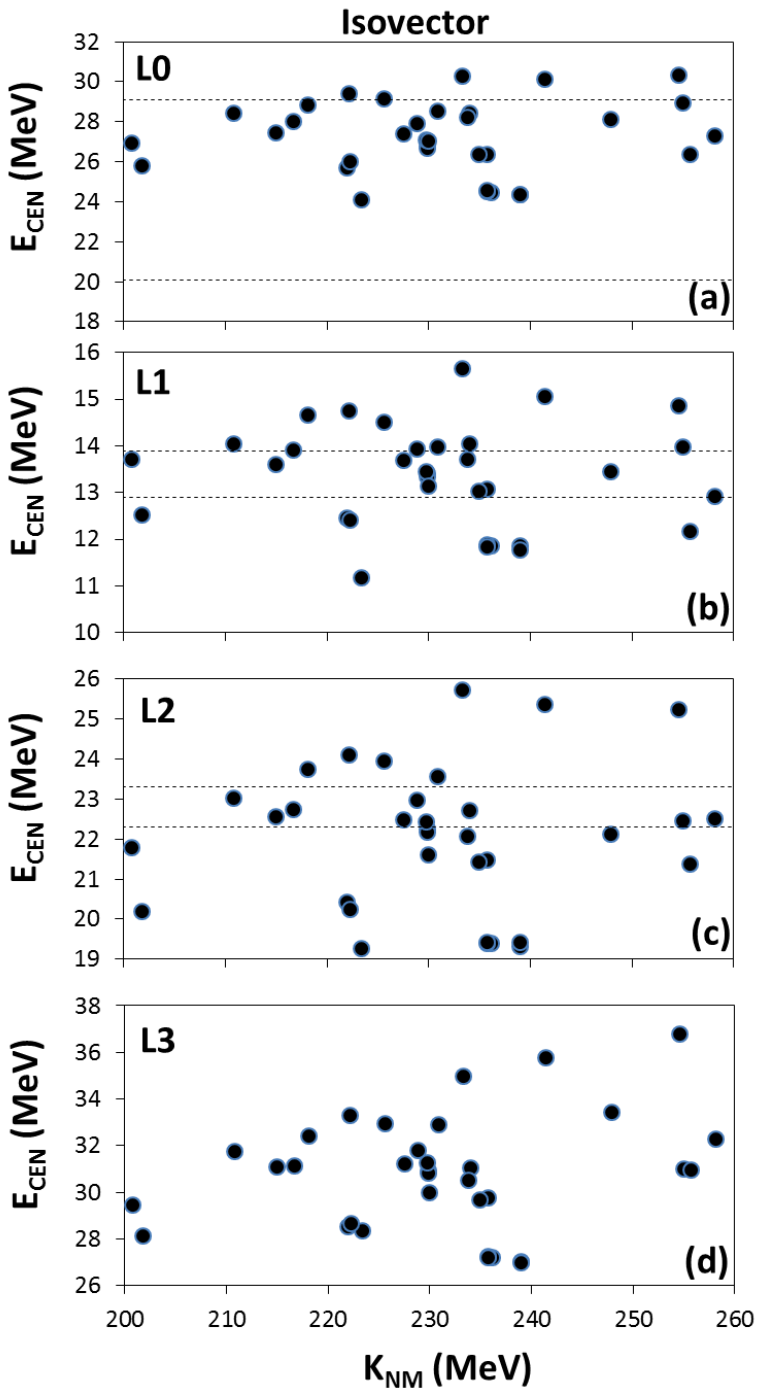

Figure 27 Comparison of experimental data [69] of the IVGMR (a), IVGDR (b), and IVGQR (c) centroid energies of ^{208}Pb, shown as the regions between the dashed lines, with the results of fully self-consistent HF based RPA calculations (full circles) obtained using the Skyrme interactions of Table 1, plotted vs. K_{NM}. Calculated IVGOR (d) centroid energies are also shown.

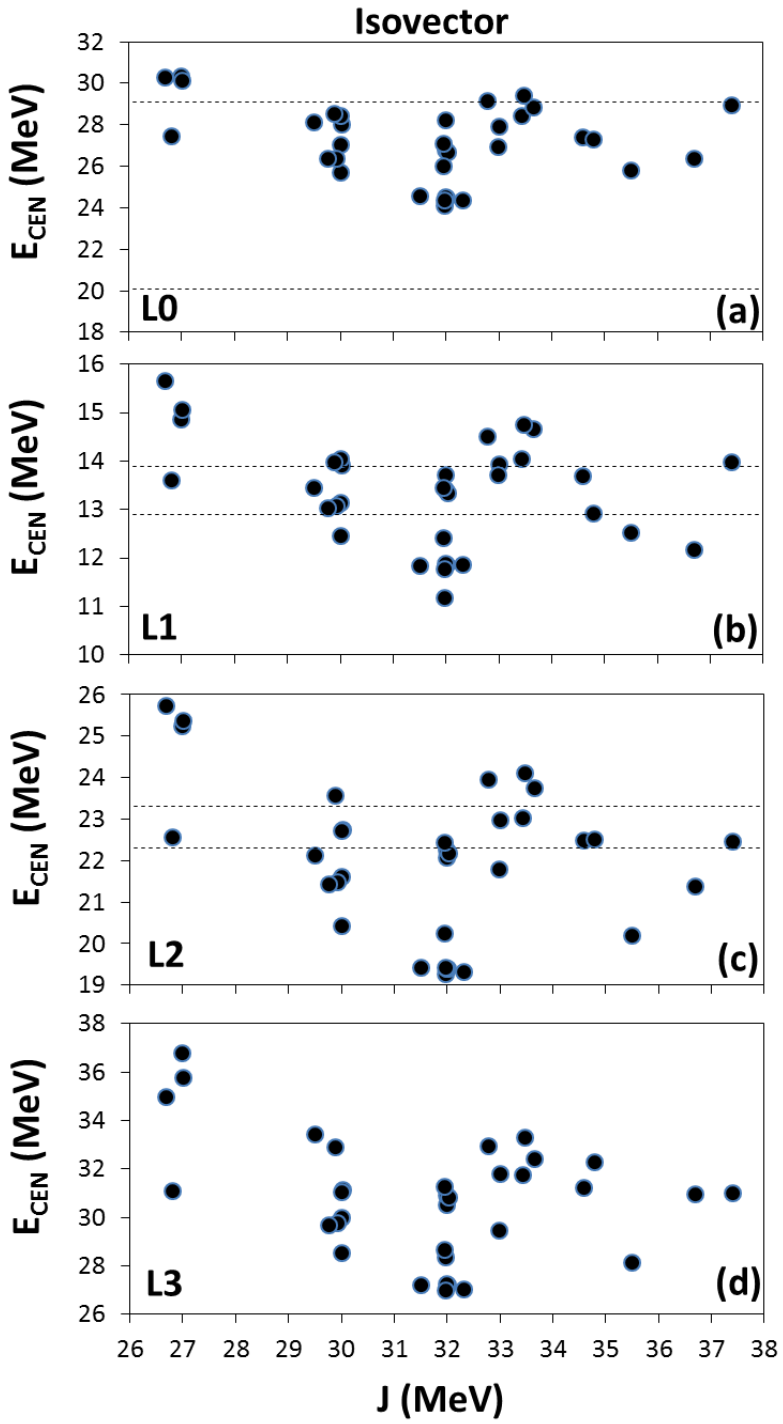

Figure 28 Same as Figure 27 except as a function of J.

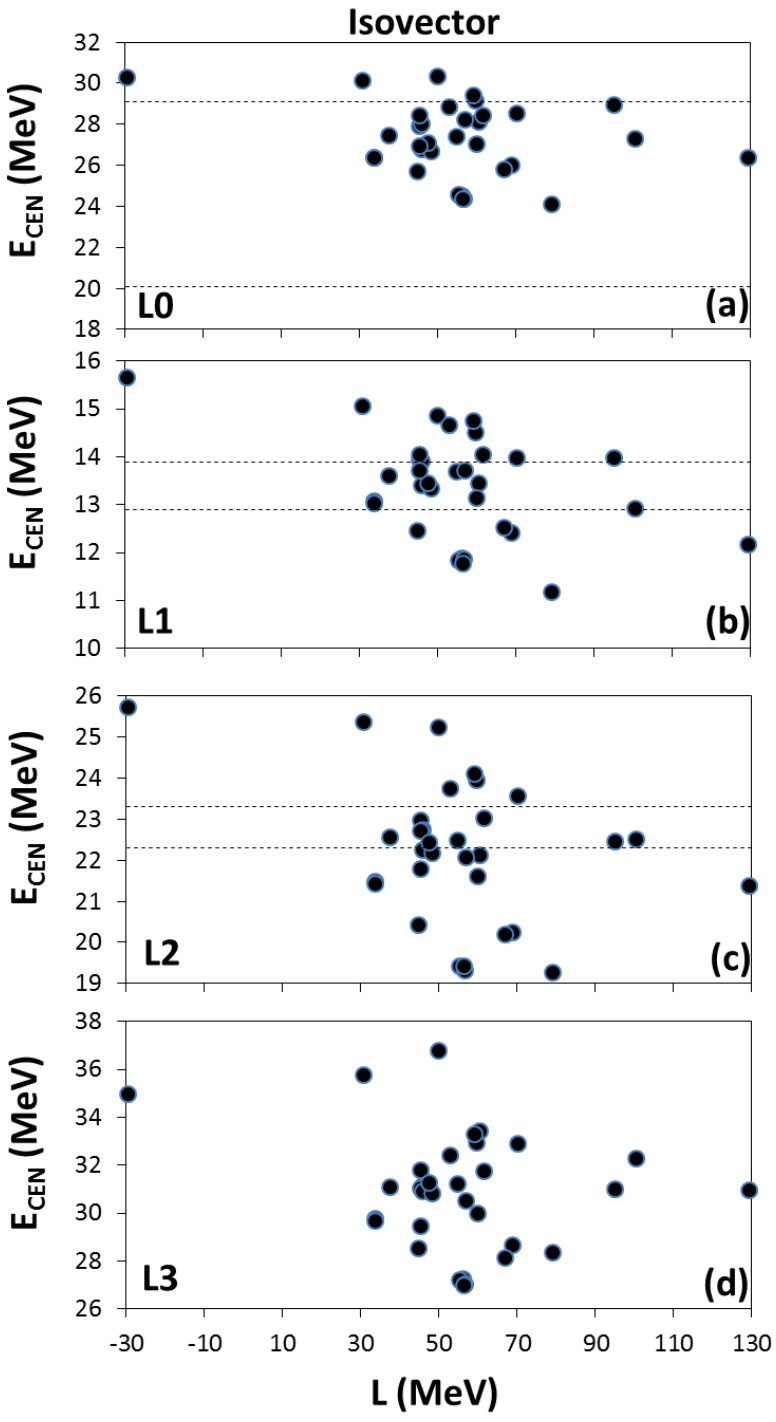

Figure 29 Same as Figure 27 except as a function of L.

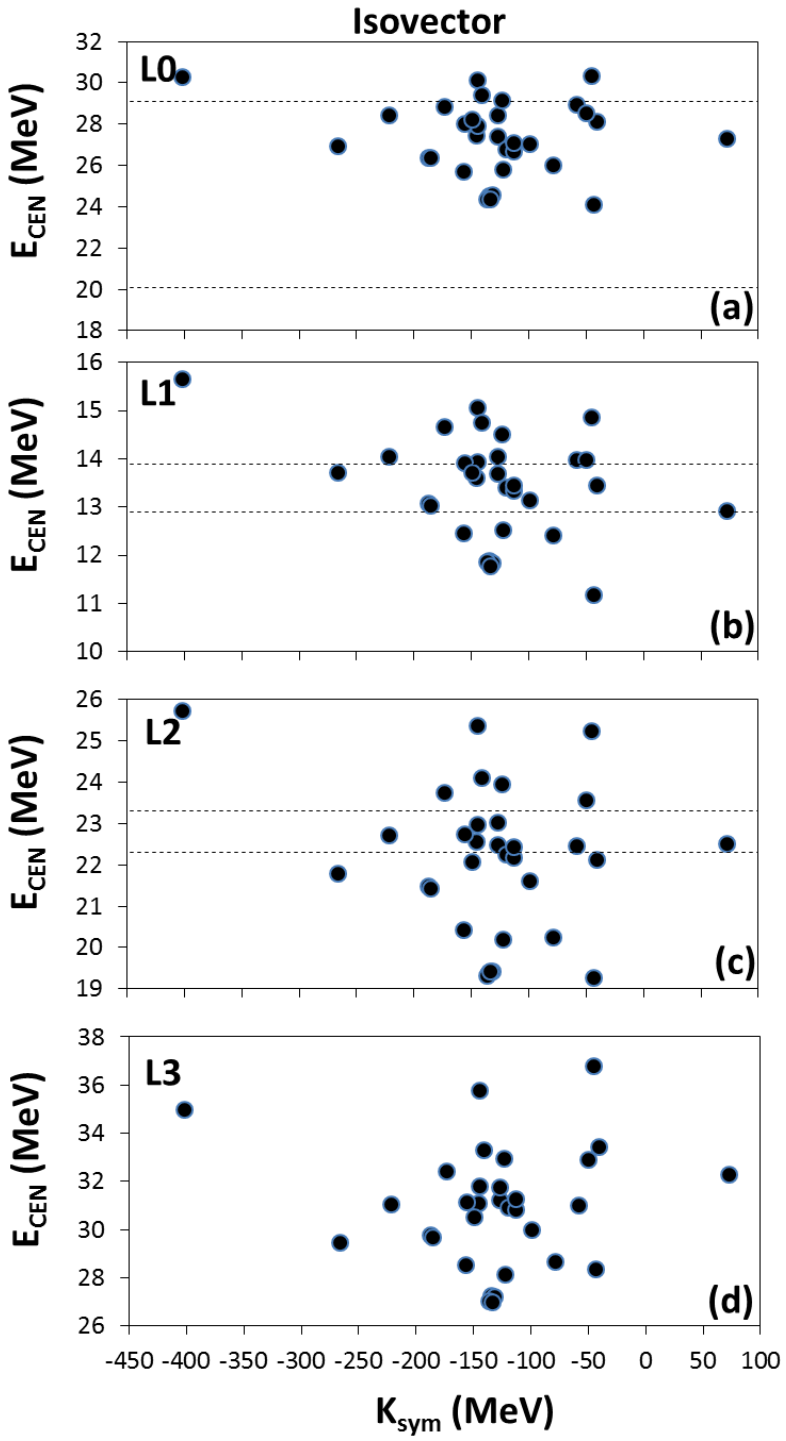

Figure 30 Same as Figure 27 except as a function of K_{sym}.

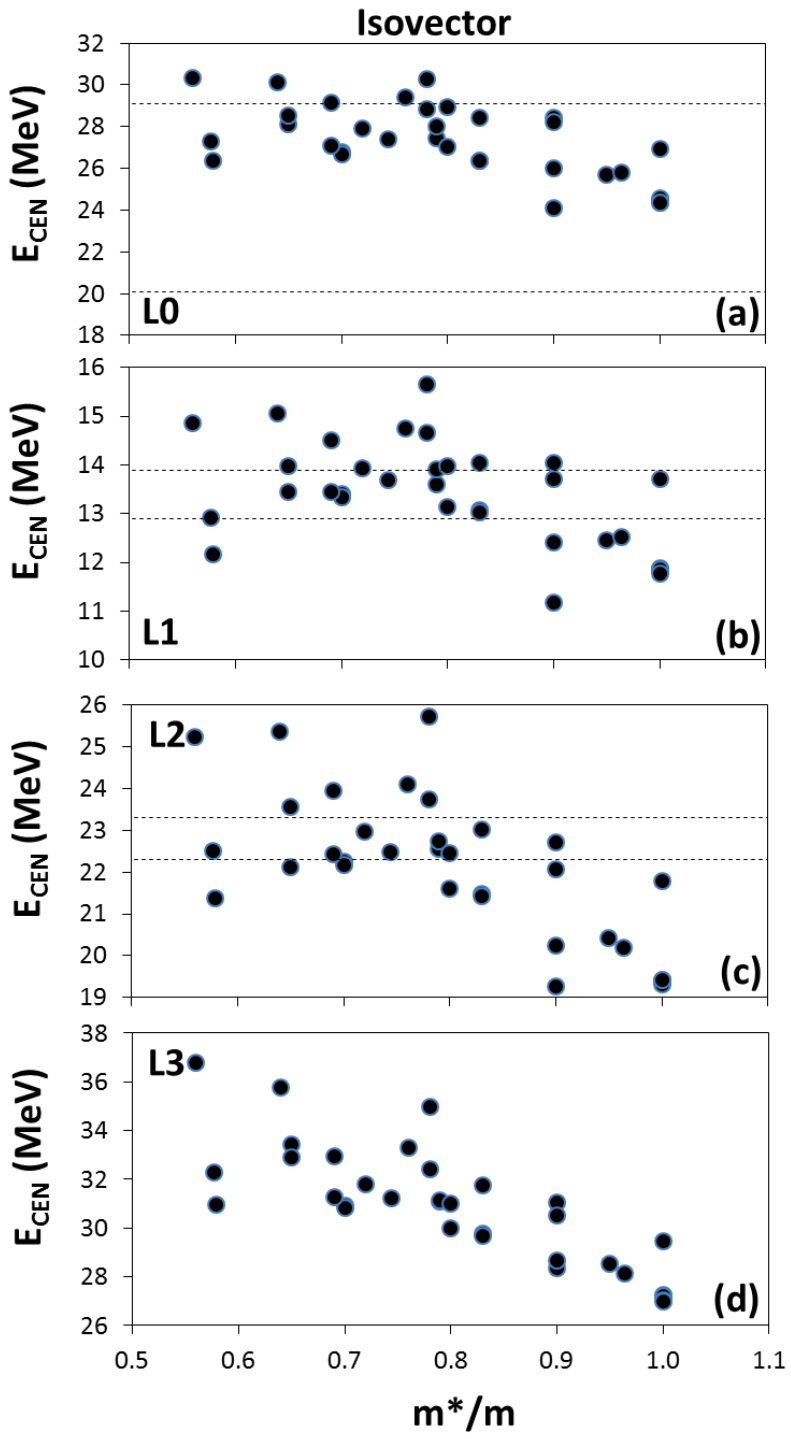

Figure 31 Same as Figure 27 except as a function of m*/m.

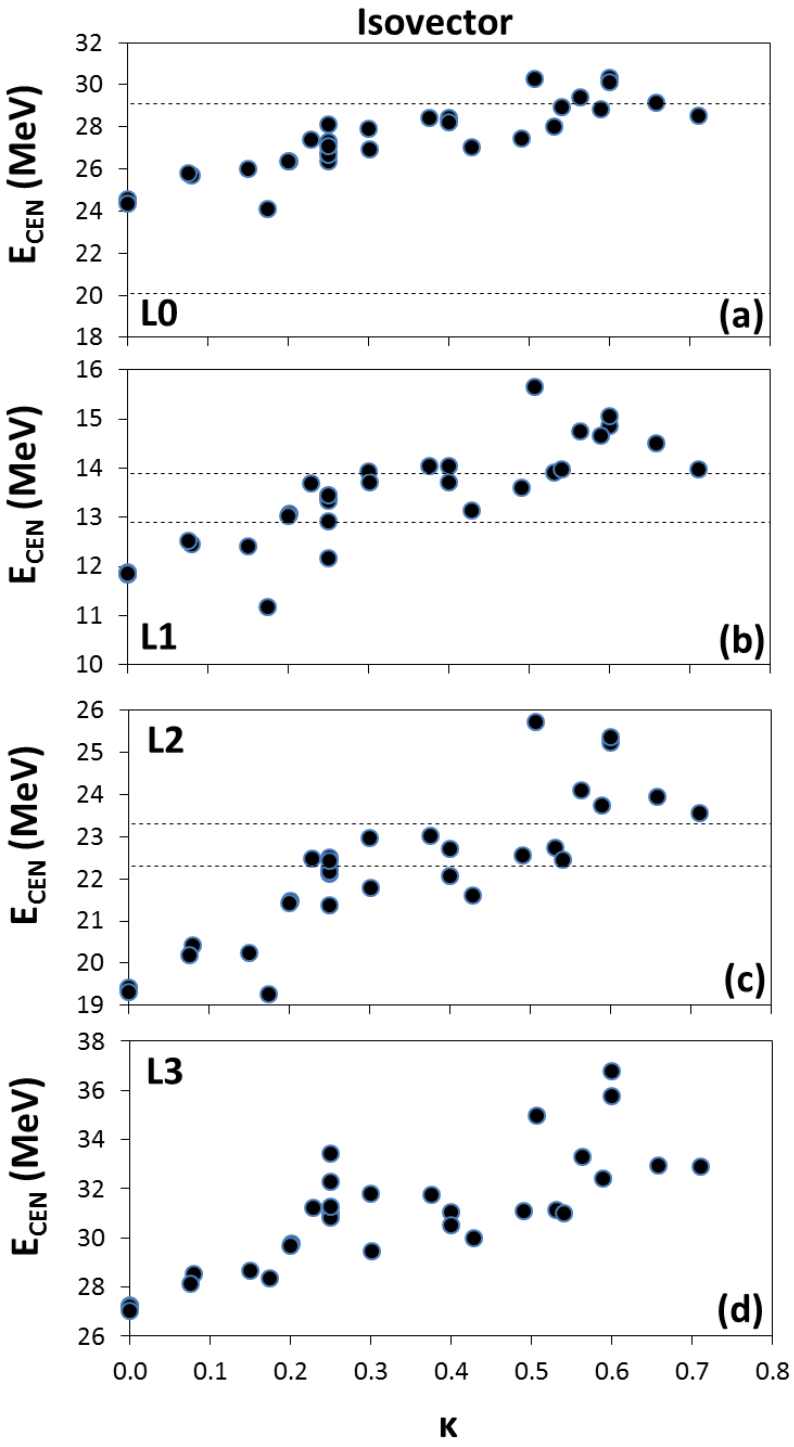

Figure 32 Same as Figure 27 except as a function of κ.

IVGMR

In Figures 27a, 28a, 29a, 30a, 31a, and 32a we compare the experimental data [10] of the IVGMR centroid energies of ^{208}Pb with the results of fully self-consistent HF-based RPA calculations (full circles), obtained using the 34 Skyrme interactions of Table 1 plotted as a function of K_{NM}, J, L, K_{sym}, m*/m, and κ, respectively. The experimental values of E_{CEN} = 26 +/- 2 MeV [10] are plotted as the regions between the dashed lines. We find a strong correlation between E_{CEN} of the IVGMR with κ, a medium correlation with m*/m, and a weak correlation with K_{NM}, J, L or $K_{sym.}$ It can be seen from Figure 28a that a stronger correlation between the IVGMR energy and K_{NM} is obtained for a fixed value of J (at 27 and 30 MeV).

IVGDR

In Figures 27b, 28b, 29b, 30b, 31b, and 32b we compare the experimental data [10] of the IVGDR centroid energies of ^{208}Pb with the results of fully self-consistent HF-based RPA calculations (full circles), obtained using the 34 Skyrme interactions of Table 1 plotted as a function of K_{NM}, J, L, K_{sym}, m*/m, and κ, respectively. The experimental values of E_{CEN} = 13.4 +/- 0.5 MeV [70] are plotted as the regions between the dashed lines. Weak correlations can be seen between E_{CEN} of ^{208}Pb with the parameters of the symmetry energy: J, L, and K_{sym}. We find a medium correlation between E_{CEN} of the IVGMR with κ and a medium correlation with m*/m. Figure 32b shows the IVGDR centroid energies as a function of κ, the enhancement factor in the EWSR of the IVGDR. A strong positive correlation between the IVGDR centroid energy of ^{208}Pb with κ is seen in the Figure and is consistent with κ = 0.2 – 0.5.

IVGQR

In Figures 27c, 28c, 29c, 30c, 31c, and 32c we compare the experimental data [10] of the IVGDR centroid energies of ^{208}Pb with the results of fully self-consistent HF-based RPA calculations (full circles), obtained using the 34 Skyrme interactions of Table 1 plotted as a function of K_{NM}, J, L, K_{sym}, m*/m, and κ, respectively. The experimental values of E_{CEN} = 23.00 +/- 0.22 MeV [71], E_{CEN} = 20.2 +/- 0.5 MeV [72], E_{CEN} = 24.3 +/- 0.4 MeV [73], E_{CEN} = 22.5 +/- 1.0 MeV [74], and E_{CEN} = 23 +/- 0.5 MeV [75], are plotted as the regions between the dashed lines as 22.8 +/- 0.5 MeV. Strong correlations between m*/m and E_{CEN} of ^{208}Pb can be seen in Figure 31c. We find a strong correlation between E_{CEN} of the IVGMR with κ.

IVGOR

In Figures 27d, 28d, 29d, 30d, 31d, and 32d we show the results of fully self-consistent HF-based RPA calculations (full circles) of the IVGOR, obtained using the 34 Skyrme interactions of Table 1 plotted as a function of K_{NM}, J, L, K_{sym}, m*/m, and κ, respectively. Strong correlations between m*/m and κ with E_{CEN} of ^{208}Pb can be seen in Figures 31d and 32d. For completeness we present in Table 12 the centroid energies of the isoscalar (T1) giant resonances of multipolarities L= 0 – 3 for each of the 34 interactions used and in Table 13 the values of the Pearson correlations coefficients among the various NM properties and spin-orbit strength W_0 with the centroid energies of the isoscalar (T1) giant resonances of multipolarities L= 0 – 3. The isovector giant resonances for ^{208}Pb are consistent with K_{NM} ~ 235 MeV, J ~ 32 MeV, L ~ 45 MeV, K_{sym} ~ -140 MeV, m*/m ~ 0.6 – 0.9, and κ ~ 0.2 – 0.5.

Table 12. Isovector centroid energies. Isovector centroid energies of ^{208}Pb for the 34 Skyrme interactions for multipolarities $L = 0 - 3$.

	L0	L1	L2	L3
SGII	27.47	13.60	22.55	31.10
KDE0	27.91	13.94	22.98	31.78
KDE0v1	27.41	13.68	22.49	31.21
SKM*	28.00	13.91	22.74	31.14
SK255	28.94	13.97	22.46	31.02
SkI3	27.29	12.93	22.50	32.27
SkI4	28.11	13.44	22.13	33.43
SkI5	26.38	12.17	21.36	30.94
SV-bas	28.43	14.04	22.71	31.05
SV-min	25.72	12.46	20.42	28.52
SV-sym32	28.22	13.72	22.07	30.52
SV-m56-O	30.32	14.85	25.25	36.78
SV-m64-O	30.14	15.06	25.38	35.76
SLy4	26.79	13.39	22.24	30.92
SLy5	26.69	13.34	22.17	30.83
SLy6	27.11	13.46	22.43	31.28
SkMP	28.53	13.97	23.55	32.88
SkP	26.96	13.72	21.78	29.46
SkO	24.08	11.17	19.26	28.37
SkO'	26.00	12.40	20.25	28.64
LNS	28.44	14.05	23.03	31.76
MSL0	27.02	13.14	21.62	29.97
NRAPR	29.14	14.51	23.95	32.93
SQMC650	28.83	14.66	23.74	32.43
SQMC700	29.43	14.75	24.09	33.31
SkT1	24.47	11.87	19.39	27.19
SkT2	24.53	11.87	19.39	27.23
SkT3	24.56	11.85	19.41	27.21
SkT8	26.38	13.07	21.47	29.75
SkT9	26.35	13.03	21.42	29.69
SkT1*	24.38	11.86	19.31	27.03
SkT3*	24.38	11.78	19.41	26.99
Skxs20	25.81	12.52	20.20	28.14
Z_σ	30.30	15.64	25.73	34.99
Experiment	26.00	13.40	22.80	
Error	2.00	0.50	0.50	

Table 13. Isovector Pearson correlation coefficients. Pearson correlation coefficients among the various NM properties and spin-orbit strength W_0 with the centroid energies of the isovector T1 giant resonances of ^{208}Pb for multipolarities *L= 0 – 3*.

	L0	L1	L2	L3
K	0.08	-0.06	0.08	0.23
J	-0.25	-0.30	-0.32	-0.34
L	-0.26	-0.44	-0.34	-0.22
K_{sym}	-0.17	-0.37	-0.19	0.00
m*/m	-0.65	-0.54	-0.71	-0.82
κ	0.90	0.86	0.87	0.82
$W_0(x_w=1)$	-0.04	-0.05	0.03	0.08

For completeness we also present in Table 14 the centroid energies for all of the giant resonances energies for ^{208}Pb that experimental data is available of the 34 interactions and the χ^2 for each interaction. SV-sym32 has the best fit to the experimental giant resonance data with a χ^2 = 3.5, with m*/m = 0.90, K_{NM} = 234 MeV, J = 32 MeV, L = 57 MeV, K_{sym} = -149 MeV, and κ = 0.40

Table 14. Giant resonance centroid energies of ^{208}Pb. Giant resonance centroid energies of ^{208}Pb for the 34 Skyrme interactions for multipolarities $L = 0 – 3$ and $T = 0$ - 1, except $L3T1$ with χ^2 for each interaction.

	L0 T0	L1 T0	L2 T0	L3 T0	L0 T1	L1 T1	L2 T1	χ^2
SGII	13.48	23.95	11.74	21.57	27.47	13.60	22.55	7.1
KDE0	13.70	24.72	12.12	22.19	27.91	13.94	22.98	13.2
KDE0v1	13.64	24.54	12.08	22.50	27.41	13.68	22.49	12.6
SKM*	13.34	23.74	11.47	20.85	28.00	13.91	22.74	5.3
SK255	14.18	24.38	11.17	20.68	28.94	13.97	22.46	7.1
SkI3	14.82	25.16	13.70	23.66	27.29	12.93	22.50	30.2
SkI4	14.42	25.23	12.52	23.06	28.11	13.44	22.13	20.8
SkI5	14.46	25.42	13.03	23.53	26.38	12.17	21.36	27.6
SV-bas	13.90	23.82	10.98	20.06	28.43	14.04	22.71	3.7
SV-min	13.53	23.19	10.68	19.56	25.72	12.46	20.42	4.7
SV-sym32	13.81	23.72	11.00	20.25	28.22	13.72	22.07	3.5
SV-m56-O	14.66	26.13	14.31	23.13	30.32	14.85	25.25	44.6
SV-m64-O	14.28	25.33	13.00	23.70	30.14	15.06	25.38	30.1
SLy4	13.77	24.52	12.14	22.27	26.79	13.39	22.24	12.0
SLy5	13.73	24.54	12.14	22.29	26.69	13.34	22.17	12.2
SLy6	13.83	24.80	12.26	22.33	27.11	13.46	22.43	14.1
SkMP	13.87	24.15	12.69	23.01	28.53	13.97	23.55	14.4
SkP	12.77	22.23	10.33	18.87	26.96	13.72	21.78	5.1
SkO	13.99	23.75	11.16	20.39	24.08	11.17	19.26	11.2
SkO'	13.31	23.26	10.65	20.14	26.00	12.40	20.25	6.1
LNS	13.57	24.41	12.11	22.20	28.44	14.05	23.03	11.7
MSL0	13.58	23.76	11.32	21.02	27.02	13.14	21.62	5.2
NRAPR	13.37	24.27	11.78	23.36	29.14	14.51	23.95	14.9
SQMC650	13.37	24.11	11.99	21.75	28.83	14.66	23.74	10.3
SQMC700	13.67	24.72	12.37	22.38	29.43	14.75	24.09	16.1
SkT1	13.86	23.21	10.43	19.52	24.47	11.87	19.39	7.8
SkT2	13.87	23.25	10.47	19.71	24.53	11.87	19.39	7.9
SkT3	13.77	23.16	10.32	19.59	24.56	11.85	19.41	7.9
SkT8	13.89	24.05	11.20	20.91	26.38	13.07	21.47	5.9
SkT9	13.88	24.08	11.26	20.87	26.35	13.03	21.42	6.2
SkT1*	13.79	23.07	10.25	19.05	24.38	11.86	19.31	8.2
SkT3*	13.69	22.89	10.08	19.07	24.38	11.78	19.41	8.1
Skxs20	12.73	24.29	10.61	19.46	25.81	12.52	20.20	13.1
Z_σ	14.01	25.03	12.13	22.12	30.30	15.64	25.73	21.2
experiment	13.96	22.2	10.89	19.6	26	13.4	22.8	
error	0.2	0.3	0.3	0.5	2	0.5	0.5	

Electric polarizability

The electric polarizability, α_D, is of special interest because it has been suggested as a good proxy to determine the neutron skin, $r_n - r_p$, of ^{208}Pb, since according to Reinhard and Nazarewicz [76] there is a high correlation between α_D and $r_n - r_p$. The electric polarizability has been experimentally measured as α_D = 20.1 +/- 0.6 fm^3 and with the high correlation between α_D and $r_n - r_p$ found by Reinhard and Nazarewicz, the neutron skin of ^{208}Pb had been predicted to be $r_n - r_p = 0.156^{+0.025}_{-0.021}$ fm [70]. The neutron skin and the electric polarizability are calculated within the HF-RPA by using respectively, the neutron and proton densities and the inverse energy weighted sum rule (IEWSR), m_{-1}, of the IVGDR strengths distribution from eq. (2.52) with *k* = -1 and the upper limit energy cut off set at 60 MeV and e^2 = 1.44 MeV fm.

$$m_{-1} = \int_0^{60} E^{-1} S(E)\, dE \ . \tag{4.1}$$

$$\alpha_D = \frac{24\pi e^2}{9} m_{-1} \tag{4.2}$$

$$\langle r_q^2 \rangle = \int r^2 \rho_q(r) 4\pi r^2 dr \Big/ \int \rho_q(r) 4\pi r^2 dr \ , \tag{4.3}$$

where $\rho_q(r)$ is the HF ground-state neutron (q = n) or proton (q = p) density distribution which is used to find the neutron skin,

$$r_n - r_p = \sqrt{\langle r_n^2 \rangle} - \sqrt{\langle r_p^2 \rangle} \ . \tag{4.4}$$

The results obtained using the Skyrme interactions of Table 1 are plotted in Figure 33 as electric polarizability versus the neutron skin. Unlike Reinhard and Nazarewicz which found a strong correlation of C = 0.98 [76], our results indicate a weaker correlation of C = 0.67. Several Skyrme forces with neutron skins between 0.138

and 0.211 fm fall within or are very close to the experimental range of α_D as compared to $0.156^{+0.025}_{-0.021}$ fm [70]. These results indicate that the electric polarizability is not a good proxy to help determine the neutron skin of ^{208}Pb. Our method takes 34 Skyrme forces which were fitted to varying data sets and which have various NM parameters and electric polarizabilities and neutron skins of ^{208}Pb to determine the correlation between the electric polarizability and neutron skin of ^{208}Pb. The Skyrme force is fitted to a data set and varying the parameters destroys the initial fit. The method of varying the parameters of a single Skyrme force to determine the correlation among the various NM coefficients and other parameters such as the electric polarizability of ^{208}Pb is called into question as a valid method. Perhaps varying one fixed parameter for several separate fits would give a better indication of the effect of differing values for the fixed parameter on other calculated values such as the electric polarizability.

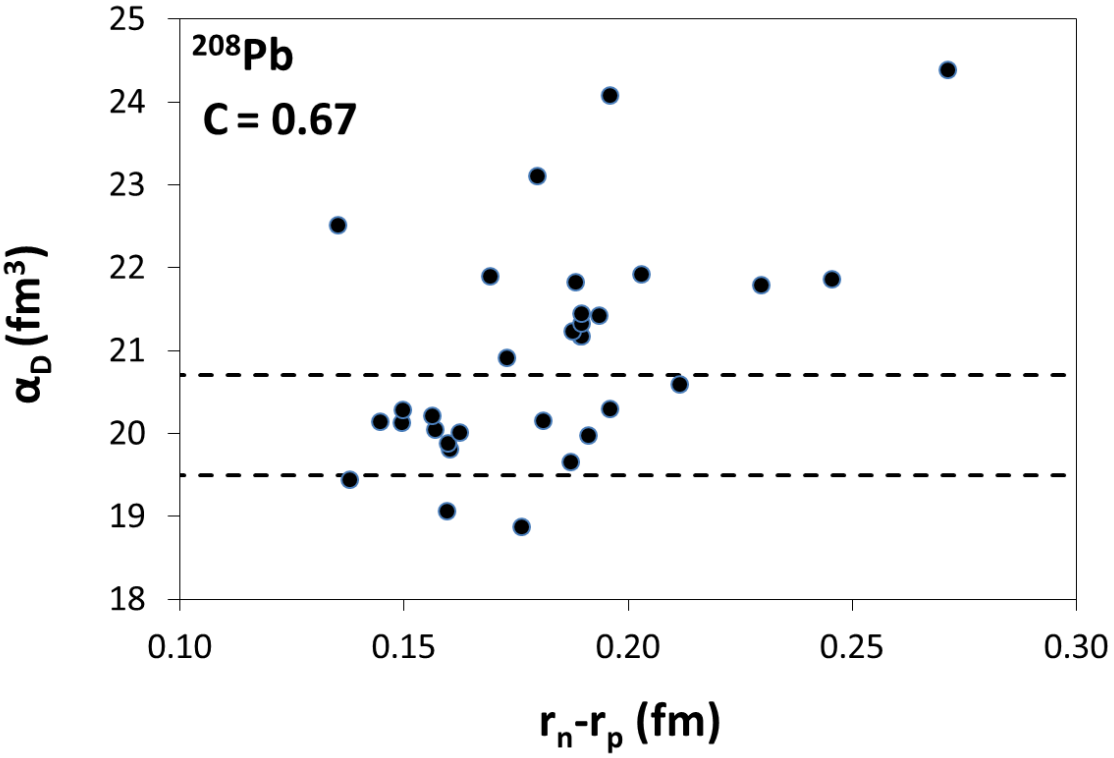

Figure 33 Comparison of experimental data [70] of the electric polarizability, α_D, of ^{208}Pb, shown as the regions between the dashed lines and the results of fully self-consistent HF based RPA calculations of α_D of ^{208}Pb (full circles) obtained using the Skyrme interactions of Table 1, with the HF calculations of the neutron skin, $r_n - r_p$, of ^{208}Pb.

"Since the correlation between polarizability, neutron skin thickness, and symmetry energy is model dependent, viz. $r_{\text{skin}} \propto \alpha_D \cdot a_{\text{sym}}$ [$r_n - r_p \propto \alpha_D J$] [77], a systematic study with a variety of EDFs as well as experimental tests in other nuclei would be important" [70]. The results obtained using the Skyrme interactions of Table 1 are plotted in Figure 34 as the product of the electric polarizability with symmetry energy at saturation density versus the neutron skin of ^{208}Pb. Our results indicate a correlation of C

= 0.91 which is much stronger than the correlation, C = 0.67, of just electric polarizability with neutron skin of ^{208}Pb. Several Skyrme forces with neutron skins between 0.135 and 0.211 fm fall within or are very close to the experimental range of $\alpha_D J$ = 653 +/- 70 MeV with 30 < J < 35 MeV [40] or J = 32.5 MeV +/- 2.5 MeV as compared to $0.156^{+0.025}_{-0.021}$ fm [70]. For completeness, Table 14 is provided to show the values of J, r_n, r_p, $r_n - r_p$, m_{-1}, α_D, and $\alpha_D J$.

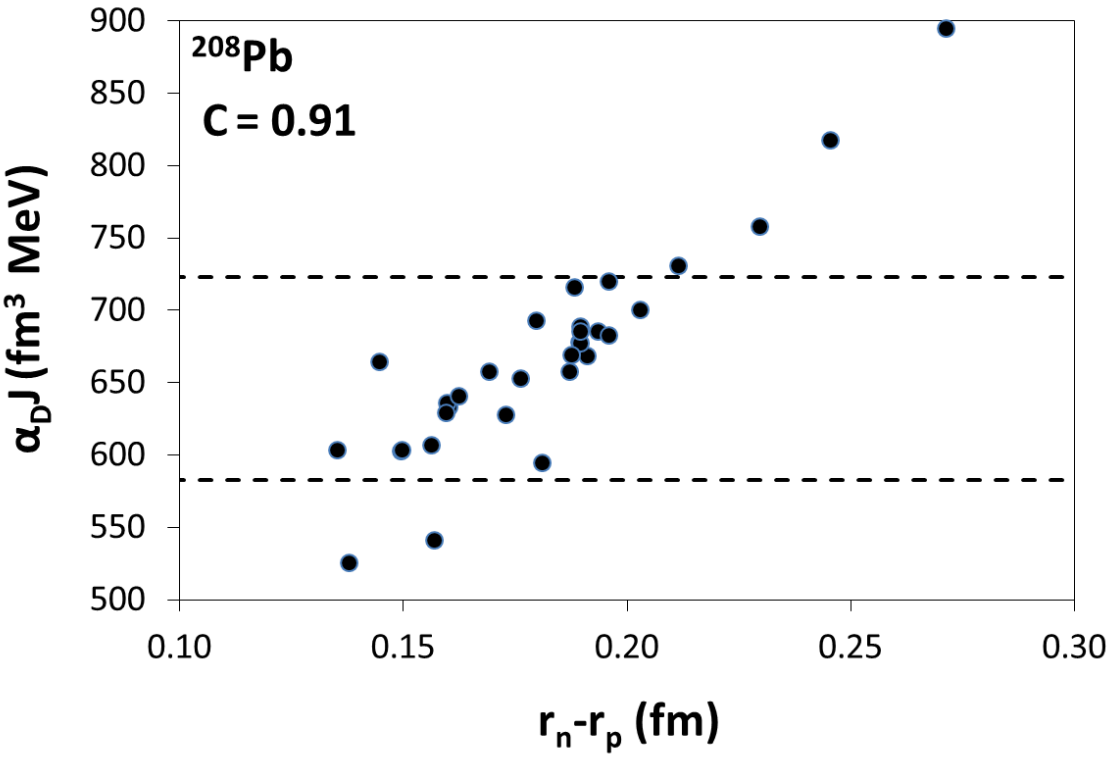

Figure 34 Comparison of the product of the experimental data [70] of the electric polarizability, α_D, with symmetry energy at saturation density, J, of ^{208}Pb, shown as the regions between the dashed lines and the results of fully self-consistent HF based RPA calculations of $\alpha_D J$ of ^{208}Pb (full circles) obtained using the Skyrme interactions of Table 1, with the HF calculations of the neutron skin, $r_n - r_p$, of ^{208}Pb.

Table 15. Electric Polarizability and Neutron Skin. Values for the symmetry energy at saturation density, J [MeV], neutron root mean square (rms) radius, r_n [fm], proton rms radius r_p [fm], neutron skin, $r_n - r_p$ [fm], inverse energy weighted sum rule, m_{-1} [fm^6 MeV^{-1}], electric polarizability α_D [fm^3], and $\alpha_D J$ [fm^3 MeV].

	J	r_n	r_p	r_n-r_p	m_{-1}	α_D	$\alpha_D J$
SGII	26.80	5.591	5.455	0.135	1.866	22.52	603
KDE0	33.00	5.600	5.440	0.160	1.580	19.06	629
KDE0v1	34.58	5.584	5.407	0.176	1.565	18.88	653
SKM*	30.03	5.622	5.453	0.169	1.815	21.89	657
SK255	37.40	5.705	5.459	0.246	1.812	21.86	817
SkI3	34.80	5.621	5.392	0.230	1.806	21.78	758
SkI4	29.50	5.607	5.426	0.181	1.671	20.16	595
SkI5	36.70	5.706	5.434	0.271	2.021	24.38	895
SV-bas	30.00	5.617	5.461	0.156	1.676	20.21	606
SV-min	30.01	5.647	5.474	0.173	1.734	20.91	628
SV-sym32	32.00	5.660	5.466	0.194	1.776	21.42	685
SV-m56-O	27.00	5.607	5.450	0.157	1.661	20.04	541
SV-m64-O	27.01	5.584	5.446	0.138	1.612	19.45	525
SLy4	32.00	5.617	5.458	0.160	1.648	19.87	636
SLy5	32.03	5.614	5.452	0.162	1.659	20.01	641
SLy6	31.96	5.616	5.456	0.160	1.642	19.81	633
SkMP	29.88	5.644	5.448	0.196	1.996	24.08	720
SkP	32.98	5.610	5.465	0.145	1.669	20.14	664
SkO	31.97	5.538	5.477	0.060	2.307	27.83	890
SkO'	31.95	5.653	5.450	0.203	1.817	21.92	700
LNS	33.43	5.456	5.268	0.187	1.630	19.66	657
MSL0	30.00	5.643	5.464	0.180	1.915	23.10	693
NRAPR	32.78	5.665	5.476	0.188	1.810	21.83	716
SQMC650	33.65	5.545	5.349	0.196	1.682	20.29	683
SQMC700	33.47	5.509	5.317	0.191	1.656	19.98	669
SkT1	32.02	5.625	5.435	0.189	1.755	21.17	678
SkT2	32.00	5.620	5.431	0.190	1.755	21.17	677
SkT3	31.50	5.626	5.439	0.188	1.760	21.23	669
SkT8	29.92	5.594	5.445	0.149	1.669	20.13	602
SkT9	29.76	5.593	5.443	0.150	1.682	20.29	604
SkT1*	32.31	5.641	5.451	0.190	1.768	21.32	689
SkT3*	31.97	5.652	5.462	0.190	1.777	21.44	686
Skxs20	35.49	5.648	5.436	0.211	1.707	20.60	731
Z_σ	26.71	5.450	5.394	0.056	1.424	17.18	459
				Correlation with r_n-r_p		0.67	0.91

Conclusions

We have presented results of our fully self-consistent HF-RPA calculations using 34 commonly employed Skyrme type interactions of Table 1, for the centroid energies of isoscalar and isovector giant resonances of multipolarities $L = 0 - 3$ along with the electric polarizability and neutron skin of ^{208}Pb and compared with available experimental data. We have investigated and discussed the sensitivity of the E_{CEN} of the giant resonances to various properties of NM and the correlation between the electric polarizability and the neutron skin. In particular we point out that:

- We have demonstrated the very strong to strong correlations of the E_{CEN} of the compression mode, the ISGMR, with the NM incompressibility coefficient K_{NM} and noted that the sensitivity of E_{CEN} to the effective mass is a reflection of the correlation between m*/m and K_{NM}, existing in the Skyrme interactions used in our calculations.
- For all the adopted Skyrme interactions, the calculated centroid energies of the ISGDR in ^{208}Pb are consistently higher than the experimental data (by about 0.5 – 3 MeV) except for the interaction SkP.
- We have demonstrated the very strong correlation of E_{CEN} of the ISGQR and the ISGOR with m*/m. We have found that an agreement with the experimental data for E_{CEN} of the ISGQR in ^{208}Pb is obtained for a value of the effective mass in the range of m*/m = 0.9 – 1.0.

- For the IVGMR of ^{208}Pb, the isovector compression mode, we find a strong correlation with κ, a medium correlation with m*/m, and a weak correlation with K_{NM}, J, L or $K_{sym.}$
- We find a weak correlation between the energies of the IVGDR of ^{208}Pb and the quantities associated with the density dependence of the symmetry energy.
- We find a strong correlation between the energies of the IVGMR, IVGDR, IVGQR, and IVGOR of ^{208}Pb and the value of κ.
- For the IVGQR and IVGOR we find a strong correlation between E_{CEN} and m*/m. Using this result we can predict that the values of the E_{CEN} of the IVGOR in ^{208}Pb should be in the region of 27 – 32 MeV.
- Unlike Reinhard and Nazarewicz which found a strong correlation of C = 0.98, our results indicate a weaker correlation of C = 0.67 between the electric polarizability and the neutron skin casting into doubt the result of $r_n - r_p = 0.156^{+0.025}_{-0.021}$ fm and the method of varying the parameters of individual Skyrme forces to the determine correlation between electric polarizability and the neutron skin of ^{208}Pb .
- The correlation of C = 0.91 of the product of the electric polarizability with symmetry energy at saturation density is much stronger than the correlation, C = 0.67, of just electric polarizability with neutron skin of ^{208}Pb yielding a much tighter range for the neutron skin of between 0.169 and 0.187 fm versus between 0.138 and 0.211 fm.

The disagreement between the HF-RPA results except for the SkP interaction and the experimental data for the centroid energies of the ISGDR in ^{208}Pb remain an unsolved problem which calls for possible extensions of the EDF used in the work, microscopic calculations of the excitation cross sections of giant resonances [58,66] and/or going beyond the HF-RPA theory [67]. As discussed in Ref. [40], the Skyrme potential is a phenomenological density-dependent interaction which contains 2-body and 3-body correlations. All of the physical information is contained within the parameters, however since the force is phenomenological, the microscopic details of the 2-body and 3-body forces are lost. The goal of using the Skyrme potential is to find an effective potential which best describes the ground state properties of nuclei and their excited states such as giant resonances for light to heavy nuclei and then to proceed to glean information about the parameters of the equation of state of asymmetric nuclear matter. This study has been carried out to find better constraints on the parameters of nuclear matter such that a new search for a better Skyrme force can take place.

CHAPTER V

MEASURED DIFFERENCE BETWEEN ^{206}PB, ^{205}TL CHARGE DISTRIBUTIONS AND THE PROTON $3S_{1/2}$ WAVE FUNCTION

Introduction

The shell model, which is based on the assumption that nucleons in the atomic nucleus move independently in single particle orbits associated with a single particle potential, has been very successful in explaining many features of nuclei [27]. In determining the nuclear mean-field potential, it is common to: (i) parametrize the central potential, using for example the WS form, and determine the parameters by a fit of calculated properties, such as single particle energy and reaction cross-sections, to the corresponding experimental data [1]; and (ii) by carrying out Hartree-Fock calculations using a parametrized effective two-body interaction and determine the parameters by a fit to experimental data and deduce the mean-field potential [28]. We present a novel method [78], using the single particle Schrödinger equation for a wave function $\Psi(\vec{r})$ with eigenenergy E, to determine the central potential $V(\vec{r})$ directly from the measured single particle matter density, $\rho(\vec{r}) = [\Psi(\vec{r})]^2$ and its first and second derivatives, assuming these are known for all $\vec{r}$.

A well-known important test of the shell model is the experimental measurement of the charge distribution of the proton $3s_{1/2}$ orbit given by the charge density difference, $\Delta\rho_c(r)$, between charge density distributions of the isotones ^{206}Pb – ^{205}Tl, determined by analysis of elastic electron scattering measurements [29,30]. The experimental data for

the $3s_{1/2}$ charge density shows a clear maximum at the center of ^{206}Pb with two additional maxima, which nicely corresponds to the shape of the shell model $3s_{1/2}$ proton orbit, in agreement with the simple shell model. It was pointed out [31] that commonly used central potentials, such as the WS potential, lead to a $3s_{1/2}$ charge density in disagreement with experimental data. In particular, the central density obtained from the WS potential is too large by 40%.

This difference between data and the WS results was attributed in Ref. [31] to be due to the effects of two-body short range correlations. Using our new method, we look for the single particle nuclear potential that corresponds to the experimental charge density associated with the proton $3s_{1/2}$ orbit in ^{206}Pb. We point out that the resulting single particle potential, if found, will provide a stringent limit on the effects of short correlations on the expected values of long-range operators, an important test for the shell model. The potential can also be used as an additional experimental constraint in determining a modern energy density functional (EDF) for more reliable prediction of properties of nuclei and nuclear matter [28,32].

In the second section we consider the single particle Schrödinger equation and describe the method for determining the single particle potential $V(\vec{r})$ from a given single particle wave function $\Psi(\vec{r})$ or matter density, $\rho(\vec{r}) = [\Psi(\vec{r})]^2$, assuming it is known for all $\vec{r}$ [27]. In particular, we consider the case of spherical symmetry. We also describe the method of deducing the point proton density from the charge distribution determined in electron scattering measurements. In the third section we present results for the case of the experimental data [29,30] for the charge density difference between

the close $(\Delta Z = 1)$ isotones ^{206}Pb – ^{205}Tl, associated with the $3s_{1/2}$ proton single particle orbit, and determine the corresponding single particle potential. In the last section we present our conclusions.

Determining single particle potential from single particle matter density

Consider the single particle Schrödinger equation,

$$-\frac{\hbar^2}{2m}\Delta\Psi + V\Psi = E\Psi\ , \tag{5.1}$$

where $V(\vec{r})$ is a real local and non-singular potential and $\Delta = \vec{\nabla}\cdot\vec{\nabla}$, with $\vec{\nabla}$ being the gradient operator. Using Eq. (5.1) we have that for a given single particle wave function $\Psi(\vec{r})$ known for all $\vec{r}$ and given eigenvalue *E*, the corresponding single particle potential *V* is uniquely determined [27] from

$$V(\vec{r}) = E + \frac{\hbar^2}{2m}S(\vec{r})\ , \qquad S(\vec{r}) = \frac{\Delta\Psi(\vec{r})}{\Psi(\vec{r})}\ . \tag{5.2}$$

It is important to point out that for a nonsingular *V*, $\Delta\Psi(\vec{r}) = 0$ when $\Psi(\vec{r}) = 0$. In the analysis of experiments, such as electron scattering, one determines the matter density $\rho(\vec{r}) = [\Psi(\vec{r})]^2$, for real Ψ. Operating with Δ on $[\Psi(\vec{r})]^b$, where b is positive and real, and using the relation $\vec{\nabla}\Psi^b = b\Psi^{b-1}\vec{\nabla}\Psi$ with the definition $S(\vec{r}) = \frac{\Delta\Psi(\vec{r})}{\Psi(\vec{r})}$ of Eq. (5.2), we obtain the general relation

$$S(\vec{r}) = \frac{\Delta\,[\Psi(\vec{r})]^b}{b\,[\Psi(\vec{r})]^b} - \frac{b-1}{b^2}\left[\frac{\vec{\nabla}\,[\Psi(\vec{r})]^b}{[\Psi(\vec{r})]^b}\right]^2. \tag{5.3}$$

Note that $\vec{\nabla}\Psi = 0$ and $\Delta[\Psi(\vec{r})]^b = 0$, when $[\Psi(\vec{r})]^b = 0$. Eq. (5.2) is a special case of Eq. (5.3) for *b* = 1. For *b* = 2, we have from Eqs. (5.2) and (5.3) that the potential $V(\vec{r})$ is

given in terms of the corresponding single particle matter density $\rho(\vec{r})$ (for real $\Psi(\vec{r})$) and its first and second derivatives.

In the spherical case we have for the wave function of a nucleon

$$\Psi_{nlj}(\vec{r}) = \frac{R_{nlj}(r)}{r} Y_{lj} \,, \tag{5.4}$$

where $R_{nlj}(r)$ is the (one-dimensional) radial wave function for the orbit with principle number *n*, orbital angular momentum *l* and total angular momentum *j* and Y_{lj} is the known spin harmonic wave function, with the normalization

$$\int R_{nlj}^2 (r) dr = 1 \,. \tag{5.5}$$

The corresponding single particle potential for a nucleon has the form

$$V(r) = V_{cen}(r) + \vec{s} \cdot \vec{l}\, V_{s.o.}(r) + \frac{1}{2}(1 - \tau_z) V_{coul}(r) \,, \tag{5.6}$$

where $V_{cen}(r), \vec{s} \cdot \vec{l}\, V_{s.o.}(r)$ and $\frac{1}{2}(1 - \tau_z) V_{coul}(r)$, are the nuclear central, spin-orbit and coulomb potentials, respectively, and τ_z=1 for a neutron and -1 for a proton. Using Eqs. (5.2), (5.4) and (5.6) the nuclear central potential is given by,

$$V_{cen}(r) = E + \frac{\hbar^2}{2m} S(r) - \frac{\hbar^2}{2m} \frac{l(l+1)}{r} - \frac{1}{2}(1 - \tau_z) V_{coul}(r) - c_{ls}\, V_{s.o.}(r) \,, \tag{5.7}$$

$$S(r) = \frac{d^2 R_{nlj}}{dr^2} \frac{1}{R_{nlj}(r)} \,,$$

where $c_{ls} = -l(l+1)$ and l for $j = l - 1/2$ and $j = l + 1/2$, respectively. The single particle radial density $\rho_{nlj}(r)$ is related to the square of the single particle radial wave function R_{nlj}^2 by

$$R_{nlj}^2(r) = 4\pi r^2 \rho_{nlj}(r) \,. \tag{5.8}$$

Using Eq. (5.1) one can deduce the radial wave-function $R_{nlj}(r)$ and determine the central potential using Eq. (5.4). But this leads to numerical complication, particularly in the vicinity of the nodes of the wave function. From Eq. (5.1) for the radial wave-function $R_{nlj}(r)$ and Eq. (5.3) for b = 2 the corresponding single particle potential V can be obtained from (5.6) by using the simple relation

$$S(r) = \frac{1}{2R_{nlj}^2}\left[\frac{d^2(R_{nlj}^2)}{dr^2} - \frac{1}{2}\left[\frac{1}{R_{nlj}}\frac{d(R_{nlj}^2)}{dr}\right]^2\right]. \tag{5.9}$$

From Eqs. (5.8) and (5.9) we find the relation

$$S(r) = \frac{1}{2\rho_{nlj}}\left[\frac{d^2\rho_{nlj}}{dr^2} + \frac{2}{r}\frac{d\rho_{nlj}}{dr} - \frac{1}{2\rho_{nlj}}\left(\frac{d\rho_{nlj}}{dr}\right)^2\right]. \tag{5.10}$$

Eqs. (5.10) can also be derived from Eq. (5.3) with b = 2 using the (real) three-dimensional wave function and the operators Δ and $\vec{\nabla}$ in spherical coordinates.

As an example, we note that for the single particle radial wave function of the form $R\sim\sin(kr+\varphi)$, an eigenstate of a constant potential, one finds from (5.7) that the corresponding constant potential $V = E - \frac{\hbar^2 k^2}{2m}$. Similarly, for the Harmonic Oscillator $3s_{1/2}$ single particle wave function

$$R_{3s/2}(r) = \left(\frac{15}{2\sqrt{\pi}}\nu^{3/2}\right)^{1/2} re^{-\frac{1}{2}\nu r^2}\left[1 - \frac{4}{3}\nu r^2 + \frac{4}{15}(\nu r^2)^2\right], \tag{5.11}$$

with the size parameter $\nu = \frac{m\omega}{\hbar}$ we have from (5.7) the expected potential

$$V(r) = E - \frac{11}{2}\,\hbar\omega + \frac{1}{2}m\omega^2 r^2\,, \tag{5.12}$$

We note that for the central nuclear potential it is common to use for the WS form,

$$V(r) = V_0/[1 + exp((r - R_1)/\mathrm{a}_0)]\,, \tag{5.13}$$

where, V_0, R_1 and a_0 are the depth, half radius and diffuseness parameters, respectively. Furthermore, for the Coulomb potential we adopt the form obtained from a uniform charge distribution of radius R_{ch},

$$V^{coul}(r) = Ze^2 \begin{cases} (3 - r^2/R_c^2)/2R_c & r < R_{ch} \\ 1/r & r > R_{ch} \end{cases} . \quad (5.14)$$

In Eqs. (5.14), R_{ch} is the equivalent radius determined by the charge root-mean-square radius, $\langle r^2 \rangle_{ch}$

$$R_{ch}^2 = (5/3)\langle r^2 \rangle_{ch} . \quad (5.15)$$

The form of the spin-orbit potential is commonly taken as,

$$V_{s.o.}(r) = c\, dV_{cen.}(r)/dr, \quad (5.16)$$

where *c* is adjusted to the experimental spin-orbit splittings (~ 0.2).

Determining the point proton density from the charge density

In an elastic electron-nucleus scattering measurement, one determines the charge density distribution, $\rho_{ch}(\vec{r})$, by carrying out a phase shift analysis of the cross section [79], whereas in a theoretical model one calculates the point proton density distribution, $\rho_p(\vec{r})$. They are related by,

$$\rho_{ch}(\vec{r}) = \int \rho_p(\vec{r'})\, \rho_{pfs}(\vec{r} - \vec{r'}) d^3\vec{r'} , \quad (5.17)$$

where $\rho_{pfs}(\vec{r})$ is the charge density distribution of a free proton.

From elastic electron scattering on a free proton one finds that,

$$\rho_{pfs}(\vec{r}) = \frac{1}{8\pi a^3} e^{-r/a} , \quad (5.18)$$

where $a^2 = \frac{1}{12} r_{pfs}^2$ with $r_{pfs} = 0.85$ fm being the corresponding charge root mean square (rms) radius. The charge mean square radius is given by

$$\langle r^2 \rangle_{ch} = \int r^2 \rho_{ch}(\vec{r}) d^3\vec{r} \,/ \int \rho_{ch}(\vec{r}) d^3\vec{r}. \tag{5.19}$$

From Eqs. (5.17) and (5.19) one has the relation

$$\langle r^2 \rangle_{ch} = \langle r^2 \rangle_p + \langle r^2 \rangle_{pfs} \,. \tag{5.20}$$

Considering the spherical case, we have using Eqs. (5.17) and (5.18), that

$$\rho_{ch}(\vec{r}) = \frac{1}{4\pi a} \int_0^\infty r' dr' \rho_p(r') \left[\left(1 + \frac{|r-r'|}{a} \right) e^{-|r-r'|/a} - \left(1 + \frac{(r+r')}{a} \right) e^{-(r+r')/a} \right]. \tag{5.21}$$

It is common [79] to define the form factor *F(q)* as the Fourier transform of the density $\rho(r)$ as

$$F(q) = \frac{4\pi}{q} \int_0^\infty \sin(qr)\, \rho(r) r dr. \tag{5.22}$$

The corresponding inverse transform is given by

$$\rho(r) = \frac{1}{(2\pi)^3} \frac{4\pi}{r} \int_0^\infty \sin(qr)\, F(q) q dq \,. \tag{5.23}$$

For the proton charge distribution of Eq. (5.18) we have the dipole form

$$F_{pfs}(q) = \left(1 + \frac{1}{12} r_p^2 q^2 \right)^{-2} . \tag{5.24}$$

For the charge density $\rho_{ch}(r)$, given by the convolution relation of Eq. (5.17) we have the simple relation for the form factors

$$F_{ch}(q) = F_{pfs}(q) F_p(q) \,. \tag{5.25}$$

Eq. (5.25) can be used to determine the form factor $F_p(q)$, associated with the point proton density distribution $\rho_p(r)$, Eq. (5.17). Then $\rho_p(r)$ can be obtained from $F_p(q)$, using (5.23) and compared with theoretical predictions.

Results

We consider the charge density difference,

$$\Delta\rho_c(r) = \rho_{ch}(r;\ ^{206}\text{Pb}) - \rho_{ch}(r;\ ^{205}\text{Tl}), \tag{5.26}$$

between the isotones ^{206}Pb – ^{205}Tl, associated with the proton $3s_{1/2}$ single particle orbit, and determine the corresponding single particle potential. The experimental data for the charge densities, $\rho_{ch}(r)$, of the isotones ^{206}Pb and ^{205}Tl, obtained from accurate elastic electron scattering experiments, are taken from Refs. [29,30], where they are given in term of sums of Gaussian functions of r.

In Fig. 35a we present the experimental data for the charge density difference, $\Delta\rho_c(r)$, between the isotones ^{206}Pb – ^{205}Tl , shown by the solid line. It is normalized to a total charge of one proton (Z=1). The experimental uncertainty is indicated by the dotted lines. Note that the two nodes associated with the proton $3s_{1/2}$ orbit are clearly seen in the figure. The experimental values of the charge rms radii of ^{206}Pb and ^{205}Tl are 5.4897 and 5.4792 fm, respectively, leading to a value of 6.2822 fm for the charge rms radius of the proton $3s_{1/2}$ orbit. To determine the corresponding single particle potential, using Eqs. (5.7) and (5.9) or (5.10), the point proton distribution, $\Delta\rho_p(r)$, is needed. This is obtained by using Eqs. (5.22), (5.24) and (5.25) to determine the point proton form factor, $F_p(q)$, and then employing Eq. (5.23) to obtain $\Delta\rho_p(r)$. The results are shown as a solid line in Figure 35b. The experimental uncertainty is shown by the dotted lines. Using the value of $r_{pfs} = 0.85$ fm in Eq. (5.20), we find that the rms radii of the proton density distributions of ^{206}Pb and ^{205}Tl are 5.4235 and 5.4129 fm, respectively, leading to

a value of 6.2244 fm for the rms radius of the point proton $3s_{1/2}$ orbit. Note that $\Delta\rho_p(r)$ (solid line) is slightly negative at the first node (at ~ 2.6 fm) and above zero at the second node (r ~ 4.9 fm). Moreover, in the vicinity of these minima, the experimental uncertainty in $\Delta\rho_p(r)$ is larger than its value.

We also present in Figure 35a and 35b (dashed line) the charge density $\Delta\rho_{Rc}(r)$ and the point particle density $\Delta\rho_{Rp}(r)$ of the proton $3s_{1/2}$ orbit, respectively, corrected for the rearrangement effect (from ^{205}Tl to ^{206}Pb). We adopted the scaling model to assess the rearrangement effect [80]. The charge distribution of ^{205}Tl is scaled so that the charge rms radius of the scaled density is equal to that of the 81 core protons in ^{206}Pb. We obtained,

$$\Delta\rho_{Rc}(r) = \rho_{ch}(r;\ ^{206}\text{Pb}) - \alpha^3\rho_{ch}(\alpha r;\ ^{205}\text{Tl}), \qquad (5.27)$$

where the scaling parameter α = 5.4792/5.4848 = 0.9990 is the ratio between the charge rms radius of ^{205}Tl to that of the core 81 protons in ^{206}Pb. The value of 5.4848 fm is obtained by adopting the Harmonic Oscillator approximation for the single particle proton orbits in ^{206}Pb and subtracting the contribution of the proton $3s_{1/2}$ orbit, using the value of $r_{pfs} = 0.85$ fm. We add that the same value of α is obtained by assuming that the charge rms radius of the core 81 protons in ^{206}Pb is larger than that of ^{205}Tl by 0.005 fm, a value similar to the change in the charge rms radii for isotone in this region [80]. We note that $\Delta\rho_{Rp}(r)$ of Eq. (5.27) is normalized to 1. It is seen from Fig. 35b that $\Delta\rho_{Rp}(r)$ (dashed line) is above zero at the first node (at ~ 2.6 fm) and at the second node (r ~ 4.9 fm). We point out that the magnitude of the difference between $\Delta\rho_p(r)$ and $\Delta\rho_{Rp}(r)$ is similar to that of the experimental uncertainty.

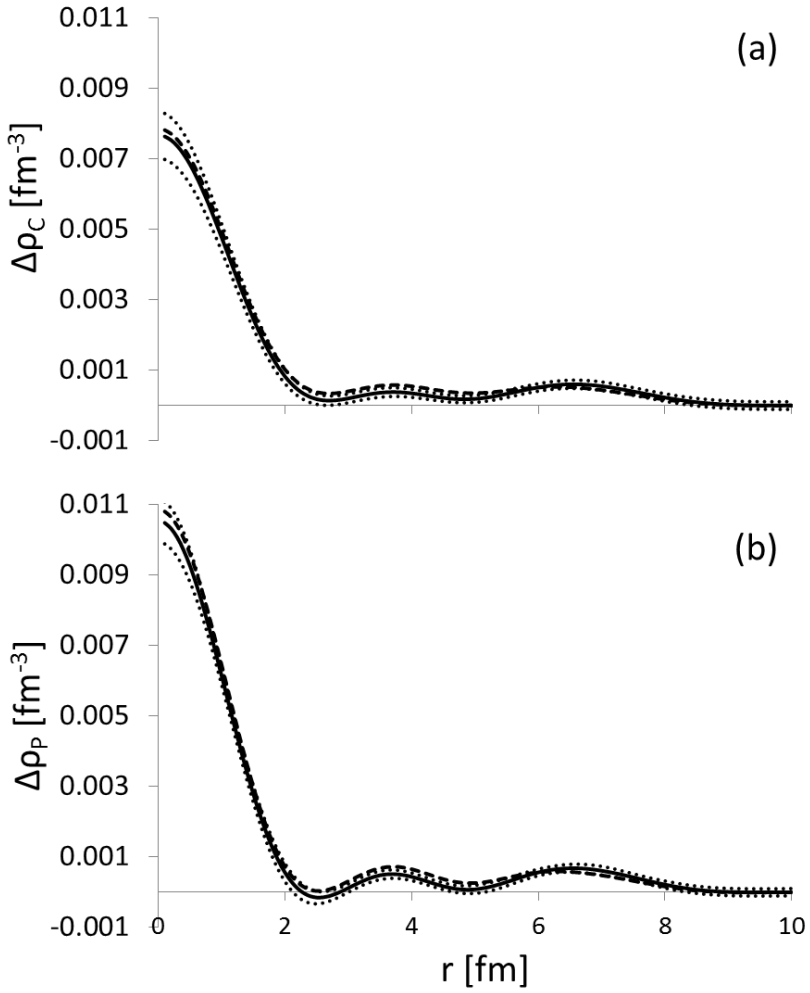

Fig.35 (a) The experimental difference, $\Delta\rho_c(r)$ between ^{206}Pb and ^{205}Tl charge distributions (solid line). The dashed line is for $\Delta\rho_{Rc}(r)$, the data after rearrangement correction. The dotted lines indicate the experimental uncertainty. (b) The experimental difference, $\Delta\rho_p(r)$ between ^{206}Pb and ^{205}Tl charge distributions (solid line). The dashed line is for $\Delta\rho_{Rp}(r)$, the data after rearrangement correction. The dotted lines indicate the experimental uncertainty.

Using the relation (5.8) we determined the corresponding square of the $3s_{1/2}$ convolved (charge) radial wave function $R_c^2(r) = 4\pi r^2 \Delta\rho_c(r)$ as obtained from Figure 35a and shown by the solid line in Figure 36a. Similarly, $R_{Rc}^2(r) = 4\pi r^2 \Delta\rho_{Rc}(r)$, the dashed line in Figure 36a is obtained from the dashes line in Figure 35a.The dotted lines

indicate the experimental uncertainty. In Figure 36b we present the square of the point particle radial wave function $R_p^2(r) = 4\pi r^2 \Delta\rho_p(r)$, (solid line) obtained from the solid line of Figure 35b. The dotted lines indicate the experimental uncertainty. Similarly, $R_{Rp}^2(r) = 4\pi r^2 \Delta\rho_{Rp}(r)$, the dashed line in Figure 36b is obtained from the dashed line in Figure 35b.

We have therefore used the experimental $R_p^2(r)$ of Figure 36b, shown by the solid line, to directly deduce the corresponding potentials by employing Eqs. (5.6), (5.7) and (5.9), obtaining the results shown in Figure 37a by the solid line. Similarly, in Fig. 37b we show the potential obtained from $R_{Rp}^2(r)$ of Figure 36b. The Coulomb potential of Eq. (5.14), with $R_c = 7.1$ fm, was adopted in the calculations. For the $3s_{1/2}$ orbit, there is no contribution from the centrifugal and spin-orbit potentials. We note that for a nonsingular potential *V*, $\frac{d^2R}{dr^2} = 0$ when $R(\vec{r}) = 0$. As seen from Figure 36b, this condition is not fulfilled at the nodes of the experimental $R_p^2(r)$. Moreover, in the vicinity of these nodes, the uncertainty in $\Delta\rho_p(r)$ is larger than its value. This leads to a very large uncertainty for *V* in the region of the nodes. We have thus constructed from the experimental data, radial wave functions having a proper behavior at the zeroes (around 2.6 fm and 4.9 fm), by fitting the experimental point radial wave function to the function $R_p = Asin(kr + \varphi)$ in the vicinity of the nodes. The corresponding (constant) potentials are shown by the dashed lines in Figure 37.

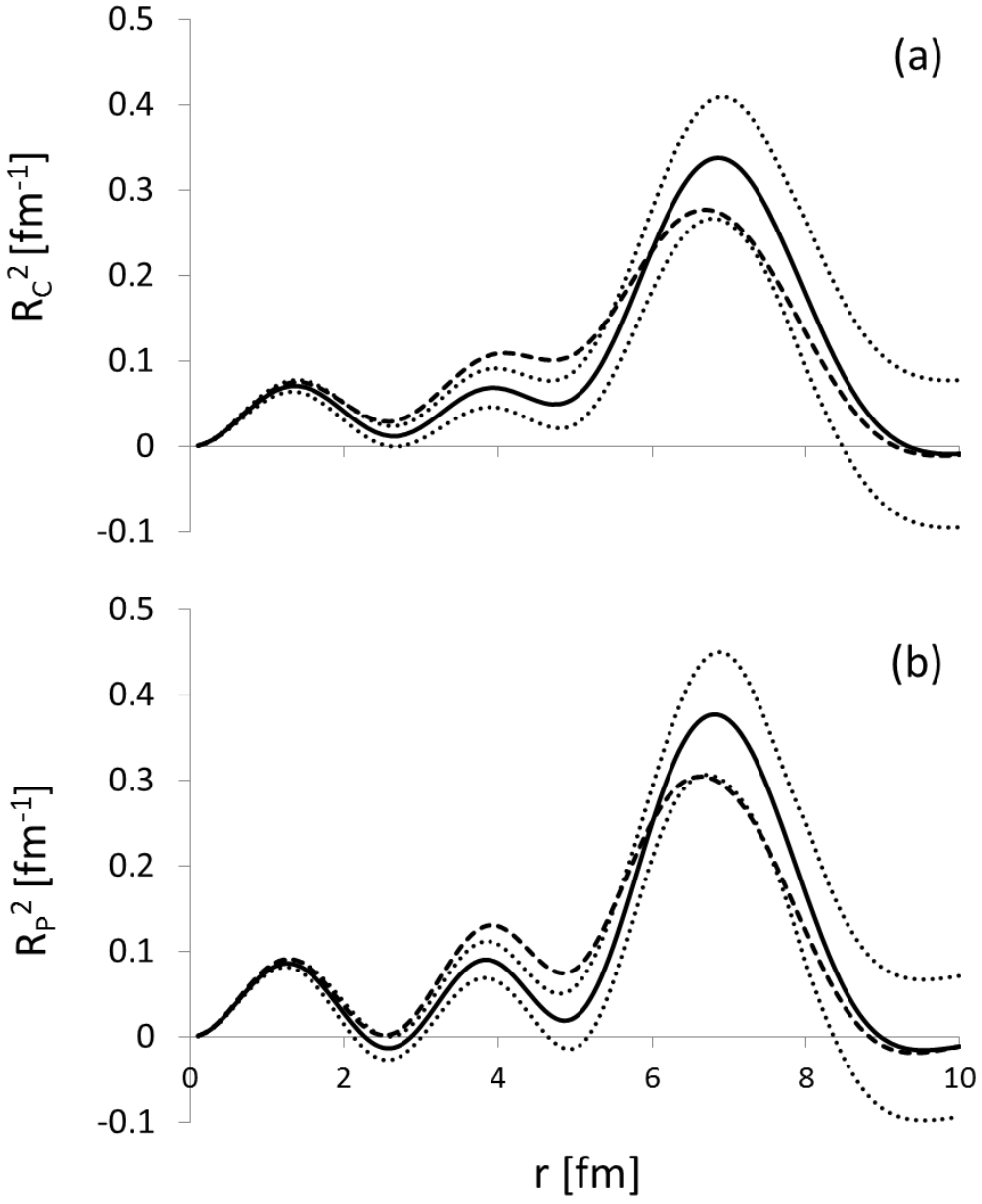

Fig.36 Similar to Figure 35. (a) $R_C^2(r) = 4\pi r^2 \Delta\rho_c(r)$. The dashed line is for $R_{Rc}^2(r)$ related to $\Delta\rho_{Rc}(r)$. (b) $R_P^2(r) = 4\pi r^2 \Delta\rho_p(r)$ where $\Delta\rho_p(r)$ is derived from the experimental $\Delta\rho_c(r)$. The dashed line is for $R_{Rp}^2(r)$ related to $\Delta\rho_{Rp}(r)$ similarly obtained from $\Delta\rho_{Rc}(r)$.

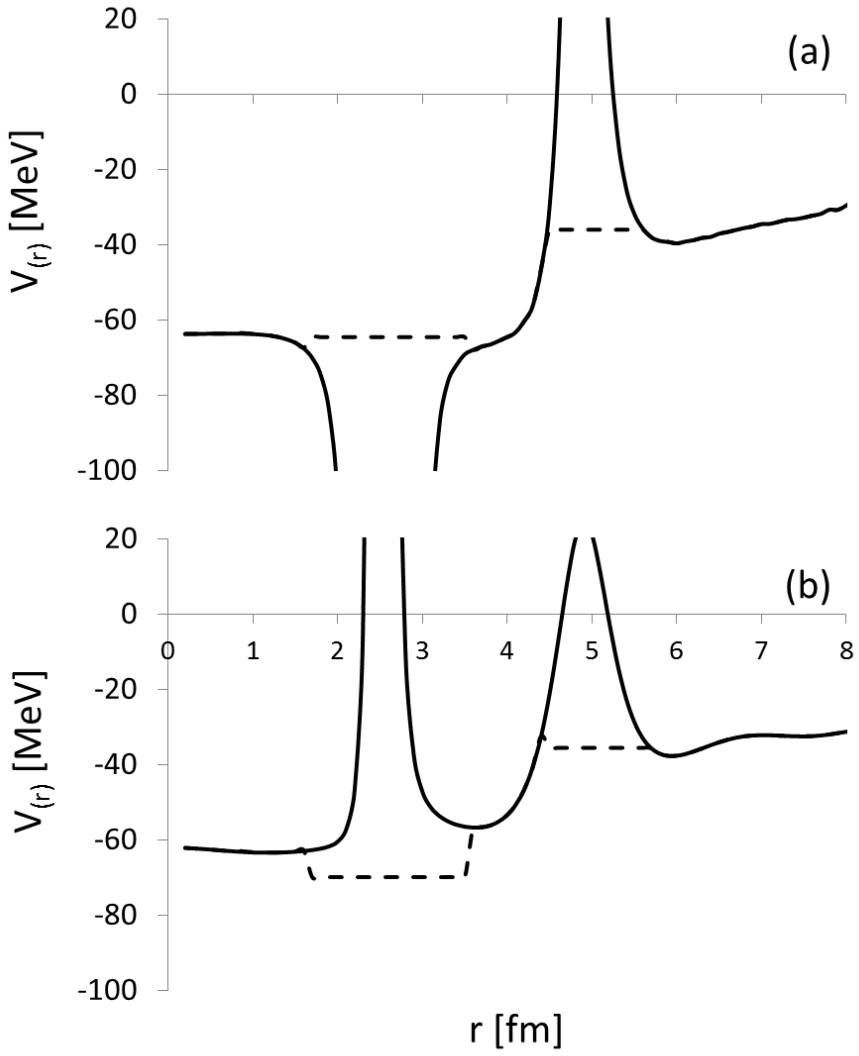

Fig.37 (a) The solid line is the potential derived from the $R_P^2\,(r) = 4\pi r^2 \Delta\rho_p(r)$ using Eqs. (5.7) and (5.9). The dashed line is the potential derived from an $R_p = Asin(kr + \varphi)$ fit near each of the minima of $R_P^2\,(r)$ since the potential blows up. (b) Similar to (a) except rearrangement correction has been taken into consideration.

In view of the resulting potentials shown in Figure 3, we have constructed from the experimental data a function $R_p^2(r)$ having a proper behavior at the zeroes (around 2.6 fm and 4.9 fm). This was done by fitting the experimental point radial wave function to a sum of two separate sine functions, $R_p = Asin(kr + \varphi)$, spliced together at $r \sim 5.3$

fm. This function is shown by the dashed line in in Figure 38a. Also shown in Figure 38a are the experimental data (solid line) and the uncertainty (dotted lines). We then determined the nuclear potential from the fitted $R_p^2(r)$ (dashed line of Figure 38a) by employing Eqs. (5.7) and (5.9). The results are shown by the dashed line of Figure 38b. Note the step function behavior of the resulting potential.

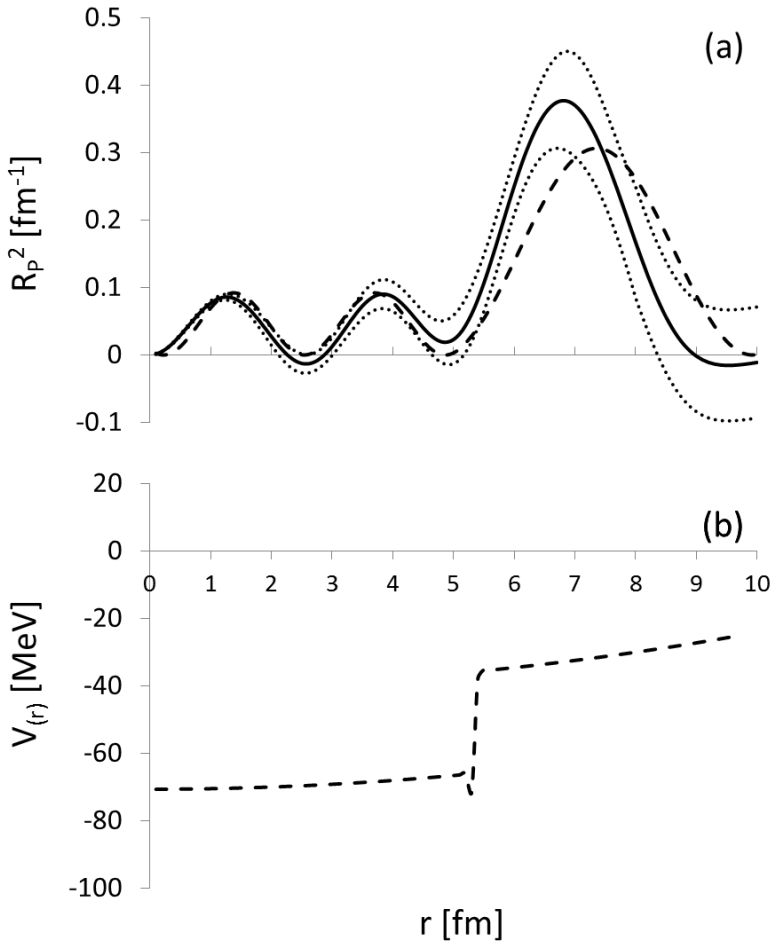

Fig.38 (a) The experimental difference, $R_P^2(r) = 4\pi r^2 \Delta\rho_p(r)$ between ^{206}Pb and ^{205}Tl charge distributions (solid line). The dashed line is for a $R_p = Asin(kr + \varphi)$ fit with two separate Sine functions spliced together at $r \sim 5.3$ fm. The dotted lines indicate the experimental uncertainty. (b) The dashed line is the potential derived from the spliced Sine functions using Eqs. (5.7) and (5.9).

We have therefore considered several nuclear central potentials with parameters obtained by fits of the calculated $R_p^2(r)$ to the corresponding experimental data, taking into account the Coulomb potential, Eq. (5.14). In Figure 39 we show the potential V_F(r), solid line, which is a smoothed potential of a jagged, multiply connected linear potential by taking the values of the jagged, linear potential at r = 3, 6 and 9 fm as free parameters, the value of r = 0 fm is constrained to reproduce the experimental value of 7.25 MeV for the separation energy of the proton $3s_{1/2}$ orbit and the value of the potential to be 0.0 MeV at r = 12 fm. The values of V_F(r) are determined by a polynomial fit to all the values of the jagged, linear potential and is smoothed near r = 0 and 12 fm so that the first derivative is zero. From a fit to the experimental data of $R_p^2(r)$, solid line in Figure 36b, we obtained that the values of V_F(r) at r = 0, 3, 6, 9 and 12 fm are -58.19, -81.35, -34.50, -23.54 and 0.0 MeV, respectively, with a corresponding χ^2 /N = 1.15. Similarly, the potential V_{RF}(r) (dashed line in Figure 39) is obtained by a fit to $R_{Rp}^2(r)$ (dashed line of Figure 36b) resulting in the values of -51.33, -88.29, -33.64, -23.96 and 0.0 MeV, for V_{RF}(r) at r = 0, 3, 6, 9 and 12 fm respectively, with a corresponding χ^2 /N = 1.81. The potential V_{WSF}(r), dashed double dotted line in Figure 39, is obtained by fitting WS potential, Eq. (5.13), obtaining the values of -167.95 MeV, -0.03 fm and 4.68 fm for V_0, R_1 and a_0, respectively, with the corresponding value of χ^2 /N = 3.28. For comparison, we also show by the dashed-dotted line the WS Potential V_{WS}(r) using the conventional values of -62.712 MeV, 7.087 fm and 0.65 fm for V_0, R_1 and a_0, respectively, with the corresponding value of χ^2 /N = 8.85.

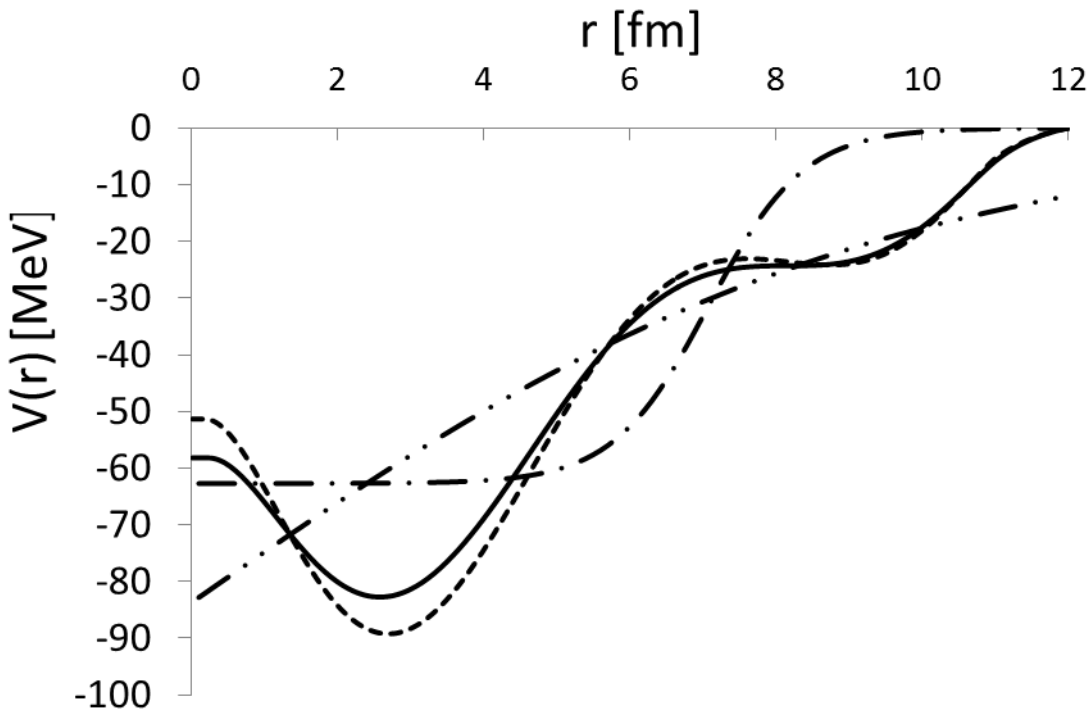

Fig.39 Potentials fitted to data in Fig.35b. The $V_F(r)$ potential (solid line), the $V_{RF}(r)$ version including rearrangement (dashed line) and the fitted $V_{FWS}(r)$ potential (double dotted-dashed line) are shown. Also shown is the conventional WS $V_{WS}(r)$ potential (dashed-dotted line).

In Figures 40a and 40b we compare the experimental results of the square of the convolved (charge) radial wave function $R_c^2(r)$ and the charge density $\Delta\rho_c(r)$ of the proton $3s_{1/2}$ orbit, respectively, with the corresponding results obtained from the potentials shown in Figure 39. The experimental data is given by the region defined by the dotted lines and the results obtained using, V_F(r), V_{WSF}(r) and V_{WS}(r) are shown by the solid, dashed-double dotted and dashed-dotted curves, respectively. Note that the results of the fitted potentials V_F(r) potential are in very good agreement with the experimental data. The results of the fitted potential V_{WSF}(r) are in reasonable agreement with data. It is important to point out that the amplitudes of the oscillations of $R_c^2(r)$ obtained from

the conventional WS potential V_{WS}(r) are much larger than those of the experimental data for r smaller than 5.0 fm and much smaller than the data for r larger than 5.0 fm. Also, as noted in Refs. [29,30], the calculated value of the charge density $\Delta\rho_c(r)$ at r = 0 fm obtained using the V_{WS}(r) potential is larger than the experimental value [29,30] by a factor of two.

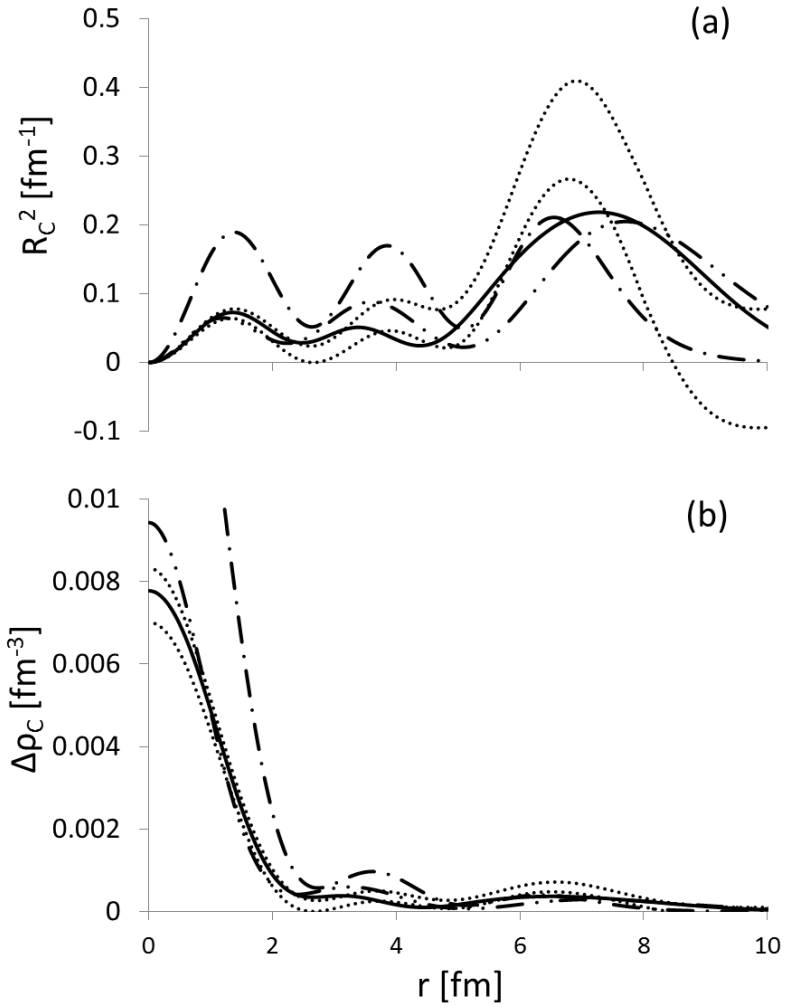

Fig.40 Experimental values of $R_c^2(r) = 4\pi r^2 \Delta\rho_c\,(r)$ (a) and $\Delta\rho_c\,(r)$ (b) plotted between dotted lines of error limits. They are compared to calculated charge distributions due to the $3s_{1/2}$ wave functions of the fitted $V_F(r)$ potential (solid lines), the fitted WS $V_{FWS}(r)$ potential (double dotted-dashed lines) and the conventional $V_{WS}(r)$ potential (dashed-dotted lines.

In Figure 41a, b and c we compare $R_c^2(r)$, the square of the radial functions, of the $1s_{1/2,}$ $2s_{1/2,}$ and $3s_{1/2}$ proton orbits, respectively, obtained from the fitted potential V_F(r) (solid lines) with those obtained from the conventional WS potential V_{WS}(r) (dashed-double dotted line). The separation energies of the $1s_{1/2,}$ $2s_{1/2,}$ and $3s_{1/2}$ proton orbits are -47.09, -22.64 and -7.24 MeV and -36.31, -24.46 and -8.00 MeV for the V_F(r) and V_{WS}(r) potentials, respectively. Note the relatively large separation energy of the $1s_{1/2}$ proton orbit obtained for the V_F(r), which is closer to the experimental data [81].

In Figure 42a, b and c, we show the corresponding charge density of the $1s_{1/2,}$ $2s_{1/2,}$ and $3s_{1/2}$ proton orbits for the V_F(r) (solid lines) and V_{WS}(r) (dashed-double dot lines) potentials, respectively. We point out that at r = 0 fm only the proton s orbits contribute to the charge density, $\rho_{ch}(r)$, in ^{206}Pb. The calculated value of $\rho_{ch}(0) = 0.060$ fm^{-3} for the fitted potential V_F(r) is significantly smaller than the value of $\rho_{ch}(0) = 0.073$ fm^{-3} for conventional WS V_{WS}(r), in good agreement with experimental value of $\rho_{ch}(0) = 0.063$ fm^{-3} [29,30].

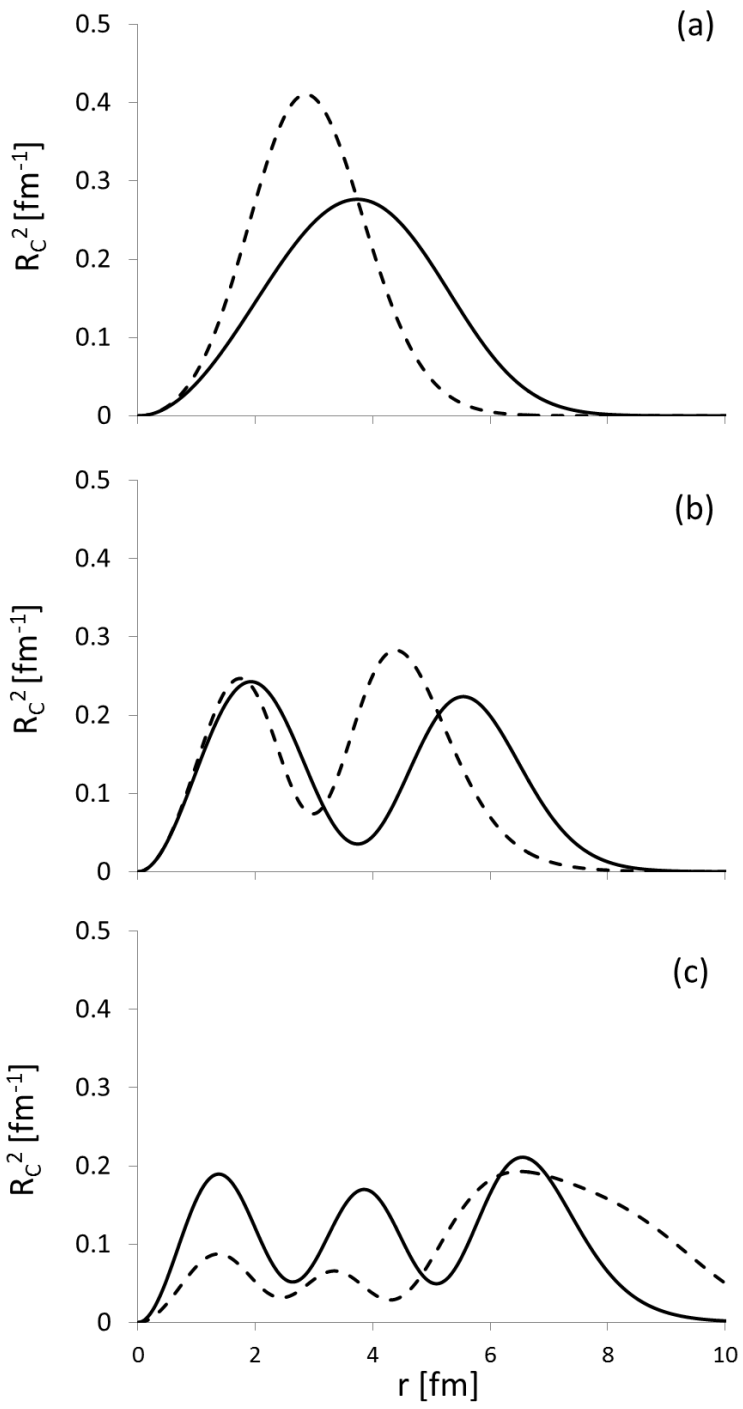

Fig.41 Calculated squared wave functions, $R_c^2(r) = 4\pi r^2 \Delta\rho_c\,(r)$, of a proton in the $1s_{1/2}$ (a), $2s_{1/2}$ (b) and $3s_{1/2}$ (c) orbits in the $V_F(r)$ potential (solid lines) and the conventional $V_{WS}(r)$ potential (dashed lines).

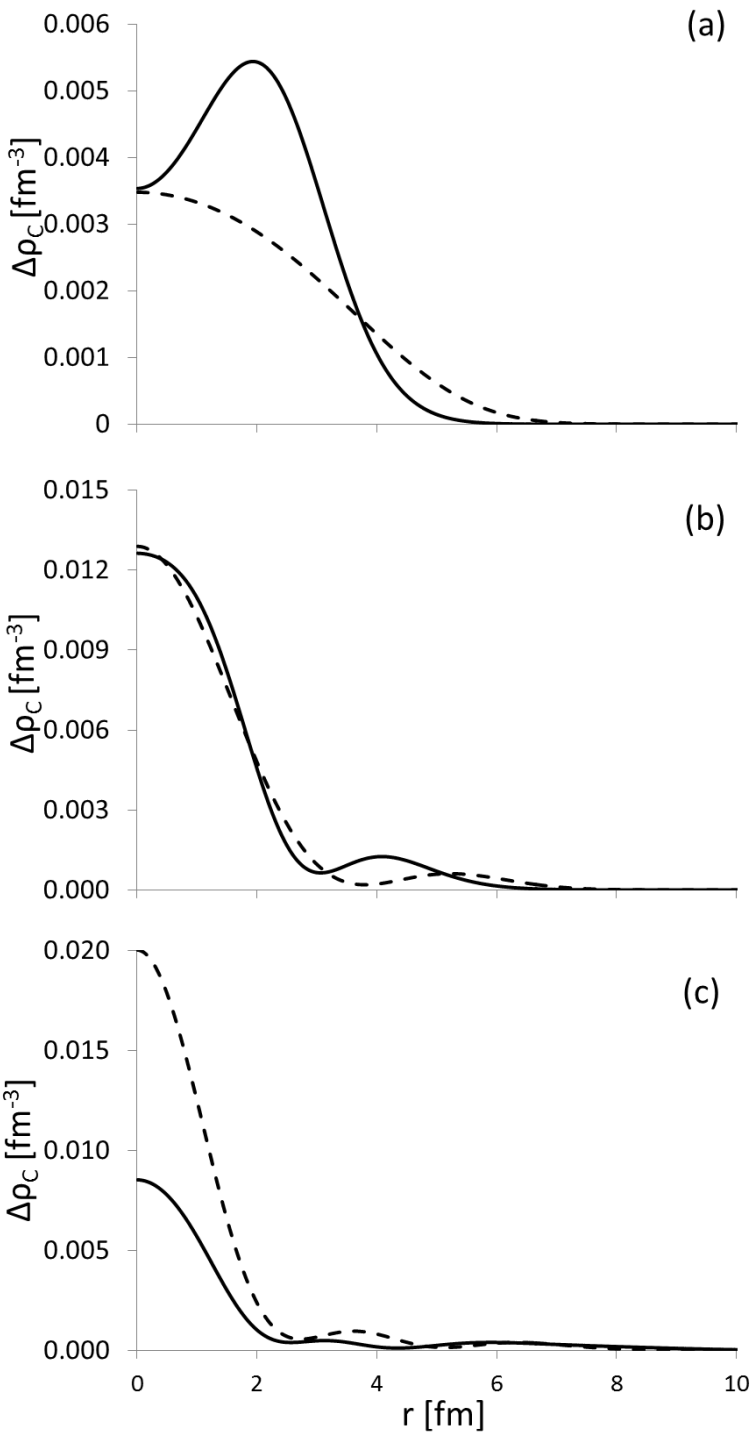

Fig.42 Calculated charge densities of a proton in the $1s_{1/2}$ (a), $2s_{1/2}$ (b) and $3s_{1/2}$ (c) orbits in the $V_F(r)$ potential (solid lines) and the conventional $V_{WS}(r)$ potential (dashed lines).

Conclusions

Starting from the single particle Schrödinger equation for the function $\Psi(\vec{r})$, with eigen-energy E, we have derived a novel method for determining the corresponding single particle potential *V* from $[\Psi(\vec{r})]^b$, where b is a real number, assuming that $[\Psi(\vec{r})]^b$, $\vec{\nabla}\Psi$ and $\Delta[\Psi(\vec{r})]^b$ are known for all positions $(\vec{r})$, see Eqs. (5.2) and (5.3). It is clear from the Schrödinger equation that for a nonsingular *V*, $\Delta\Psi(\vec{r}) = 0$ when $\Psi(\vec{r}) = 0$. This condition is extended to the requirements that $\vec{\nabla}\Psi = 0$ and $\Delta[\Psi(\vec{r})]^b = 0$, when $[\Psi(\vec{r})]^b = 0$. For b = 2, we have from Eqs. (5.2) and (5.3) that the potential $V(\vec{r})$ is given in term of the corresponding single particle matter density $\rho(\vec{r})$ (for real $\Psi(\vec{r})$) and its first and second derivatives.

We have presented results for the nuclear single particle potential *V* associated with the proton $3s_{1/2}$ orbit in ^{206}Pb deduced from the electron scattering [29,30] data for the charge density difference between the isotones ^{206}Pb – ^{205}Tl, obtained by employing our new method for the special case of spherical symmetry, Eqs. (5.7) and (5.10). The results for the proton $3s_{1/2}$ orbit in ^{206}Pb, shown in figure 37a, exhibit large uncertainty for *V* around the zero values of the $3s_{1/2}$ proton density $\Delta\rho_p(r)$, where the experimental uncertainty in $\Delta\rho_p(r)$ is lager than its value. It is difficult to see whether the conditions that the first derivative of $\Delta\rho_p(r)$ and the corresponding expression in the square brackets in right hand side of Eq. (5.10) vanish when $\Delta\rho_p(r) = 0$, which are necessary for determining a nonsingular *V*, are satisfied by the experimental data for $\Delta\rho_p(r)$.

We have also carried out a least-square fit of the calculated density $\Delta\rho_p(r)$ of the $3s_{1/2}$ point proton density to the corresponding experimental data, using the three parameter WS potential and a potential defined by its values at r = 0, 3, 6, 9, and 12 fm and compared with the results obtained from the conventional WS potential. We note that the fitted potentials exhibit large diffuseness (Figure 39). As seen from Figure 40, we obtained good agreements with the experimental data for the fitted potentials, whereas the results obtained from the conventional WS potential are in disagreement with data. Clearly more accurate experimental data for $\Delta\rho_p(r)$ with uncertainty smaller by a factor of two or more may help in answering the question how well can the data be reproduced be a calculated $3s_{1/2}$ single particle wave function and determining the form of *V*.

CHAPTER VI

SUMMARY[*]

We have presented results of our fully self-consistent HF-RPA calculations for the centroid energies of isoscalar and isovector giant resonances of multipolarities $L = 0 - 3$ in ^{40}Ca, ^{48}Ca, and ^{208}Pb using 18 and 34, respectively, commonly employed Skyrme type interactions of Table 1, and compared with available experimental data. The goal of using the Skyrme potential is to find an effective potential which best describes the ground state properties of nuclei and their excited states such as giant resonances for light to heavy nuclei and then to proceed to glean information about the parameters of the equation of state of asymmetric nuclear matter. We have investigated and discussed the sensitivity of the E_{CEN} of the giant resonances to various properties of NM. We have also investigated the relationship between the electric polarizability and the neutron skin in ^{208}Pb where we found there is not a strong enough correlation to narrow down the neutron skin.

The Skyrme forces we used were unable to reproduce ^{48}Ca – ^{40}Ca centroid energy differences of the ISGMR. For ^{40}Ca, ^{48}Ca, and ^{208}Pb the ISGDR was consistently higher than the experimental data except for the SkP interaction. We have demonstrated the very strong correlation of E_{CEN} of the ISGQR and the ISGOR for ^{40}Ca, ^{48}Ca, and ^{208}Pb with m*/m. However, ^{40}Ca and ^{48}Ca prefer m*/m = 0.65 – 0.80 while ^{208}Pb prefers

[*] Part of this chapter is reprinted with permission from "Giant Resonances in ^{40}Ca and ^{48}Ca" by M. R. Anders *et. al.*, 2013. *Physical Review C*, **87**, 024303, Copyright [2013] by American Physical Society.

m*/m = 0.9 – 1.0. The effective mass in nuclear matter is better determined by ^{208}Pb rather than ^{40}Ca or ^{48}Ca due its larger nucleon number which better approximates infinite nuclear matter, meaning m*/m = 0.9 – 1.0 is the more certain estimate for the effective mass. Caution must be used when seeing correlations among the centroid energies of the GRs and the NM properties since the NM properties also can have strong correlations among themselves as in the case of m*/m and K_{NM}. We have also reconfirmed the very strong correlation between the ISGMR centroid energy in ^{40}Ca, ^{48}Ca, and ^{208}Pb and K_{NM}. However, we have demonstrated that there are no strong correlations between the IVGDR centroid energy and the parameters of the symmetry energy, J, L, and K_{sym}. This again demonstrates the need to use a wide variety of interactions and not to vary the parameters of one interaction to investigate possible correlations. This part of the study has been carried out to find better constraints on the parameters of nuclear matter such that a new search for a better Skyrme force can take place.

We also succeeded in extracting some limited information about the mean field from the $3s_{1/2}$ state in ^{206}Pb and ^{205}Tl even though the data was challenging around the nodes. Starting from the single particle Schrödinger equation for the function $(\vec{r})$, with eigen-energy E, we have derived a novel method for determining the corresponding single particle potential *V* from the corresponding single particle matter density $\rho(\vec{r})$ (for real $\Psi(\vec{r})$) and its first and second derivatives.

We have presented results for the nuclear single particle potential *V* associated with the proton $3s_{1/2}$ orbit in ^{206}Pb deduced from the charge density difference between the isotones ^{206}Pb – ^{205}Tl, obtained by employing our new method for the special case of

spherical symmetry. The results for the proton $3s_{1/2}$ orbit in ^{206}Pb exhibit large uncertainty for the mean-field potential around the zeroes of the $3s_{1/2}$ proton density, where the experimental uncertainty is larger than its value. Tighter error bars around the zeroes of the proton density would therefore be of great help in the pursuit of the mean-field potential.

REFERENCES

[1] A. Bohr and B. M. Mottelson, *Nuclear Structure II, (Benjamin, New York, 1975).*

[2] P. Ring and P. Schuck, *The nuclear many-body problem*, (Springer, New York -Heidelberg-Berlin, 1980).

[3] S. Shlomo, V. M. Kolomietz, and G. Colo, Eur. Phys. J. **A30**, 23 (2006) and references therein.

[4] N. K. Glendening, Phys. Rev. C **37**, 2733 (1988).

[5] J. M. Lattimer and M. Prakash, Phys. Rep. **442**, 109 (2007).

[6] W. D. Myers and W. J. Swiatecki, Phys. Rev. C **57**, 3020 (1998).

[7] L. Satpathy, V. S. U. Maheshwari and R. C. Nayak, Phys. Rep. **319**, 85 (1999).

[8] J.P. Blaizot, Phys. Rep. **64**, 171 (1980).

[9] H. Krivine, J. Treiner and O. Bohigas, Nucl. Phys. **A336**, 155 (1984).

[10] E. Lipparini and S. Stringari, Phys. Rep. **175**, 103 (1989).

[11] J. Treiner, H. Krivine, and O. Bohigas, Nucl. Phys. **A371**, 253 (1981).

[12] D. H. Youngblood, P. Bogucki, J. D. Bronson, U. Garg, Y.-W. Lui, and C. M. Rozsa, Phys. Rev. C **23**, 1997 (1981).

[13] B. K. Jennings and A. D. Jackson, Phys. Rep. **66**, 141 (1980).

[14] S. Shlomo and D.H. Youngblood, Phys. Rev. C **47**, 529 (1993), and references therein.

[15] J. M. Pearson, N. Chamel and S. Goriely, Phys. Rev. C **82**, 037301 (2010).

[16] T.H.R. Skyrme, Phil. Mag. **1**, 1043 (1956).

[17] T.H.R. Skyrme, Nucl. Phys. **9**, 615 (1959).

[18] D. Vautherin and D. M. Brink, Phys. Rev. C **5**, 626 (1972).

[19] Y.-W. Lui, D.H. Youngblood, S. Shlomo, X. Chen, Y. Tokimoto, Krishichayan, M. Anders, and J. Button, Phys. Rev. C. **83**, 044327 (2011).

[20] D.H. Youngblood, Y.-W. Lui, H.L. Clark, Y. Tokimoto, and B. John, Phys. Rev. C **68**, 057303 (2003).

[21] D.H. Youngblood, Y.-W. Lui, and H.L. Clark, Phys. Rev. C **63**, 067301 (2001).

[22] D.H. Youngblood, Y.-W. Lui, and H.L. Clark, Phys. Rev. C **55**, 2811 (1997).

[23] Nguyen Van Giai and H. Sagawa, Phys. Lett. **106B**, 379 (1981).

[24] B.K. Argawal, S. Shlomo, and V. Kim Au, Phys. Rev. C **72**, 014310 (2005).

[25] J. Bartel, P. Quentin, M. Brack, C. Guet, and H.B. Hakansson, Nucl. Phys. **A382**, 79 (1986).

[26] B.K. Argawal, S. Shlomo, and V. Kim Au, Phys. Rev. C **68**, 031304 (2003).

[27] A. de Shalit and I. Talmi, *Nuclear Shell Model*, Academic Press, New York, N.Y., 1963.

[28] B. K. Agrawal, S. Shlomo and V. Kim Au, Phys. Rev. C **72**, 014310-1-13 (2005).

[29] J. M. Cavedon, *et al*, Phys. Rev. Lett. **49**, 978 (1982).

[30] B. Frois, et al, Nucl. Phys. **A396**, 409c (1983).

[31] V. R. Pandharipande, I. Sick and P. K. A. deWitt Huberts, Rev. Mod. Phys. **69**, 961 (1997)

[32] S. Shlomo, in *The Universe Evolution: Astrophysical and Nuclear Aspects,"* Eds., L. Blokhintsev and I. Strakovsky, Nova Science Publishers, 2013.

[33] S. Shlomo and G. Bertsch, Nucl. Phys. **A243**, 507 (1975).

[34] P. -G. Reinhardt, Ann. Phys. (Leipzig) **1**, 632 (1992).

[35] T. Nakatsukasa, T. Inakura and K. Yabana, Phys. Rev. C **76**, 024318 (2007).

[36] E. Chabanat, P. Bonche, P. Haensel, J. Meyer and R. Schaeffer, Nucl. Phys. **A627**, 710 (1997).

[37] W. Kohn, Rev. Mod. Phys. **71**, 1253 (1999).

[38] S. Shlomo, Rep. Prog. Phys. **41**, 957 (1978).

[39] M. Bender, P. H. Heenen, and P.-G. Reinhard, Rev. Mod. Phys. **75**, 121 (2003).

[40] M. Dutra, O. Lourenco, J. S. Sa Martins, A.Delfino, J. R. Stone and P. D. Stevenson, ArXiv:1202.3902v1, Phys. Rev. C.**85**, 035201 (2012).

[41] P. -G. Reinhard, and H. Flocard, Nucl. Phys. **A587**, 467 (1995).

[42] P. Klupfel, P. -G. Reinhard, T. J. Burvenich and J. A. Maruhn, Phys. Rev. C **79,** 034310 (2009).

[43] N. Lyutorovich, V. I. Tselyaev, J. Speth, S. Krewalsd, F. Grummer and P.-G. Reinhard, Phys. Rev. Lett. **109**, 092502 (2012).

[44] L. Bennour, P.-H. Heenen, P. Bonche, J. Dobaczewski and H. Flocard, Phys. Rev. C **40**, 2834 (1989).

[45] J. Dobaczewski, H. Flocard, and J. Treiner. Nucl. Phys. **A422**, 103-139 (1984).

[46] P.-G Reinhard, D. J. Dean, W. Nazarewicz, J. Dobaczewski, J. A. Maruhn, and M. R. Strayer, Phys. Rev. C **60**, 014316 (1999).

[47] L. G. Cao, U. Lombardo, C. W. Shen, and Nguyen Van Giai, Phys. Rev. C **73**, 014313 (2006).

[48] Lie-Wen Chen, Che Ming Ko, Bao-An Li, and Jun Xu, Phys. Rev. C **82**, 024321 (2010).

[49] A. W. Steiner, M. Prakash, J. M. Lattimer, and P. J. Ellis, Phys. Reports **411**, 325 (2005).

[50] P. A. M. Guichon, H. H. Matevosyan, N Sandulescu, and A. W. Thomas, Nucl. Phys. **A772**, 1-19 (2006).

[51] F. Tondeur, M. Brack, M. Farine, and J. M. Pearson, Nucl. Phys. **A420**, 297-319 (1984).

[52] B. Alex Brown, G. Shen, G. C. Hillhouse, J. Meng, and A. Trzcińska, Phys. Rev. C **76**, 034305 (2007).

[53] J. Friedrich and P.-G. Reinhard, Phys. Rev. C **33**, Number 1, 335-351 (1986).

[54] S. Shlomo and W. G. Love, Physica Scripta **26**, 280 (1982).

[55] Tapas Sil, S. Shlomo, B.K. Agrawal, and P.-G. Reinhard, Phys. Rev. C **73**, 034316 (2006).

[56] V. O. Nesterenko1, J. Kvasil2, and P.-G. Reinhard, Phys. Rev. C **66**, 044307 (2002).

[57] C. Colo, L. Cao, N. V. Giai, and L. Capelli, Comp. Phys. Comm. **184**, 142-161 (2013).

[58] S. Shlomo and A. I. Sanzhur, Phys. Rev. C **65**, 044310 (2003).

[59] B. K. Agrawal, S. Shlomo and A. I. Sanzhur, Phys. Rev. C **67**, 034314 (2003).

[60] M. R. Anders, *et al*., Phys. Rev. C **87**, 024303 (2013).

[61] E. Erell, J. Alster, J. Lichtenstadt, M. A. Moinester, J. D. Bowman, M. D. Cooper, F. Irom, H. S. Matis, E. Piasetzky, and U. Sennhauser, Phys. Rev. C **34**, 1822 (1986).

[62] P. Gleissl, M. Brack, J. Meyer, and P. Quentin, Ann. of Phys. **197,** 205 (1990).

[63] A. Veyssière, H. Beil, R. Bergère, P. Carlos, A. Leprêtre, and A. De Miniac, Nucl. Phys. **A277**, 513 (1974).

[64] G. J. O'keefe, M. N. Thompson, Y. I. Assafiri, R. E. Pywell and K. Shoda, Nucl. Phys. **A469**, 239 (1987).

[65] D. A. Sims *et al*., Phys. Rev. C **55**, 1288 (1997).

[66] A. Kolomiets, O. Pochivalov and S. Shlomo, Phys. Rev. C **61**, 034312-1-8 (2000).

[67] S. Kamerdzhiev, J. Speth, and G. Tertchny, Eur. Phys. J. A **7**, 483 (2000); S. Kamerdzhiev, J. Speth, and G. Tertchny, Phys. Reports **393**, 1 (2004).

[68] M. R. Anders, *et al*., submitted to Phys. Rev. C (2015).

[69] D. H. Youngblood, Y.-W. Lui, H. L. Clark, B. John, Y. Tokimoto, and X. Chen, Phys. Rev. C **69**, 034315 (2004).

[70] A. Tamii *et al*., Phys. Rev. Lett. **107**, 062502 (2011).

[71] S. S. Henshaw, M. W. Ahmed, G. Feldman, A. M. Nathan, and H. R. Weller, Phys. Rev. Lett. **107**, 222501 (2011).

[72] D. S. Dale, R. M. Laszewski, and R. Alarcon, Phys. Rev. Lett. **68**, 3507 (1992).

[73] R. Leicht, M. Hammen, K.P. Schelhaas, and B. Ziegler, Nucl. Phys. **A362**, 111 (1981).

[74] K.P. Schelhaas *et al*., Nucl. Phys. **A489**, 189 (1988).

[75] D. M. Drake, *et al*., Phys. Rev. Lett. **47**, 1581 (1981).

[76] P.-G. Reinhard and W. Nazarewicz, Phys. Rev. C **81**, 051303(R) (2010).

[77] Wojciech Satuła, Ramon A. Wyss, and Michał Rafalski, Phys. Rev. C **74**, 011301(R) (2006).

[78] M. R. Anders, S. Shlomo and I. Talmi, ArXiv: 1504.05507v1, submitted to Phys. Rev. C (2015).

[79] L. R. B. Elton, *Nuclear Sizes*, Oxford University Press, London, 1961.

[80] H. Euteneuer, J. Friedrich and N. Voegler, Nucl. Phys. **A298**, 452 (1978).

[81] A. A. Vorobev, Y. V. Dotsenko, A. A. Lobodenko, O. V. Miklukho, I. I. Tkach, A. Y. Tsaregorodtsev, and Y. A. Shcheglov, Phys. At. Nucl. **58**, 1817 (1995).